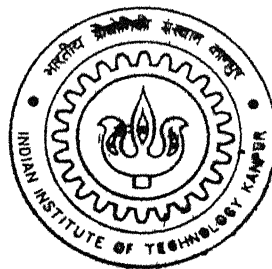# Study of Fracture and Cavitation Behavior of Superplastic Materials: Cu-Zn-Al and Al-Mg Alloys

By

Subhasish Bandyopadhyay

DEPARTMENT OF MATERIALS AND METALLURGICAL ENGINEERING
Indian Institute of Technology Kanpur
June, 2002

Study of Fracture and Cavitation Behavior of Superplastic Materials: Cu-Zn-Al and Al-Mg Alloys

A Thesis Submitted
In Partial Fulfillment of the Requirements
For the Degree of

MASTER OF TECHNOLOGY

By

Subhasish Bandyopadhyay

TO THE

**DEPARTMENT OF MATERIALS AND METALLURGICAL ENGINEERING.
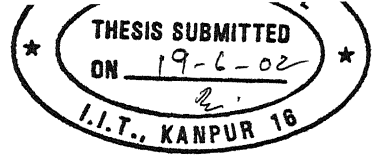INDIAN INSTITUTE OF TECHNOLOGY, KANPUR
JUNE 2002**

Dedicated to

My Parents

Certificate

This is to certify that the present work, entitled "**STUDY OF FRACTURE AND CAVITATION BEHAVIOR OF SUPERPLASTIC MATERIALS: Cu-Zn-Al AND Al-Mg ALLOYS**" BY Mr. Subhasish Bandyopadhyay has been carried out under my supervision and to the best of my knowledge it has not been submitted elsewhere for a degree.

Dr. Sandeep Sangal
Professor
Dept of Materials and Metallurgical Engg.
Indian Institute Of Technology
Kanpur
Date: 19/6/02

ACKNOWLEDGEMENT

Subhasish Bandyopadhyay

ABSTRACT

Cavitation is frequently observed in superplastic deformation. In this present investigation cavitation and fracture behavior in superplastic deformation of two alloys, Cu-Zn-Al and Al-Mg were studied. The different sections of the tensile gauge length have been qualitatively and quantitatively analyzed. The fracture surfaces were also analyzed to make a correlation between different parameters like strain rate and rolling direction. Two strain rates, $2x10^{-2}s^{-1}$ and $2x10^{-4}s^{-1}$, had been used. There were three orientation of tensile gauge length with the rolling axis: parallel, normal and 45 degree angle. Strain rate has a significant effect on the morphology of cavitation and fracture behavior. The degree of cavitation increases with decreasing distance from the fracture tip along the gauge length. It is also observed that orientation differences between tensile axis and rolling direction play an important role in cavitation behavior as well as fracture behavior.

Contents

List of Figures

Figure

1. Introduction and Objectives

Superplastic materials are polycrystalline solids which have the ability to undergo large uniform strains prior to failure. For deformation in uniaxial tension, elongations to failure in excess of 200% are indicative of superplasticity, although several materials can attain extension greater than 1000%.

When a superplastic material fails during tensile deformation it is either the result of unstable plastic flow or a consequence of the growth and interlinkage of internally nucleated voids. In the former processes, inhomogeneities in the cross-sectional area of a test lead to localized increase in the strain rate and the difference in the cross-sectional area increases. The rate at which the discontinuity in the cross-sectional area increases depends on both the strain hardening and the strain rate sensitivity. In superplastic materials, where true strain hardening is minimal, any neck which is present will grow, although the rate of growth decreases with increasing m. unstable plastic flow normally results in the material pulling out to a fine point prior to failure. In superplastic deformation failure occurs as the result of the nucleation, growth and interlinkage of internal voids, the fracture surface is more abrupt. In this investigation, fracture and cavitation behavior were studied in Cu-Al-Zn and Al-Mg alloys. These alloys exhibit superplasticity at temperature above $0.4T_M$, where T_M is the melting temperature of the alloy.

The following aspects of superplastic deformation were studied.

1. To study the effect of strain rate on fracture and cavitation behavior.
2. To investigate the effect of rolling direction on cavitation behavior.
3. To correlate the degree of cavitation with strain.
4. To characterize fracture surface and microstructure.

2. Literature Survey

2.1 Introduction

There is enough appeal to Superplasticity that the word is likely to endure even though there is nothing especially superior about the plasticity of a metal in that state. Many ordinary ductile metals will neck down with as much 100% reduction in area before parting in tension. What is unusual about a superplastic metal is its necking resistance and the more nearly uniform distribution of plasticity, or ductility, that follows.

Superplasticity can be induced both in materials possessing a stable, ultra-fine grain size at the temperature of deformation.($> 0.4T_M$, where T_M is the absolute melting point) and in those subjected to special environmental condition , e.g. thermal cycling through a phase change. These two categories are best described a "structural" and "environmental" superplasticity, respectively [1]

Prior to 1945 the deformation behavior of the class of alloys that possessed "viscous properties between glass and pitch" [2] was known under different names. The term superplasticity became common after 1945 when the Russian word SVERKHPLASTICHNOST, introduced by Bochvar and Sviderskaya (3), got so translated.

2.2 Historical Contribution.

Observations of what appeared to be superplastic behavior were made in late 1920s by Hargreaves [4,5] and Jenkins [6]. However, the most spectacular of the earlier observation was that by Pearson [7]. While working on eutectics, he reported a tensile elongation of 1950% without failure for Bi-Sn alloy. Pearson also examined the bulging characteristics of his materials using internal pressurized tubular specimens. In 1945 Bochvar and Sviderskaya coined the term superplasticity.

Although papers on superplasticity occasionally appeared after 1945, the major increase in interest came in 1962 with a article review of Underwood on work in USSR [8] .His work illustrated the ductility of Zn-Al alloy, which gave 650 % elongation at 250 °C. This result attracted the attention of Backofen at the MIT. His research group studied details of the Zn-Al monotectic alloy and Pb-Sn eutectic composition materials. Of great significance is that Backofen and his colleagues showed that the superplastic Zn-Al alloy could be formed into a practical shape by a simple air pressure operation [9]. The paper of Backofen dealt with the phenomenological basis for superplastic flow in terms of the now well-known relationship.

$$\sigma = \kappa \varepsilon^m$$

where σ is the applied stress, ε is the strain rate and k and m are constant dependent on test parameter like temperature and grain size.

In the field of ceramics extensive efforts are made in the West during the 1950s to hot fabricate ceramics using conventional metallurgical processes such as extrusion, rolling, and forging. In 1986, a major breakthrough occurred: a 3-mol %yttria stabilized tetragonal zirconia (YTZP) and its composite were shown to be superplastic in tension tests [10].

Superplasticity studies intermetallics began in 1987. Materials such as nickel aluminides, nickel silicides, and titanium aluminides have been shown to be superplastic [11]. In the area of composites, superplasticity of a fine-grained, aluminum composite reinforced with silicon carbide whiskers was discovered in 1984 [12]. Interestingly, it was observed at a very high strain rate (about $10^{-1}s^{-1}$).

2.3. Mechanical Aspects

2.3.1 Characteristics of Deformation.

The most important mechanical characteristics of a superplastic material is its high strain rate sensitivity of flow stress, referred to as 'm' and defined by

$$\sigma = k\varepsilon \qquad \dots\dots\dots\dots\dots\dots\dots\dots\dots\dots \quad 1.1$$

where σ is the flow stress, ε is the strain rate and k is the material constant.
Restating the relationship

$$\sigma = k\varepsilon^m = P/A \qquad \dots\dots\dots\dots\dots\dots\dots\dots\dots\dots \quad 1.2$$

where P is the force being transmitted through a cross section of area A. At any point along a rod in tension

$$\varepsilon = (1/l)(dl/dt) = -1/A(dA/dt) \qquad \dots\dots\dots\dots\dots\dots \quad 1.3$$

Combining Eq.1.2 and Eq. 1.3

$$-dA/dt = (P/K)^{1/m} [1/A^{(1-m)/m}] \qquad \dots\dots\dots\dots\dots\dots \quad 1.4$$

$$\frac{dA}{dt} \propto \frac{1}{A^{\frac{1-m}{m}}}$$
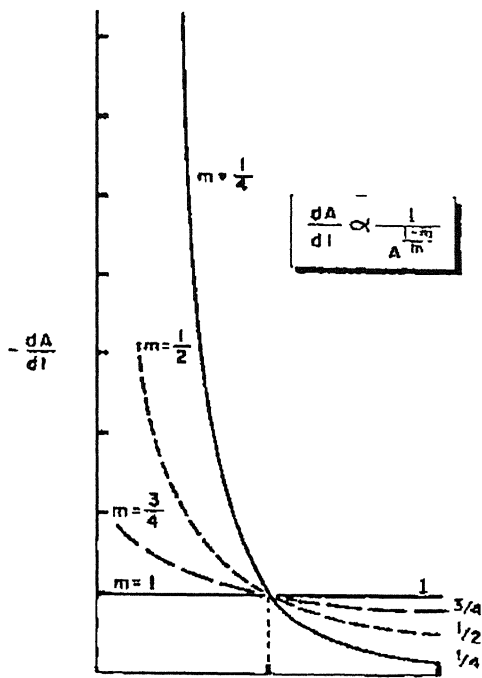
A

Fig 1 Dependence of the cross-sectional shrinkage rate on cross-section size for different amounts of strain rate sensitivity.

Therefore as long as m is < 1, the smaller the cross section the more rapidly it is reduced .As m approaches 1, the reduction rate at all cross section approaches a common level, as indicated schematically in fig. 1. When m=1, the flow is Newtonian viscous and dA/dt is independent of A, so that any cross-sectional irregularities are simply preserved during pulling.

It can be seen from eq. 1.1 that if the relationship between σ and ε is measured and then plotted logarithmically the slope of the plot is equal to the strain rate sensitivity of the flow stress , m. In practice most superplastic materials show a sigmoidal variation of the flow stress with strain rate. In Fig 2 it is evident that the strain rate sensitivity passes through maximum .A value of m >0.3 delineates the superplasticity regime (region 2). Both the high and low strain rate ranges exhibit values of m in the range 0.1 to 0.3. the

region at high strain rates (region 3) is recovery controlled dislocation creep (power law creep). Deformation within this region leads to the observation of slip lines and to the development of high dislocation densities within the grains. A crystallographic texture within the material is increased and significant grain elongation occurs during deformation.

In the superplastic regime, Region 2, where high uniform strains are observed, experimental studies have so far failed to identity a unique rate controlling mechanism of deformation. It is clear, however, that that grain boundary sliding and grain boundary rotation make a substantial contribution to the total strain. In contrast to region 3 the grains remain equiaxed throughout the deformation and materials which initially show microstructural banding develop a more uniform equiaxed microstructure. Crystallographic texture may be reduced during deformation in this region. TEM studies have shown only limited evidence for dislocation activity within the grains of superplastically deformed materials. The flow stress σ, decreases and the strain rate sensitivity, m, increases with increasing temperature, T, and the decreasing grain size, d, (Fig. 2). The elongation to failure to failure in this region tends to increase with increasing m.

It has been suggested that the decrease in the strain rate sensitivity with decreasing strain rate is only apparent and results from a threshold stress for deformation, or from the effects of microstructural instability (grain growth hardening). Alternatively, the similarity in stress exponent (n = 1/m) between region 1 and region 3 has been used to imply that region 1 also recovery controlled dislocation creep.
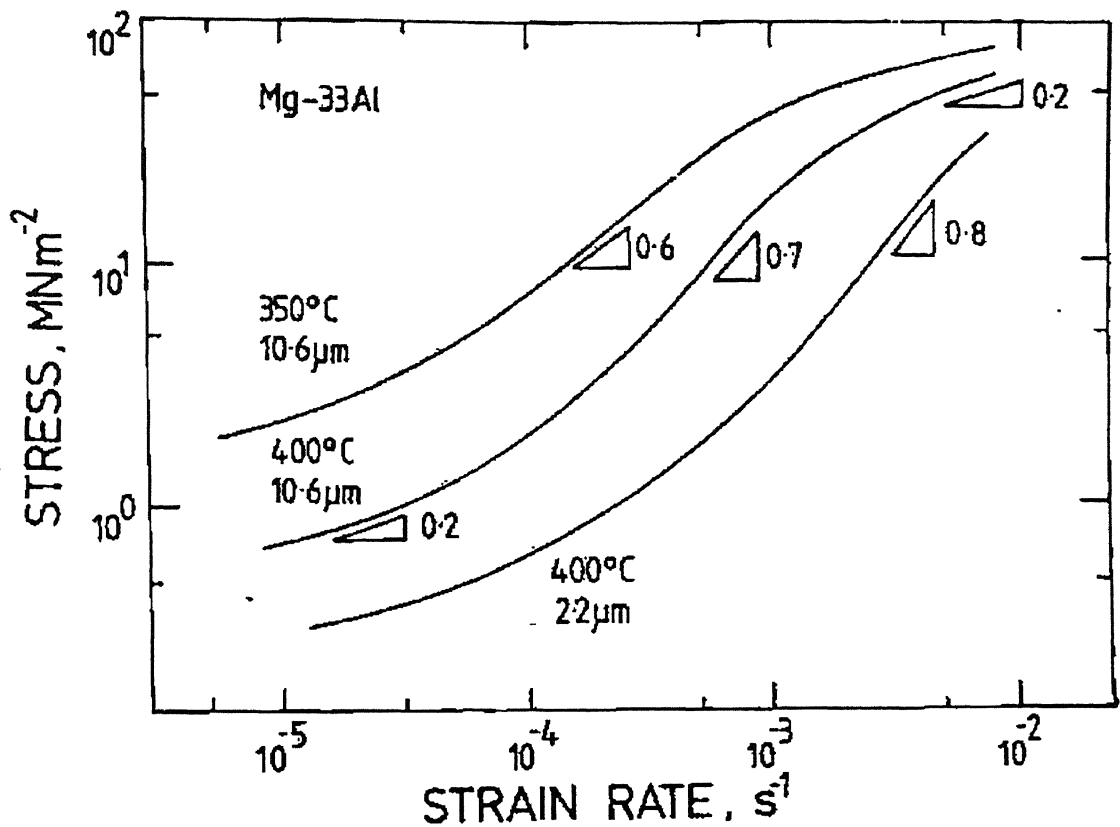
Fig 2. Measured variation of the flow stress with strain rate for a superplastic Al-Mg eutectic at different temperature and grain sizes.

2.3.1.1 Superplastic Flow – Region 2

At intermediate strain rates (Region 2) the flow process is less understood, although there is agreement on the microstructural features associated with it. Strain is accumulated by the motion of individual grains or cluster of grains relative to each other by sliding and rolling. Grains are observed to change their neighbors and to emerge at the free surface from the interior. During deformation the grains remain equiaxed, or, if they were not equiaxed prior to deformation, become so during superplastic flow. Textures become less intense as a result of deformation in Region 2, while the converse is normally observed in Region 3. the motion of individual grains is dependent on both the normal and shear stresses acting on their grains boundaries and is therefore dependent on the shape and orientation of the grains. Translation and rotation are thus stochastic in nature, occurring different directions, to different extents, at different location.

Many attempts have been made to develop theories capable of predicting both the mechanical topological features of superplastic deformation. However, none have yet been completely successful. Unlike recovery controlled dislocation creep, where dislocation climb is accepted as the rate controlling process, several rate limiting mechanism have been proposed for superplastic deformation [15].

2.3.1.2 Dislocation Models

When grain boundaries slide, stress concentrations develop wherever that sliding is obstructed. Relaxation of the stress concentration by the emission of dislocation from one grain boundary and their absorption by another can be limited by the rate at which the dislocation are emitted, the rate at which they can cross the grains (glide or lattice climb control) or the rate at which they are absorbed into the boundaries (grain boundary climb control). The glide process has been assumed to occur relatively rapidly in superplasticity since there is a lack of either strong obstacles or significant solute drag effects within the grains at the deformation temperature [16]. Pile-ups of dislocations adjacent to the grain boundaries are thought to develop and provide a back stress against which the sliding grain(s)would have to work to emit further dislocations along a particular slip plane. Climb of the leading dislocation from the pile up into the boundary would allow another dislocation to be emitted and enable a small increment of grain boundary sliding to be accumulated (Fig 3). If only one source per grain were activated then flow would be boundary controlled. By allowing grain boundary ledges to act as dislocation sources, the absolute magnitude of the predicted strain rate can vary by upwards of two orders of magnitude and is therefore source dependent. The deformation rate is given by

$$\varepsilon_{xx} = A_{xx} \, D_{gb} \delta Gb/kT \, [(b/d)^2 \, (\sigma/G)^2] \qquad \ldots\ldots\ldots\ldots\ldots\ldots 1.5$$
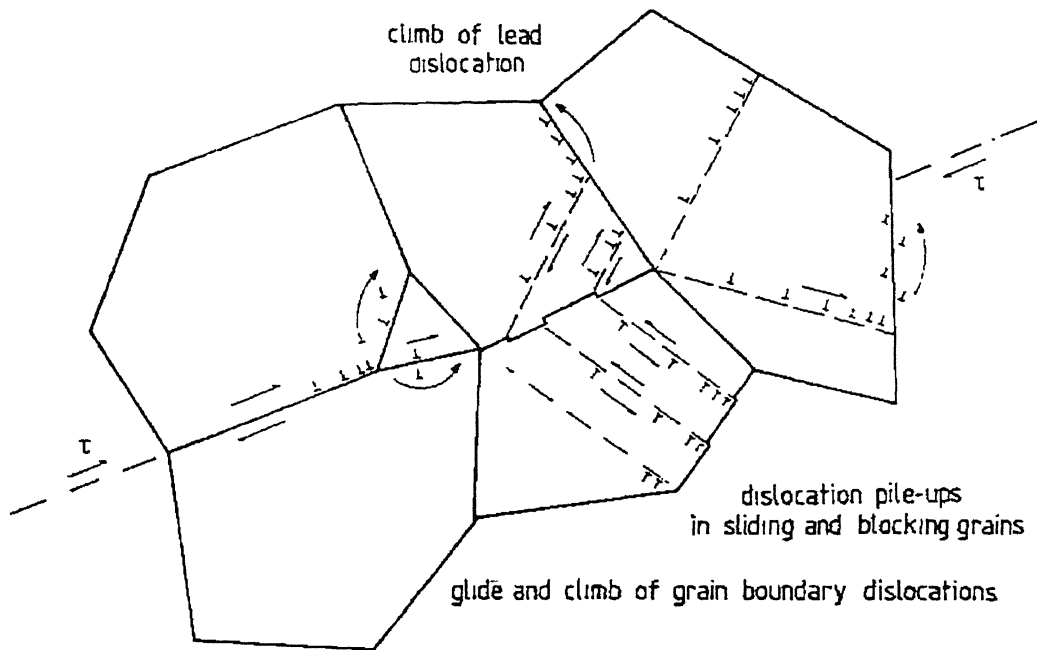
Fig 3 Dislocation pile-up models of superplastic flow [16].

2.3.1.3 Diffusion Model

It has also been envisaged that mass could be redistributed by diffusional flow. Driven by differences in the stress dependent chemical potential on adjacent grain boundaries, mass transport from regions of compression to tension would occur. Sliding is accommodated by a gradual change in grain shape as matter is moved by diffusion [17,18]. Grain boundary migration restores the orientation (Fig.3.). the retention of an equiaxed grain shape is therefore achieved in the model of Ashby and Verral. Furthermore, because a transient but finite increase in grain boundary area results from the shape change, the model predicts a threshold stress for superplastic flow. The strain rate in the superplastic region is that due to diffusion but operating under an apparent stress,σ^*. This stress is equal to the applied stress less the stress necessary to create that additional grain boundary energy.

$$\varepsilon_{x-xx} = A_o \, D_{diff} Gb/kT \, [b/d]^2 \, [\sigma^*/G] \dots\dots\dots\dots\dots 1.6$$

If the sliding results in grain switching then no matter how small the individual three-dimensional shape change steps are, a finite increase in the grain boundary area would still be required. The work done in creating the new grain boundary surface would be some fraction oh the instantaneous grain boundary area and would have to be supplied by the external stress. The increased grain boundary energy is used to drive the subsequent grain boundary migration but the energy is lost in the form of heat. The work done per grain would vary as d^2 and thus the threshold stress, which is the work done per unit volume, will vary as $1/d$. The threshold stress for superplastic flow predicted by the diffusion accommodation model varies as the inverse of the grain size.
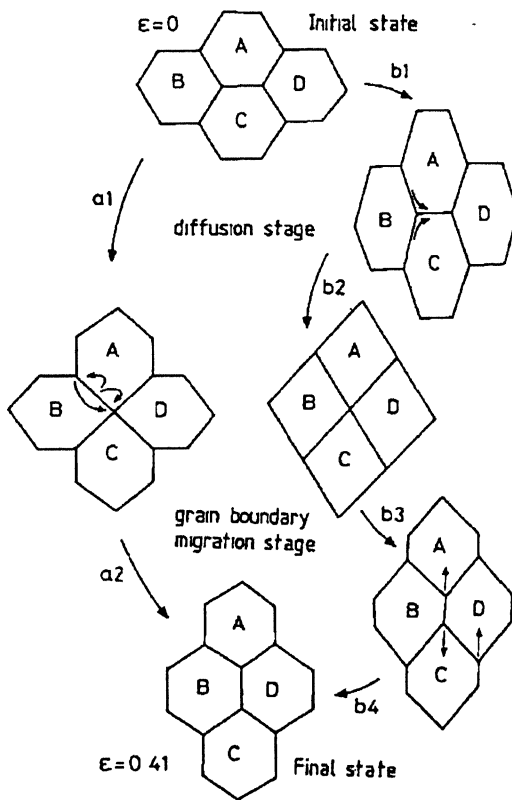
Fig 4 Grain switching through diffusional mass transport [18]

2.3.1.3 Grain Boundary Sliding

To examine the process of grain boundary sliding consider a two dimensional array of of regular hexagons orientated at random with respect to a remotely applied stress field (Fig. 5). The normal and shear stresses acting on each grain boundary can be balanced by

stresses acting throughout the continuum body. If it is assumed that the grain boundary shear stresses are fully relaxed then the grain boundary sliding rate will be controlled by the rate at which the normal stresses on the grain boundaries are relaxed. For the case of uniaxial tension, the average stress, σ_{avg}, on a given grain boundary is

$$\sigma_{avg} = \sigma\infty \left(3/2 - \sin\theta \right) \quad\text{.....................................} \quad 1.7$$
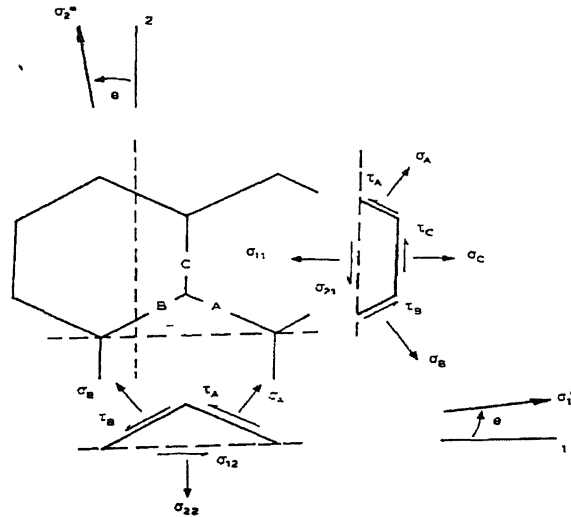
Fig 5 An idealized array of hexagonal grains subjected to a uniaxial stress [18].

where $\sigma\infty$ is the applied stress, and θ is the angle between the applied stress and the normal to the grain boundary. Ih, for example , diffusion relaxes the normal stresses then the strain rate is simply that due to diffusion creep, i.e.

$$\varepsilon_{xx} = 15 \, D_{diff} \, Gb/kt \, [b/d]^2 \, [\sigma/G] \quad\text{.............................} \quad 1.8$$

This may be compared with Eq. 1.6 except that there is no threshold stress. During diffusional stress relaxation, the local value of the normal stress can vary from 0 at the triple points to anywhere between +2.16 and –0.72 times the applied stress at the center of the grain boundaries. For uniaxial compression, diffusional mass transport would be predicted to occur from the center of grain boundaries oriented approximately perpendicular to the applied stress, via the triple point, to the center of boundaries oriented mainly parallel to the applied stress. If the applied stress was tensile then diffusional flow would occur in the opposite direction. The predicted diffusion paths are in excellent agreement with the modified paths for diffusion accommodated superplastic flow (Fig 4) [18].

If on the other hand the normal tractions on the grain boundaries are relaxed by rapid diffusional flows ($\sigma_a = \sigma_b = \sigma_c = \sigma/2$) then the average shear stress, τ_{avg}, acting parallel to the boundary would be given by

$$\tau_{avg} = -\sigma\infty (2 \sin\theta.\cos\theta) \quad \dots\dots\dots\dots\dots\dots\dots\dots \quad 1.9$$

and the corresponding strain rate by

$$\varepsilon_{xx} = A[\sqrt{3}/2]^{n-1} [\sigma/G]^n \quad \dots\dots\dots\dots\dots\dots \dots\dots \quad 1.10$$

where A is a rate constant, and n the stress exponent characterizing the stress relaxation process. If all the boundaries are equally resistant to sliding then the strain rate is independent of the orientation of the grains. If the boundary viscosity varies with, for example, misorientation or precipitate density, then

$$\varepsilon_{xx} = 1/\sqrt{3}d \ [(S_a - S_b) (2\cos^2\theta -1) +(S_a + S_b -2S_c) (2\sin\theta . \cos\theta)] \ \dots\dots\dots 1.11$$

where the grain center shear rate, S_1, is related to the grain boundary shear rate, X_1, and the shear stress acting on that boundary, τ_1, through the relationships

$$S_1 = X_1 \text{ and } X_1 \propto \tau_1^n \quad \dots\dots\dots\dots\dots\dots\dots\dots\dots\dots\dots \quad 1.12$$

The grain boundary is only equal to the grain size center shear rate when the grains do not rotate. Grain boundary sliding can, therefore, be accommodated by relaxing the shear stresses in and adjacent to the grain boundaries, and the process can be equated with the 'core and mantle' model of superplastic deformation [19].

equal grain centre offset

sliding only $(\chi = \chi_B)$
no rotation $(\omega = 0)$

no sliding $(\chi = 0)$
rotation only $(\omega = \omega_9)$

sliding $(\chi < \chi_9)$·
rotation $(\omega < \omega_S)$

a   b   c
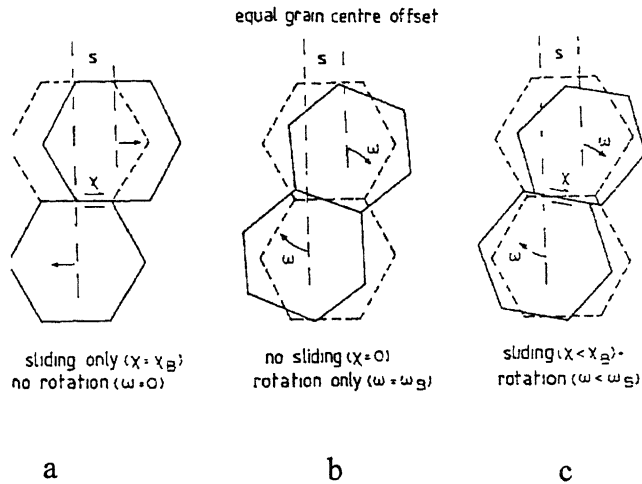
Fig 6, Sliding and rotational displacements required to generate a given grain center offset between two adjacent hexagonal grains. (a) sliding only, (b) rotation only and (c) a mixture of sliding and rotation [19].

In Fig.6, it can be seen that a given grain center shear displacement, s, and hence a macroscopic strain, ε, can be achieved not only by sliding a distance X_B along the boundary, but also by rotation of the boundary through an angle W_B. if both processes are allowed to operate simultaneously then a given grain center shear displacement can be achieved by lesser rotation and sliding , i.e.

$$S = X + w\,d \quad \ldots\ldots\ldots\ldots\ldots\ldots\ldots\ldots\ldots\ldots 1.13$$

Where w is the average rotational velocity of the grains on either side of the grain boundary. If no holes appear in the structure then the average strain rate is twice that when rotation is not allowed. A given strain rate can therefore be maintained for smaller grain boundary sliding rates and hence at a lower stress. Moreover, for a given grain boundary sliding rate the strain rate would increase as the grain size was reduced. Thus grain boundary sliding and superplastic deformation would be expected to become increasingly apparent in progressively finer materials.

2.3.2 The Strain-rate Sensitivity Index, m

From Eq. 1.1 we can derive

$$m = d (\ln \sigma)/d (\ln \varepsilon) \qquad \dots\dots\dots\dots\dots\dots \ \dots\dots\ 1.14$$

This is the slope in the σ - $\ln \varepsilon$ curve (Fig. 2). There are various methods of measuring m but broadly all lead to variation of m with ε of the form shown in Fig 7. m also varies with temperature and structure (grain size).
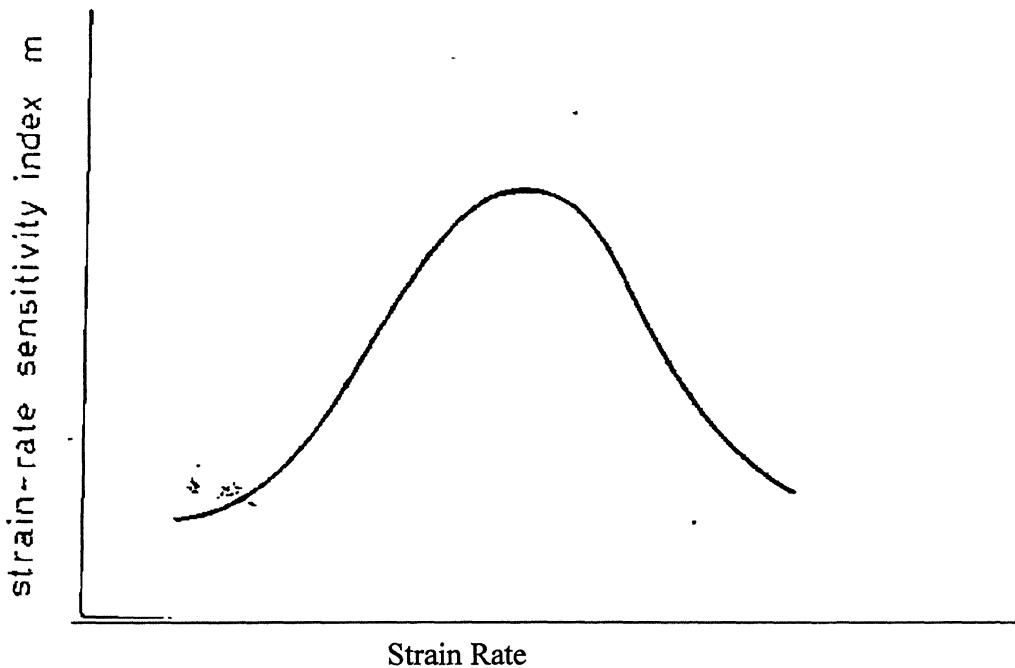
Strain Rate

Fig 7 The Variation of the strain-rate sensitivity index with strain rate [3]

2.3.2.1 Determination of m from the σ - ε curve.

In this method m is determined as the slope of the experimental $\ln \sigma$ -$\ln \varepsilon$ plots. The latter are obtained using instantaneous values measured in the steady state region. The rate at which data are controlled can be increased if incremental increases in the in the strain rate are carried out in a single test. The slop of the curve is measured either by graphically or by better using by a curve fitting procedure and carrying out differentiation.

2.3.2.2 Determination of m using change in strain-rate method

This is the most widely used procedure and is normally based on the description of Backofen *et al.* (13). As shown in Fig. 8 if the crosshead velocity is suddenly increased from V_1 to V_2 there is a corresponding increase in inn load. If straining is continued for a few percent to eliminate transient effects a load comparison can be made. The lower velocity curve is extrapolated to established a common strain for measurement (point A and point B in Fig 8 are of equal strains) if m is assumed to be nearly independent of strain rate in the range covered by the velocity increases then

$$m = \ln (P_A/P_B)/\ln (V_2/V_1 \quad \dots\dots\dots\dots\dots\dots\dots\dots\dots\dots \quad 1.15$$
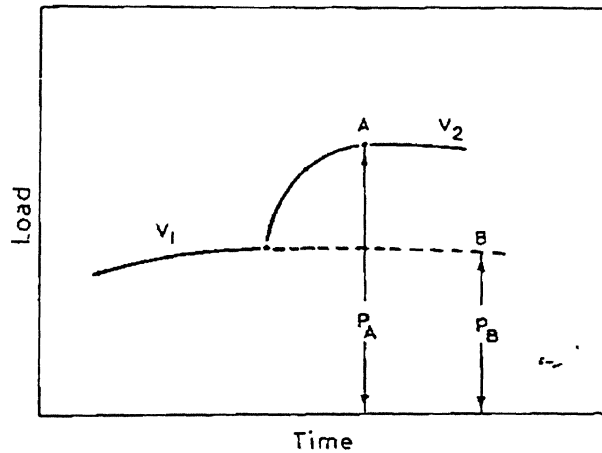
Fig 8 A schematic load time diagram representing a velocity change from V_1 to V_2. times A and B represent the same strain at the different pulling speeds [3]

Variations to this method can be introduced by identifying the critical points on the load time curve slightly differently. Considering Fig.9, a more detailed version of Fig. 8, the alternatives can be examined. Another approach is to calculate the true stresses and the true strain rate at the points of maximum load (A and C in Fig.9). Then

$$m = \ln (\sigma^A/\sigma^C)/\ln (\varepsilon^A/\varepsilon^C) \quad \dots\dots\dots\dots\dots\dots\dots\dots \quad 1.16$$

A velocity-change test can also involve a velocity decrease 14) for which equivalent form of equations 1.15 and 16 can be defined. With references to Fig. 9. these are,

$$m = \ln (P_C{'}/P_B{'})/\ln (V_1/V_2) \quad \text{.........................} \quad 1.17$$

and

$$m = \ln (\sigma^{C'}/\sigma^A)/\ln (\varepsilon^{C'}/\varepsilon^A) \quad \text{.........................} \quad 1.18$$

2.3.3 Necessary Conditions For Deformation

The existences of fine-grained equiaxed polyphase structures, with the phase displaying similar ductility at the temperature of deformation, is conductive to superplasticity. The rates of deformation should be such as to given give m values of 0.3 or more.

Single-phase materials e.g. cold rolled nickel can be rendered superplastic by rapid testing. Duplex and multiphase structures have stable grain sizes which are resistant to grain growth and these alloys are significantly more superplastic. The type of phase or phases, their distribution, the grain boundary condition temperature, strain rate and grain size all influences the degree of superplasticity observed. The purity of the base metals from which alloys are prepared does not appear to affect the superplasticity tendency provided the grain size is the same. Heat treatment does not change the functional dependence of variables. There is also an empirical rule that for a given base metal the lower the eutectic temperature of the alloy better the superplastic properties.

Although under favorable conditions even non-random initial structures give rise to superplastic effects, depending upon the extent of directionality present in the microstructure elongation in the range of 70 to 300 percent was necessary before isotropic superplasticity deformation could be induced. For a given strain, however, the tendency towards ideal behavior increased with decreasing with strain rate and / or increasing volume fraction of the second phase in the alloy.

On the other hand, superplasticity has not been observed in many alloys with continuous solubility. When the grain size is coarse, as in the β-Pu prepared from γ-Pu, or the grain boundaries were not flat and the structure was not equiaxed and uniformly fine grained no superplastic effects could be observed. Annealing the material to coarsen the structure and/or to dissolve the second phase also eliminated rate sensitivity and high elongation. Non-deformable second phase particle, as found in dispersion hardening alloys, eliminated effect of fine grain size and led to cavitation. In iron carbon alloys undissolved carbides, residual massive martensite, and non-equilibrium structures have been shown to prevent superplasticity. In alloys system e.g. the Zn-Al eutectoid, where quenching confers ultra-fine grain size, quenching from below the invariant temperature and homogenization destroyed superplastic tendency. Moreover, when the condition $0.4T_M < T < T_M$, where T is the absolute temperature of superplastic deformation and T_M is the appropriate transformation temperature which defines the upper limit of the two phase field for the alloy, was not satisfied or when the grain growth at the deformation temperature is very rapid, significant superplasticity was absent. Finally, when one of the phases is high melting and/or the proportion of the second phase is very small as in the Al-Fe, Al-Si, and Al-Ni system, optimal superplasticity is not observed.

Cast or cast homogenized alloys of eutectic, eutectoid or polyphase composition were also not although in the wrought condition they exhibited significant superplasticity. This difference has been attributed variously to the lamellar, dendritic or interlocking nature of grain boundaries in the cast alloys.

2.3.3.1 Grain refinement by mechanical working.

1.3.3.1.1 Duplex alloys

Grain refinement in equilibrium duplex alloys is accomplished by hot working the material close to the temperature range where superplastic deformation is to be carried

out. In most cases the temperature is as high as possible concomitant with a microstructure consisting of approximately equal volume fraction of the two phases. If phases have different deformation characteristics, such as one being harder and one more brittle than the other, then working would fragment the harder phase. The softer phase would then be forced to infiltrate and separate the harder phase. The phases can recrystallise and spherodise during hot working process. Alternatively, if the two phases have very similar mechanical responses, working first elongates the grain structure and then fragments it by the development of intense shear bands. Again the original structure can be reformed, but on a much finer scale by recrystallization. In some cases, the fine equiaxed structure is developed from a cold rolled material by recrystallization during heating immediately prior to superplastic deformation.

Grain growth during heat treatment superplastic flow is restricted as the individual phases have different chemical composition. In order that grain growth can occur solutes must diffuses from the smaller grains of each phase through or around the other phase to the to the larger grains. As alloy addition partition to the phase in which they are most soluble, the rate of mass transfer of the alloy element through the other phase is restricted by its limited solubility. The grain size is then said to be 'segregation stabilized '. A duplex superplastic material of very high structural stability would be one in which the component metals showed little or no solid solubility.

2.3.3.1.2 Pseudo single phase alloys.

Grain refinement as a result of warm working and recrystallization treatments has been used extensively in the development of superplastic aluminum based alloy. The alloys are termed pseudo single phase since they consist almost entirely of a solid solution strengthened matrix with <10% by a volume of a precipitate phase which is present to stabilize the microstructure against grain growth. The alloys are constituted such that two types of particles are present during worm working but that usually only one, the finer of the two, remains at the superplastic forming temperature.

The high density of dislocation which forms during worm working would normally tend to rearrange themselves by climb to form dislocation walls and possibly subgrain boundaries. In the absence of any fine particles the dislocation array would migrate by climb allowing the microstructure to undergo continuous recovery and ultimately recrystallization. However, the presence of fine particles, which are usually less than 0.2 μm in diameter, prevents recovery by exerting a drag on the migrating dislocation, dislocation walls, and subgrain boundaries. Mechanical working in the presence of the fine particles therefore generates and maintains a large amount of stored energy and introduces into the microstructure a large number of potential nucleation sites for subsequent recrystallization

Alloys which contain predominantly fine particles develop a fine grain equiaxed microstructure during the initial stages of superplastic deformation by in situ recrystallization.

Alloys which contain predominantly fine particles develop a fine grain equiaxed microstructure during the initial stages of superplastic deformation by in situ recrystallization. The particles and solutes which prevent recrystallization during warm working àt lower temperature cease to be effective in restraining dislocation migration at the higher deformation temperatures. The majority of the grains which form on heating to the superplastic deformation temperature have very similar crystallographic orientation because of the texture introduced into the material during worm working. As high temperature deformation and hence grain boundary sliding proceeds, the misorientation between the grains increase and leads to the formation of high angle grain boundaries and a true superplastic microstructure which can undergo grain boundary sliding (Fig. 10)
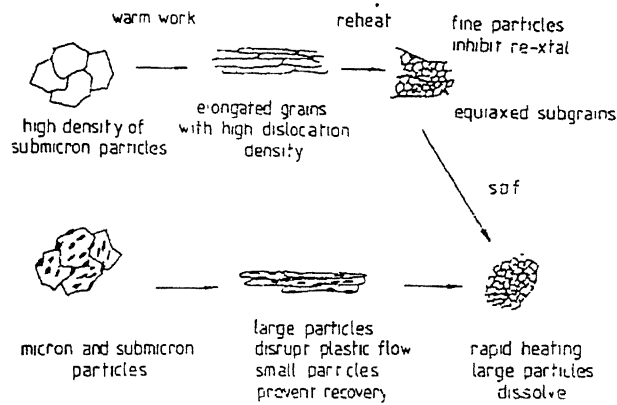
Fig 10 Schematic illustration of the microstructural changes that occur during grain refinement by mechanical working of pseudo single phase alloys.

A second group of pseudo single phase alloys contains both fine and coarse particles during processing. The presence of larger particles, which are usually greater than 1μm in diameter, provide nucleation sites for recrystallization and cause localized distortion in the orientation of plastic flow during warm working. The resulting differences in crystallographic orientation of the material, on a very fine scale, lead to the nucleation of recrystallized grains with widely varying boundaries as the embryonic grains impinge. Materials which contain predominantly the larger particles are statically recrystallized to produce the fine equiaxed microstructure by annealing prior to superplastic deformation.

2.3.3.2 Grain refinement by phase transformation

Several studies have shown that repeated thermal cycling of a material through a phase transformation could result in a very fine grain size. The mechanism of grain refinement is the nucleation of the reaction product at several sites on the grain boundaries of the parent phase. The product phase then grows as the transformation proceeds, replacing the single parent grains by a multitude or smaller grains. Repeated cycling through the phase transformation further refines the structure until a saturation grain size is reached (Fig. 11). A similar effect can be achieved by controlled rolling above the transformation temperature such that a heavily deformed but unrecrystallized parent phase is produced.

The high dislocation density within the parent phase results in a large number of nucleation sites for the product phase. The parent phase transform directly to a fine grain product on cooling. Ideally superplastic deformation would take place in the temperature range where the two phases are present in order that the grain size is stabilized. However, if superplastic deformation is to be carried out at a temperature where the material is single phase then additional steps need to be taken to prevent grain growth – e.g. the introduction of fine dispersoids to pin the grain boundaries.
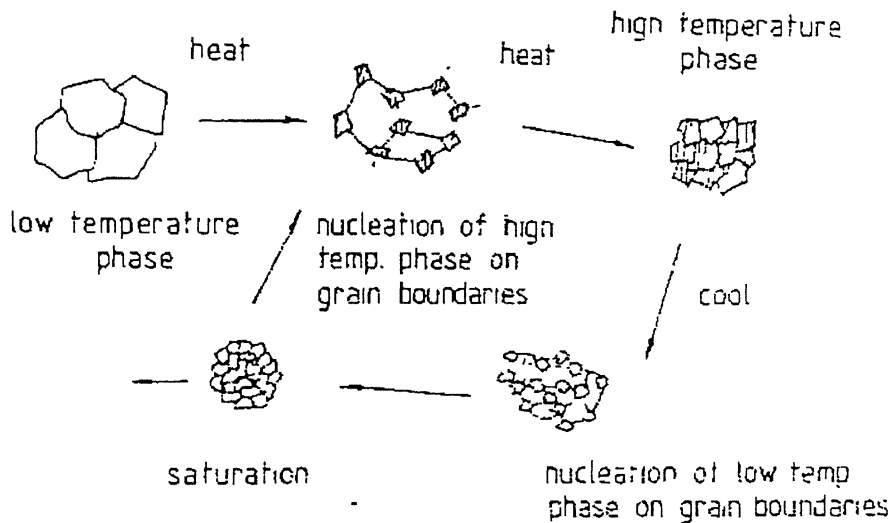
Fig 11 Schematic illustration of the microstructural changes that occur during grain refinement by phase transformation on thermal cycling.

Controlled rolling coupled to phase transformation has been successfully exploited in high strength low alloy steel, ultra-high carbon steels and could equally be applied in the Cu-Al based alloys where the eutectoid transformation occurs on cooling.

2.3.3.3 Grain refinement by phase separation

It is often possible to anneal duplex material at a temperature where only one phase is stable. Quenching the resulting single phase structure will then either effect a martensitic transformation or produce a supersaturated solid solution. A subsequent annealing treatment will result in the separation of the two equilibrium phases from the metastable microstructure. If sufficient nucleation sites are available then a fine grain microstructure

is produced. A martensitic structure, such as that formed on quenching α/β titanium alloys from the β phase field, provides such a density of potential nucleation sites for the α grains and hence aids the change of the $\beta' - Ti$ to the equilibrium α+β phases. Another example of grain refinement by phase separation is the spinoidal decomposition of Zn-22%Al. Slow cooling the Zn-Al alloy results in a lamellar eutectoidal decomposition product with very poor superplastic properties. If however, the alloy is quenched to room temperature a supersaturated solid solution of Al in Zn is formed which decomposes in a spinoidal fashion producing a very fine grain, highly superplastic, microstructure [20,21]

Despite the wide variety of methods available for developing fine grain microstructures, only a very small number of upwards of 100 distinct alloys which show extensive superplasticity are, or have the potential to be, exploited on a commercial scale. These include medium to high strength aluminum alloys, some duplex titanium alloys and ultra-high carbon and stainless steels.

2.3.4 Variables of Deformation

Load, grain size and temperature are the three important independent variable where stress, strain rate strain constitutes the list of dependent variables [21].

As the stress level are determined solely by the magnitude of the load applied , discussion in terms of the latter independent variable is felt to be unnecessary. Therefore, for obtaining a clear picture the dependent variables should be considered as functions of grain size and temperature.

At a given temperature, the flow stress of an alloy in the superplastic state is about 10 percent of the flow stress of the same alloy in the non-superplastic condition. In general stress is related to strain rate through eq. 1.1. The stress at a given strain rate and temperature decreases with decreasing grain size (Fig 12.). The dependence of stress on grain size can be described by the relation

$$\sigma\,|_{\varepsilon,T} \, \propto \, L^a \qquad \text{... 1.19}$$

where L is the grain size and a is a constant lying in the range 0.5 to 3.0.

for a given strain rate and grain size the flow stress decreases with increasing temperature. The bulk of evidence is that the temperature dependence follows an exponential relationship from which an apparent activation energy can be deduced.
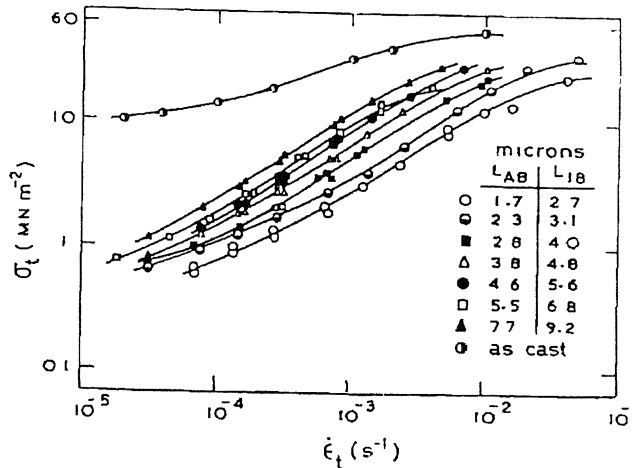
Fig 12 The stress vs. strain rate relation for various grain sizes at 793 K for hot worked and annealed Al-CuAl$_2$ eutectic alloys [3]

2.3.4.1 Strain rate

In general, uniform strain and secondary creep rate increase with decreasing grain size. Under conditions of optimal superplasticity the relation

$$\varepsilon\,|_{\sigma,\,T} \propto 1/L^b \qquad \text{..................................... 1.20}$$

with b having the values 1 to 5 is applicable. It follows from simple dimensional analysis that since m is less than unity, b in equation 1.20 should be greater than a in equation 19. When m was independent of strain rate b was equal to 2 over wide ranges of temperature and strain rate. Therefore, the spectrum of values obtained from b could be attributed to the simultaneous variation of m with strain rate and/or grain size. A similar comment is applicable in case of the variation of flow stress with grain size discussed earlier. In

general an increase in strain rate is equivalent to an increase in grain size and has a deleterious effect on superplastic properties.

The strain rate increases exponentially with temperature and as in the case of stress an apparent activation energy is often obtained from the temperature dependence of strain rate.

2.3.4.2 Strain

Irrespective of whether the superplastic effect was achieved by grain refinement, high temperature or low strain rate, superplastic creep caused no increase in the low temperature yield stress above that annealed material. On the other hand, hardening was observed after normal rate insensitive creep which increased with strain rate. Finer grained material, however, exhibited greater recovery. Under optimal condition thermal or thermomechanical history did not influence superplastic properties so long as the independent variables are unaltered. During low temperature deformation, however, the strain hardening has been reported [13]

Watts and Stowell [14] , however, obtained a significant linear strain dependence of flow stress and the relationship

$$\sigma = \sigma_I + \alpha\varepsilon \quad \dots\dots\dots\dots\dots\dots\dots\dots\dots\dots\dots\dots\dots\dots\dots \text{1.21}$$

With σ_I equal to the stress for zero strain at a given strain rate and α a slowly varying function of strain rate, is valid under these conditions. Time dependent grain coarsening was shown to be responsible for this type of dependence. It is therefore, cautioned that if the effect of grain growth, which usually is macroscopically manifested by a strain dependence of stress, is neglected spurious in $\ln\sigma$ -$\ln\varepsilon$ relations, m values etc. will results. It is interesting to note in this regard that superplastic deformation was essentially strain independent when structural changes were absent. Nevertheless, there are some situations where strain is considered to be important on account of dynamical effects.

2.3.4.3 Temperature

The temperature dependence of both stress and strain rate appear to be exponential. Empirically there are two alternatives expressions available to describe the temperature dependence, viz.,

$$\varepsilon \mid_{\sigma, L} \propto \exp(-Q_\sigma/kT) \quad \ldots\ldots\ldots\ldots\ldots\ldots\ldots\ldots\ldots\ldots 1.22$$

and

$$\sigma \mid_{\varepsilon, L} \propto \exp(Q_\varepsilon/kT) \quad \ldots\ldots\ldots\ldots\ldots\ldots\ldots\ldots 1.23$$

where the suffixes indicate the variables that are maintained constant and Q is an activation energy. However, for the above equations to be rigorously applicable to the superplastic flow m should be independent of temperature. As the experimental evidence reviewed earlier suggests that the temperature dependence of m can be considerable in the region of optimal superplastic deformation both the activation energy at constant stress Q_σ and the activation energy at constant strain rate, Q_ε, are apparent and will be different from the real activation energy for the process. Moreover, as m is less than unity, Q_σ will be greater than Q_ε and the ratio of the latter to the former will approximately be equal to the strain rate sensitivity index, m.

2.4 Cavitation In Superplasticity

When a superplastic material fails during tensile deformation it is either the result of unstable plastic flow or a consequence of the growth and interlinkage of internally nucleated voids. In the former process, inhomogenities in the cross-sectional area of a test piece lead to a localized increase in the strain rate and the strain rate and the difference in the cross sectional area increase. The rate at which the discontinuity in the cross sectional area increases depends on both the rate of strain hardening and the strain rate sensitivity. In the superplastic materials, where true strain hardening is minimal, any neck which is present will always grow, although the rate of growth decreases with increasing m. unstable plastic plastic flow normally results in the material pulling out to a fine point prior to failure (fig. 13). Where failure occurs as the results of the nucleation, growth and

interlinkage of internal voids, the fracture surface is much more adrupt. The value of the strain rate sensitivity is important in determining the rate at which the voids grow and thus to some extent controls the elongation to failure in system which undergo cavitation.
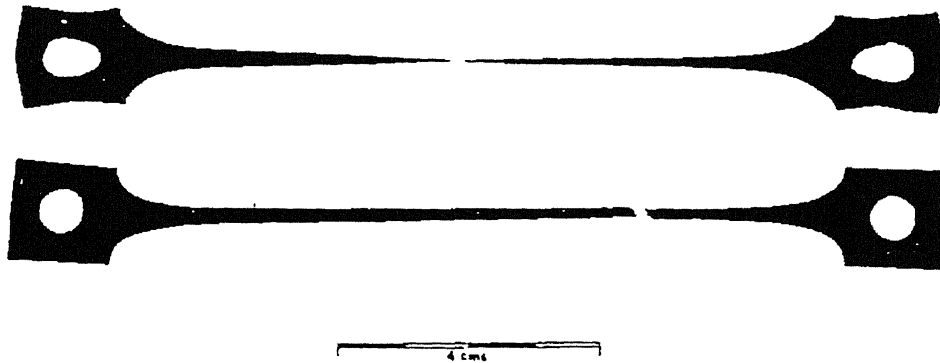
Fig 13 Shadowgraph of the fracture in two superplastic alloys after 900 % tensile elongation. (a) unstable plastic flow in Ti-6Al-4V and (b) pseudo brittle fracture by cavitation in Supral 220 [22].

2.4.1 General Characteristics Of Cavitation

Despite the large plastic strains which can be obtained in superplastic materials it is now well established that cavitation may occur during superplastic flow. The alloys in which cavitation has been observed include those based on aluminum, copper, iron, lead silver titanium and zinc. The subject of cavitation in superplasticity has been reviewed extensively both from experimental and theoretical viewpoint. In general, cavities nucleate at the grain boundaries and their subsequent growth coalescence invariably leads to premature failure. However, and more importantly from practical viewpoint, the presence of cavities in superplastically formed components could adversely affect their mechanical properties. There is also evidence that cavities may develop from defects which pre-exist, and which are usually produced during the thermomechanical processing required to develop a superplastic microstructure [22].

An important requirement for cavitation during superplastic flow is the presence of a local tensile stress. Under the conditions of homogeneous compression cavitation is not observed, and cavities which are produced during superplastic tensile flow are removed during subsequent compressive flow. Superplastic closed die isothermal forging of Ni – based superalloys such as IN 100, starting from hot pressed powders which are heavily worked by extrusion, is used in the manufacture of turbine discs to give a sound cavity free product of uniform microstructure. It has also been demonstrated that the superimposition of hydrostatic pressure during both uniaxial and biaxial superplastic tensile flow can reduce or eliminate cavitation [23]. The cavitation damage which develops during superplastic forming can also be removed by a post-forming hot isostatic pressing treatment which will sinter the voids. In order to control cavitation it is therefore necessary to understand both the microstructural and deformation parameters. Which influences its occurrence and magnitude.

In the majority of the studies on cavitation only the variation of the total volume fraction of cavities with strain at different strain rates and temperature has been studied. It should be noted that the volume fraction of cavities, Cv, can be written as

$$C_V = \Sigma \, N_{vl}.V_l \quad \text{.. 1.22}$$

Where N_{vl} is the number of cavities per unit volume having a volume V_l. The number of voids of any particular size is related to the number of pre-existing voids and to the nucleation rate, while the volume of a particular void is controlled essentially by the growth rate. However, during the latter stages of deformation when the cavitation level is high (approaching to 10%), the growth process is affected by the spatial distribution of the voids through void coalescence. Hence growth becomes, in part, dependant on nucleation process. It is therefore evident that the variation of the volume fraction of voids with strain, strain rate and temperature is not a simple one. The effect of changing the strain rate and temperature at which deformation occurs may be further complicated by other factors such as grain growth and/or a change in phase proportion[24,25].

27

The morphology of cavities formed during superplastic flow varies from one material to the next and even in the same materials deformed at different strain rates. In general, three types of cavities have been observed in superplastic materials. These are:

1. Superplastic voids with radii up to ~ 100μm.

2. Elliptical voids elongated parallel to the tensile axis with lengths up to ~ 50 μm and aspect ratios from 2:1 to 10:1

3. Groups of angular or crack like cavities, each up to 10 μm in length, interlinked around cluster of grain.

The cavity morphologies have been cited as evidence for the operation of different void growth mechanism. The circular section voids have often been taken to infer diffusional growth, while the elongated elliptical section voids are thought to e indicative of strain-controlled growth. However, there have been few systematic studies or quantitative analysis of the evolution of void size and shape during superplastic flow.

Unfortunately, observations of cavities at the nucleation stage are usually difficult to make. Cavities do not form uniformly throughout the microstructure and information concerning nucleation has to be deduced from specimen in which the voids have grown to a size where they are resolvable, either by direct observation or by the measurement of physical properties of the base material. Since cavities do not nucleate always during superplastic flow and, with only very specific exception, will always grow during tensile superplastic deformation, the mechanism of cavity growth will be examined prior to consideration of the nucleation process.

2.4.2 Cavity Growth

2.4.2.1 Diffusion Controlled Growth

A cavity located on a grain boundary, whether nucleated during superplastic flow or pre-existing, may grow by stress directed vacancy diffusion, by plastic deformation of the surrounding matrix or by a combination of both these mechanism. The former process has been analyzed by several workers [26, 27] for the case of spherical voids under uniaxial tension and leads to a relationship of the form

$$Dr/d\varepsilon = D_{gb}\delta\Omega/kT\varepsilon r^2 \ [\sigma_1 - 2\Gamma/r] \ 1/\ln(1/2r) -3/4 \quad \dots\dots\dots\dots\dots\dots \ 1.25$$

Where σ_1 is the maximum principal stress local to the grain boundary, Ω is the atomic volume, Γ the surface energy and r the cavity radius. The driving force for cavity growth is provided by the difference in chemical potential between an atom on the stressed grain boundary and that on the free surface of the void. When the maximum principal stress is tensile, atoms move from the void surface to the grain boundary and the void will grow (fig 14)
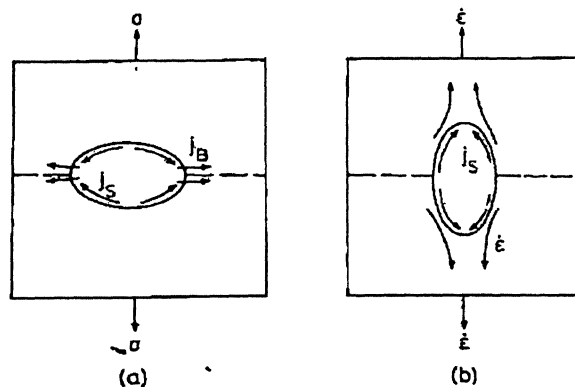
Fig 14 Schematic illustration of cavity (void) growth process for (a) diffusion controlled growth, (b) strain controlled growth. [6]

The relationships derived in the literature differ only the form of the last term containing solely r and 1, the size and spacing of the voids. In deriving relationships of the form of equation it has been assumed that the voids are widely spaced on fixed boundaries oriented perpendicular to the applied stress axis and are themselves small relative to the grain size of the material. It is evident from Equation 1.15 that the rate of void growth decreases as the inverse square of the cavity radius of the cavity radius and thus slows considerably as the voids grow. In the majority of superplastic materials, void have dimension similar to that of the grain size. Furthermore, the cavities are usually located on sliding boundaries which are oriented randomly with respect to the applied stress. It was proposed by Miller and Langdon that when the void diameter was the same as the grain size, then the growth rate would be enhanced by additional mass transfer along boundaries intersecting the surface of the void. Such enhancement was later shown to be sensitive to the ratio of the void size to the grain size. The rate of void growth is then given by

$$Dr/d\varepsilon = 45 \ D_{gb}\delta\Omega/kTd^2 \ [\sigma_1/\varepsilon] \quad \dots\dots\dots\dots\dots\dots\dots\dots\dots\dots 1.26$$

Where d is the grain size. Unlike the previous equation, the rate of change of void radius with strain rate is independent of the void radius, r.

Equations 26 and 27, which were initially derived for the case of uniaxial tension, can be written in more general terms allowing the effects of multiaxial states of stress and alternative geometries of deformation to be considered. The maximum principal stress σ_1, can be redefined in terms of the Von Mises equivalent stress, σ_E and the superimposed pressure, P, i.e.

$$\sigma_1/\sigma_E = [k_D/3 - P/\sigma_E] \quad \dots\dots\dots\dots\dots\dots\dots\dots\dots \quad 1.27$$

Where k_D is a geometric factor that depends on the mode of deformation and the extent of grain boundary sliding.

2.4.2.2 Plasticity or Strain Controlled Growth

For cavity growth by deformation of the surrounding matrix in uniaxial tension, the relationship

$$Dr/d\epsilon = \cap/3 \ [r - 3\Gamma/2\sigma_3] \ \ldots\ldots\ldots\ldots\ldots\ldots\ \ldots\ \ldots\ldots 1.29$$

Has been proposed, where $\cap$, the cavity growth rate parameter, is dependent on both the applied stress state and the geometry of deformation. Unlike diffusion controlled cavity growth, the rate of void growth increases linearly with void size. Plasticity dominated void growth is controlled by the mean stress rather than the maximum principal stress.

The parameter $\cap$ has been determined theoretically by several workers for the case of uniaxial tension with values ranging from 1.22 through 1.25 to 3 [28]. following the analysis of Rice and Tracy [29] it can be shown that

$$\cap/3 = 0.5585 \sinh [\ 3\sigma_m/2\sigma_E \ ] + 0.008 [\ -3\epsilon_2/\epsilon_1-\epsilon_3 \ ]\cosh [3\sigma_m/2\sigma_E] \ldots\ldots\ldots\ldots 1.30$$

where σ_M is the mean stress,ϵ_1, ϵ_2 and ϵ_3 are the principal strain rates,ϵ_E the von mises equivalent stress.. Rice and Tracy showed that $\cap$ would be equal to 0.9 for uniaxial tension, 1.65 for plane strain and 1.92 for balanced biaxial tension in a perfectly plastic solid (m=0). Alternatively, Buianski et al. predicted that $\cap$ would take different values depending on the magnitude of the strain rate sensitivity. For example, in balanced biaxial tension, which would arise in the case of blowing a hemisphere from a circular disc of material, Budianski et al. calculated that $\cap$ would equal 1.75 when m = 0.5; 1.94 when m= 0.33 and 2.64 when m = 0. Stowell et al. have also shown that value of $\cap$ is dependant on the strain sensitivity and hence vary with the strain rate. The relationship given by Stowell et al. for uniaxial tension can be readily extended to multiaxial states of stress. Following the analysis of Cooks and Ashby it can be shown that [30]

$$\cap = 3/2\ [(m+1)/m]\ \sinh\ [2[(2-m)/(2+m)][\sigma_M/\sigma_E]]\ \dots\dots\dots\dots\ 1.30$$

Or [31]

$$\cap = 3/2\ (1+0.93m-0.432m^2)^{1/m}[\sigma_M/\sigma_E]\ \dots\dots\dots\dots\dots\ 1.31$$

The term containing the ratio of the mean stress, σ_M to the Von Mises equivalent stress, σ_E, in equations 1.31 and 1.32 defines the triaxiality of stress local to the grain boundary. The form of this term is dependent on the geometry of deformation and may be rewritten in terms of geometric constant, K_S, and the superimposed hydrostatic pressure, P. Thus

$$\sigma_m/\sigma_E = [\ K_s/3 - P/\sigma_E]\ \dots\dots\dots\dots\dots\dots\dots\ 1.32$$

To establish the values of K_s and K_D appropriate to superplastic flow, two modes of deformation need to be considered. Firstly, the case of rigid grains where there is no grain boundary sliding and secondly, the case of freely sliding grains, where the state of stress on the grain boundaries is dependent on the extent of sliding. As the voids are located on the boundary they experience the local rather than the remote state of stress and thus their rate of growth is, to a large extent, dependent on the fraction of the total strain carried by the grain boundaries.

3. Experimental Procedure

Experimental procedure comprises mechanical testing, optical microscopy, stereological measurements and scanning electron microscopy. Fig. 3.1 shows the layout of the experimental procedure.

3.1 Materials

In this study the cavitation behavior of superplastic materials Cu-Zn-Al and Al-Mg were studied. The materials were received from Dresden Germany. The compositions of these materials are given below in table 3.1 and 3.2. The chemical analysis of the alloys were performed by using EDX on SEM

Table 3.1 Composition of Cu-Zn-Al alloy

Cu	Zn	Al	Si	Co
74.5%	23%	2%	0.4%	0.1%

Table 3.2 Composition of Al-Mg alloy

Al	Mg	Mn	Si	Cu
94%	4.90%	1%	0.4%	0.15%

3.2 Mechanical Testing

The tensile tests were carried out on an INSTRON 1195 testing machine at a constant crosshead velocity. The tensile tests were carried out at 550°C and 400°C for Cu-Zn-Al and Al-Mg materials respectively. These temperatures are just above the recrystallisation-temperature of these alloys at which such alloys exhibit superplasticity at a temperature above the recrystallisation-temperature. A resistance furnace had been used to obtain the temperature. The full-scale load was set to 0.1 kN for all tests. The tensile tests were conducted at two crosshead velocities, 0.1 $mm^{-1}min^{-1}$ and 0.5 $mm^{-1}min^{-1}$, which produced initial strain rates of $2\times10^{-4}s^{-1}$ and $2\times10^{-2}s^{-1}$ respectively. The dimensions of the samples are give in tables 3.3 and 3.4. Load versus time plots were recorded on a chart recorder connected to the INSTRON machine.

Table 3.3 Dimension of Cu-Zn-Al tensile samples

Gauge Length, mm	Width,mm	Thickness,mm
8.5	4	4

Table 3.4 Dimension of Al-Mg tensile samples

Gauge Length, mm	Width,mm	Thickness,mm
8.33	4	1.75

3.3 Optical Microscopy

Optical microscopy was used for microstructural study at low magnifications. The tested samples were ground using a belt grinder followed by polishing on emery sheet of various grades (1/0 to 4/0). The paper polished samples were then wheel polished using a suspension of alumina powder of 0.3μm. The polished Cu-Zn-Al samples were etched by $FeCl_3$ solution and Al-Mg samples are etched by Kellar solution. The prepared samples were used for microstructural study by optical microscopy. In optical microscopy the samples were observed at low magnifications of 200X and 500X. At this magnification the morphology and distribution of cavities were conveniently studied. The micrographs were taken along the gauge length by a CCD camera, attached to the optical microscope (Axiolab Zeiss Optical Microscope).

3.4 Stereological Measurements.

Image-pro plus imaging software tool was used for acquiring the microscope images and making subsequent stereological measurements. The captured images were processed to quantify the morphology of the cavities produced during superplastic deformation. The parameters selected for measurement are volume fraction and aspect ratio of the cavities. In this study the stereological relation used for measuring volume fraction of cavities :

Volume Fraction = point Fraction

Using image analysis, it was possible to make manual measurements of the point fraction of the cavities.

Aspect ratio of the cavities is the ratio of major axis of the cavity to its minor axis. The tools of imaging software measured this ratio automatically. The grabbed microscope images are adjusted by changing brightness and contrast. Then filter tools were used. Filtering of the images makes the cavities in the images isolated from the matrix.

3.5 Scanning Electron Microscopic analysis.

The fracture surfaces of tested samples were studied using JSM – 840A Scanning Electron Microscope. The samples were mounted vertically by fixing them on to an Al block using an adhesive. This block was placed on the specimen holder and suitable packing was used to prevent any movement of the sample. The fracture surfaces were examined at magnifications ranging from 400X to 5000X.

```
┌─────────────────────────────┐
│   As received sample with   │
│   Various rolling direction. │
└─────────────────────────────┘
              │
              ▼
┌─────────────────────────────┐
│ Tensile testing at $2\times10^{-2}s^{-1}$ and │
│ $2\times10^{-4}s^{-1}$.     │
│  Testing temperature 550°C. │
└─────────────────────────────┘
              │
              ▼
┌─────────────────────────────┐
│                             │
│   Material characterization │
│                             │
└─────────────────────────────┘
```

| Optical microscopy to observe cavity distribution and morphology. | Stereological measurement For cavity volume fraction And aspect ratio estimation | SEM for fracture surface study. |
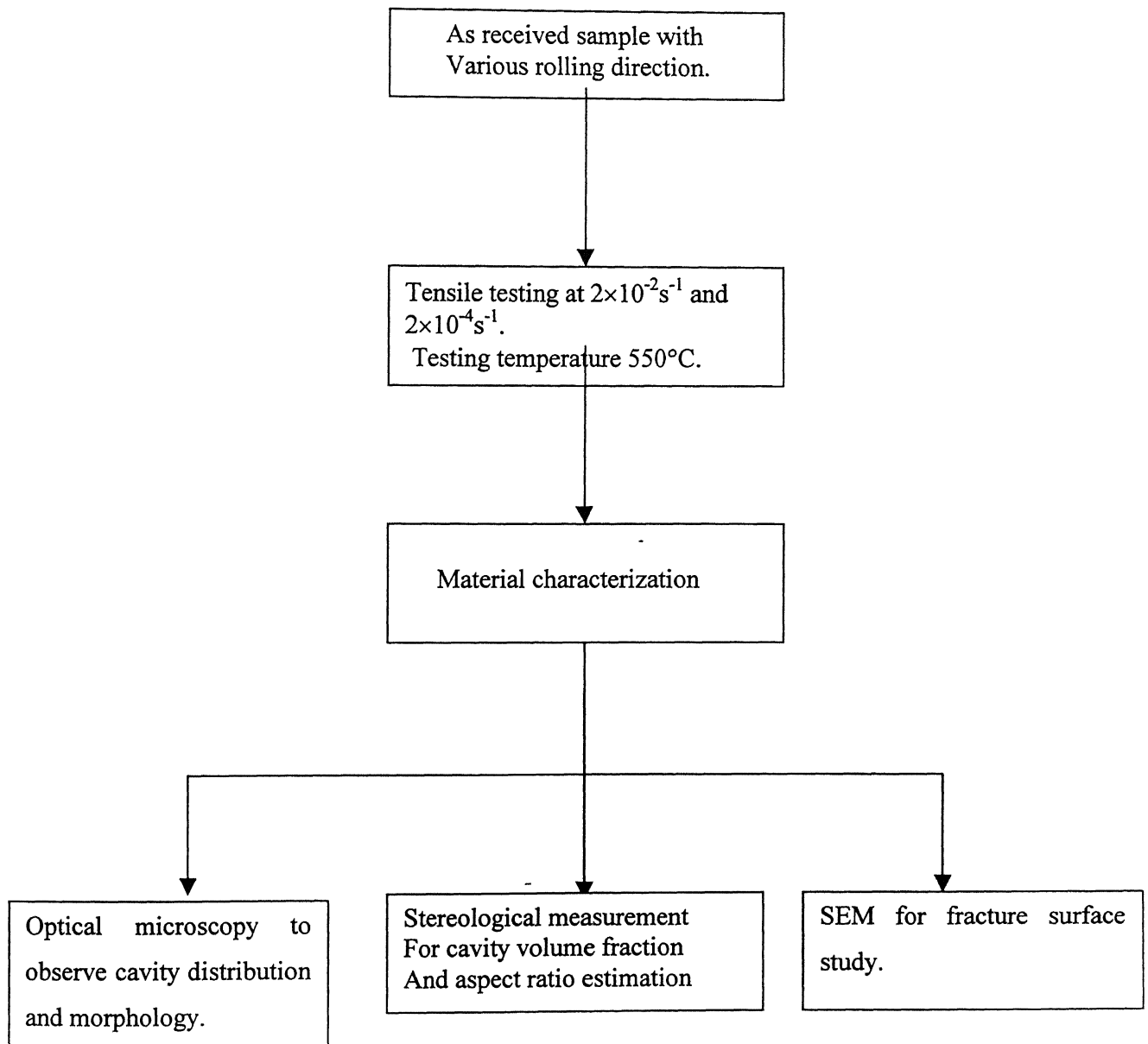
Fig 3.1 Layout of the experiments

4. Results and discussion

4.1 As received samples

Figs. 4.1a and 4.1b show the micrographs of Cu-Zn-Al samples having rolling direction normal to tensile axis, parallel to tensile axis and 45° angle to tensile axis respectively. Each micrograph shows evidence of pre-existing cavities. These pre-existing cavities play an important role in cavity nucleation. Because cavity nucleation is favored by the presence of second phase particles and pre-existing pores or cavities. Pre-existing cavities were not observed in Al-Mg sample.

4.2 Tensile test

4.2.1 Cu-Zn-Al samples

The results of high temperature tensile testing of Cu-Zn-Al are given in the table 4 1 The elongations of the materials are not ideally characteristic of superplastic behavior. Because in superplastic deformation the elongation is typically in excess of 200%. The pre-existing cavities, as mentioned in the previous section may be the prime cause of premature failure.

Figs. 4.2a and 4.2b show the variation of true stress with true strain. From these figures, it is evident that the stress-strain behavior is similar for all the three samples (i.e. normal, parallel and 45° angle) and for both strain rates (i.e. 2×10^{-2} s^{-1} and 2×10^{-2} s^{-1}). It is also apparent that the flow stress is almost independent of strain in all cases. In ideal superplastic deformation the flow stress is completely independent of strain. The rate of change in cross section can be expressed as (refer to section 2).

$$-(dA/dt) = (P/C)^{1/m} (1/A^{(1-m)/m}) \qquad \text{Eq 3.1}$$

where P is axial load, C is a constant, A is the cross sectional area, m is strain rate sensitivity. In ideal superplastic deformation m should be unity so dA/dt is independent of A. An increase in the flow stress is indicative of strain enhanced grain growth while a decrease in the flow stress, particularly at high strains can often be related to the development of cavitation damage.

Table 4.1 Tensile tests data of Cu-Zn-Al alloys.

No.	Direction of tensile axis w.r.t Rolling direction	Strain rate s^{-1}	Testing Temperature	Elongation
1	Normal	2×10^{-2}	550°C	141%
2	Parallel	2×10^{-2}	550°C	138%
3	45 degree	2×10^{-2}	550°C	133%
4	Normal	2×10^{-4}	550°C	145%
5	Parallel	2×10^{-4}	550°C	144%
6	45 degree	2×10^{-4}	550°C	140%

4.2.2 Al-Mg materials

The results of tensile high temperature tensile test are given in table 4.2. The difference of these results with the results of Cu-Zn-Al alloy is that the elongation of Al-Mg Alloy, tested at higher strain rate, i.e., $2\times10^{-2}s^{-1}$ is higher than that at lower strain rate, i.e., $2\times10^{-4}s^{-1}$. This is due to the fact that the value of strain rate sensitivity, m, for Al-Mg alloy is closer to unity at higher strain rate [32]

Figs. 4.3a to 4.3d show the variation of true stress with true strain. From these figures, it is evident that the stress-strain behavior is similar for all the three samples (i.e. normal, parallel and 45°angle) and for both strain rates (i.e. 2×10^{-2} s^{-1} and 2×10^{-2} s^{-1}). It is also apparent that the flow stress is almost independent of strain in all cases. The reason for this behavior has been discussed in the previous section.

Table 4.2 Tensile tests data of Al-Mg alloys.

No.	Direction of tensile axis w.r.t Rolling direction	Strain rate s^{-1}	Testing Temperature	Elongation
1	Normal	2×10^{-2}	400°C	200%
2	Parallel	2×10^{-2}	400°C	210%
3	Normal	2×10^{-4}	400°C	165%
4	Parallel	2×10^{-4}	400°C	170%
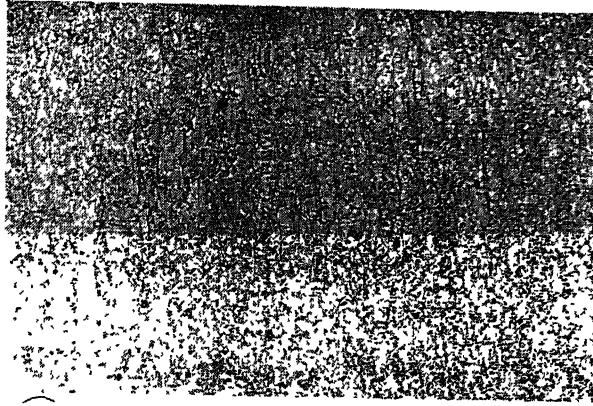
Fig 4.1a As received Cu-Zn-Al sample having rolling direction normal to the tensile axis.
Magnification 200X.
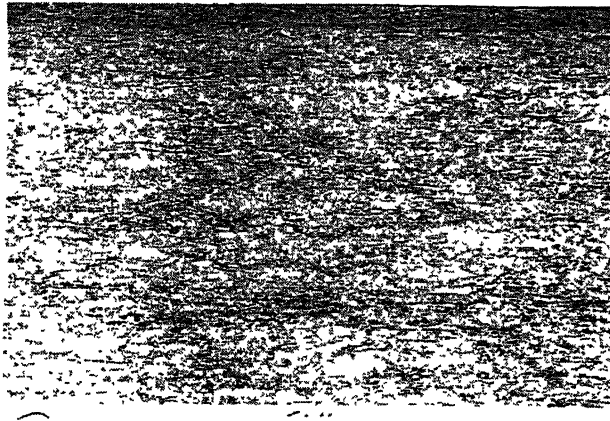
Fig 4.1b. As received Cu-Zn-Al sample having rolling direction parallel to the tensile
axis. Magnification 200X
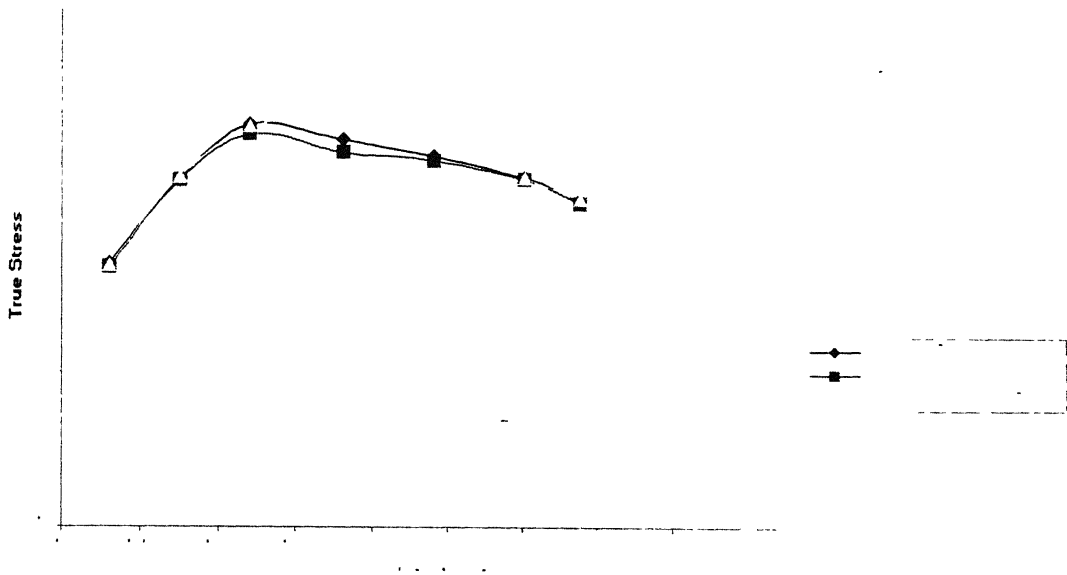
Fig. 4.2a The Variation of True Stress with True Strain For the Cu-Zn-Al Samples Tested at a Strain Rate of 2x10⁻²s⁻¹
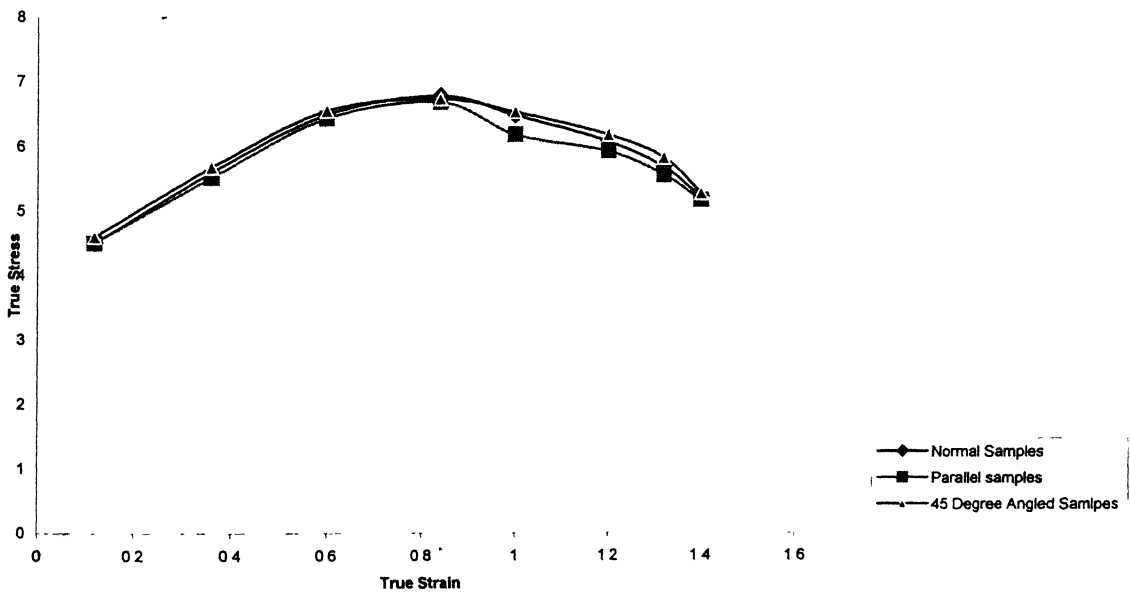
Fig. 4.2b Variation of True Stress with True Strain for the Cu-Zn-Al Samples Tested at a Strain Rate of 2x10⁻⁴s⁻¹
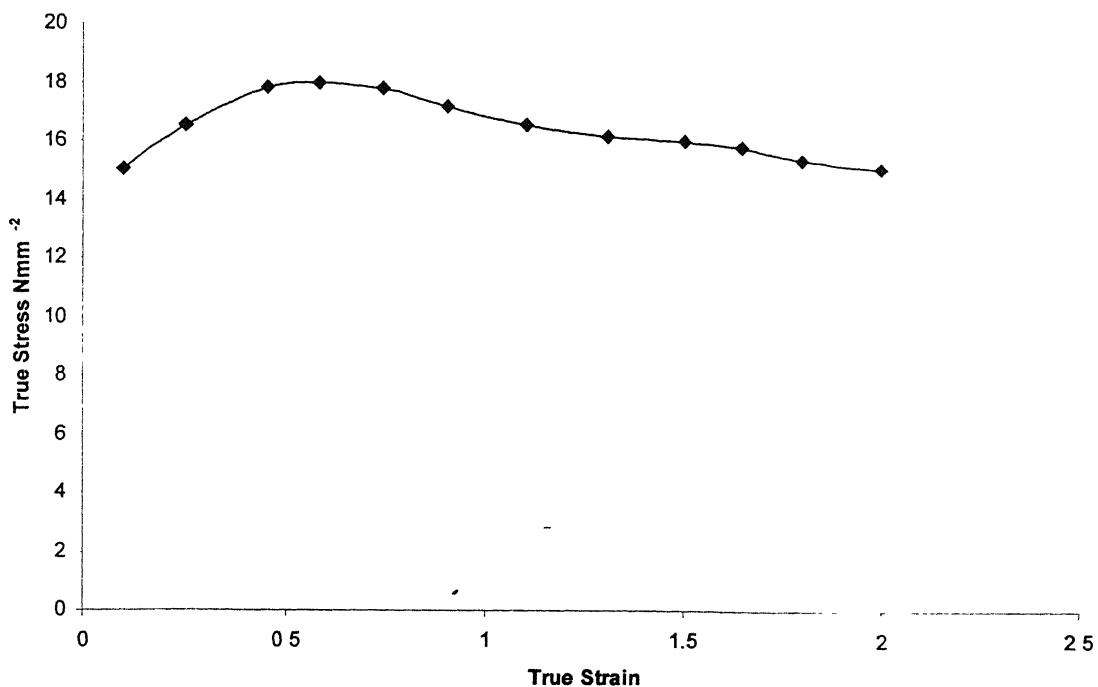
Fig 4.3a The variation of true stress with true strain for the Al-Mg tensile sample, having a orientation normal to the rolling axis, tested at a strain rate of $2 \times 10^{-2} s^{-1}$
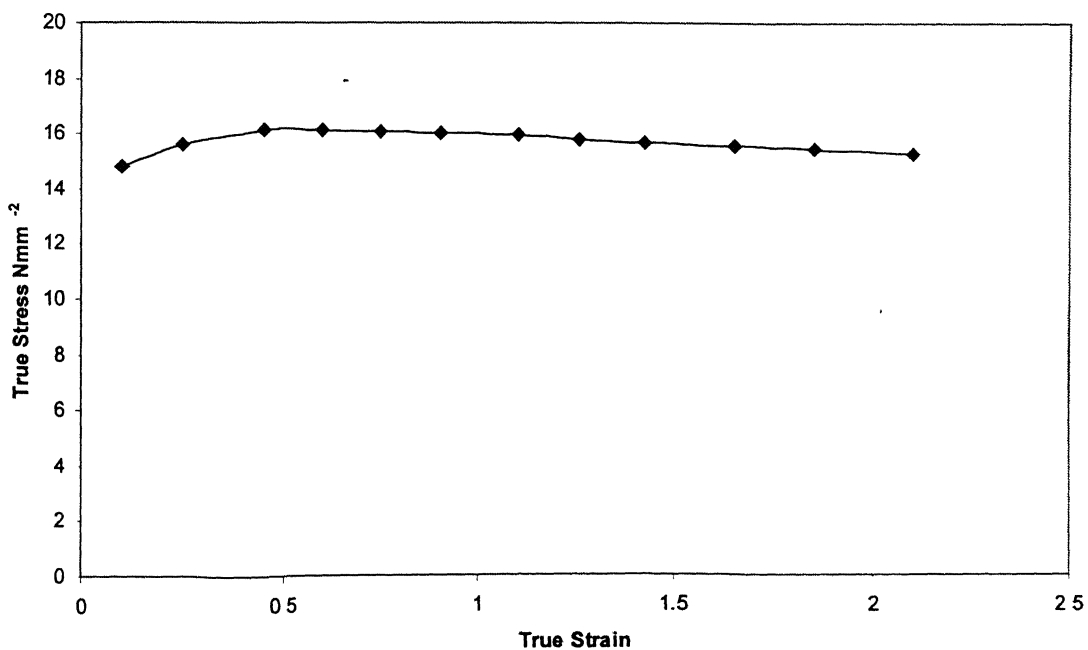
Fig. 4.3b The variation of true stress with true strain for the Al-Mg tensile sample, having a orientation parallel to the rolling axis, tested at a strain rate of $2 \times 10^{-2} s^{-1}$.
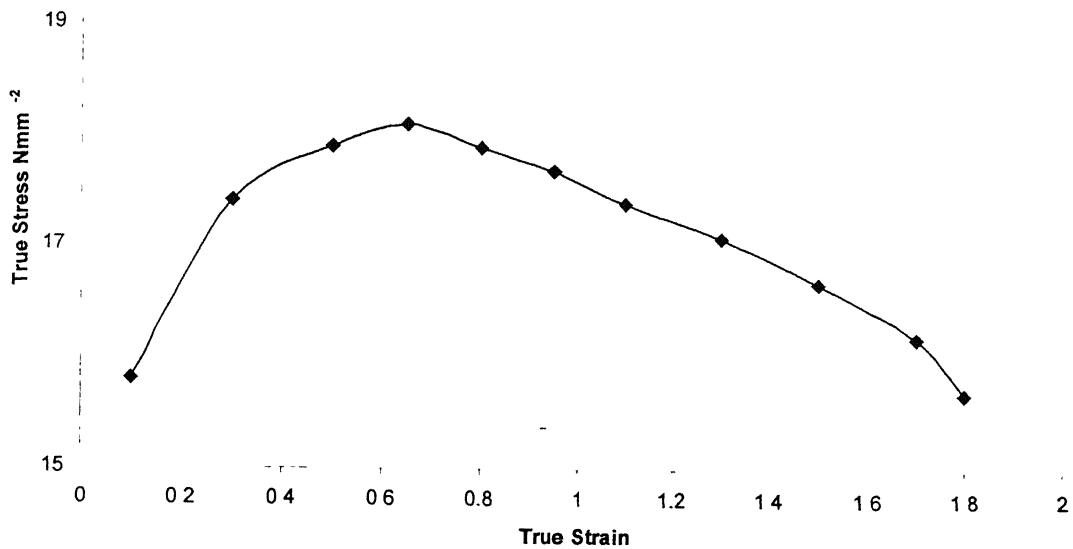
Fig. 4.3c The variation of true stress with true strain for the Al-Mg tensile sample, having a orientation parallel to rolling axis, tested at a strain rate of $2x10^{-4}s^{-1}$
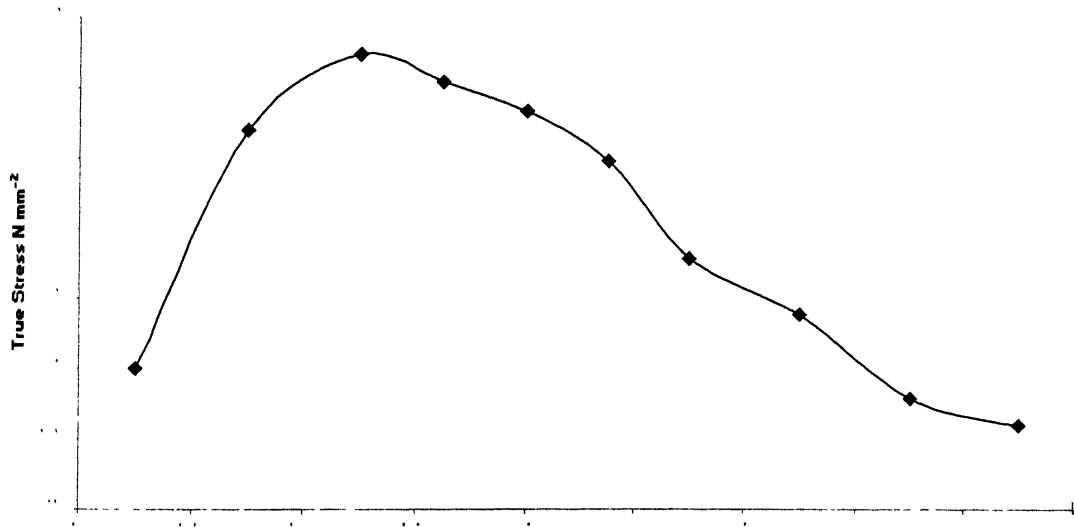
Fig. 4.3d The variation of true stress with true strain for the Al-Mg samples, having a orientation normal to the rolling axis, tested at a strain rate of $2x10^{-4}s^{-1}$

4.3 Fracture Surface Study

4.3.1 Cu-Zn-Al Alloy

Tensile samples normal to rolling direction.

Figs. 4.4 and 4.5 show typical fracture surfaces of the samples having tensile gauge length normal to the rolling direction. All micrographs of the fracture surfaces showed dimpled nature, which is a characteristic of ductile fracture. Figs. 4.4a to 4.4d show the fracture surfaces of the samples which are tested at the strain rate of 2×10^{-2} s^{-1}. Fig. 4.4a shows that the relief of grain has taken place. This is the outcome of the grain boundary sliding. To accommodate this movement, grains rearrange their position. Due to this rearrangement some grains are uplifted leading to grain relief. It can also be seen that cavities are accompanied with grain boundary sliding. This is prominent in the Figs. 4.4b and 4.4d. This elucidates the fact that cavities are formed due to lack of accommodation resulting from grain boundary sliding. Fig. 4.4c shows an example of interconnection of cavity. Due to this coalescence of cavities the failure takes place.

Figs. 4.5a to 4.5f show the fracture surfaces of the samples tested at lower strain rate i.e. in 2×10^{-4}s^{-1}. The basic difference of these surfaces from the previous surfaces is that there is less evidence of interconnectivity of the cavities. Fig. 4.5b shows the fracture surface at 400X magnification and supports the fact (see the arrow mark). At lower strain rate diffusion controlled cavity growth is more prevalent than strain induced cavity growth. Details of this mechanism have been discussed in section 2.4.2. This fact may be deduced from the observation that coalescence of cavities occurs at lower strain rate. In lower strain rate deformation, the rate of deformation is lower and for this reason mass transfer via diffusion can easily take place. That makes the cavities more regular shaped and isolated. Figs. 4.5a, 4.5c and 4.5e show that grains are more or less equiaxed. This is due to the fact that the grains undergoing superplastic deformation are not subjected to

elongation. In superplastic deformation grain growth does not take place. However, dynamic recrystallization and recovery occurs resulting in equiaxed grains. Fig. 4.5b clearly shows that cracks propagate along the grain boundary. This supports the fact that in superplastic deformation failure is occurs due to intergranular propagation of cracks. Since the tensile tests had been carried out at a temperature higher than 0.4 T_M, the region near the grain boundary is weaker than the grain interior. Due to this fact, crack is initiated near the grain boundary region. The occurrence of grain relief as in higher strain rate is also observed in the case of lower strain rate. Fig. 4.5f represents this phenomenon. The micrograph shows the upliftment of the grains.

Tensile samples parallel to rolling direction.

Figs. 4.6 and 4.7 show the fracture surfaces of the samples having the tensile gauge length parallel to the rolling direction and Figs. 4.6a and 4.6d are the micrographs of the samples tested at the strain rate of $2 \times 10^{-2} s^{-1}$. In this case as shown in Figs. 4.6b and 4.6c some facets have been observed. The facets are indicated by an arrow mark in the micrograph. Brittle fracture is characterized by separation normal to tensile stress. This type of separation forms facets. Therefore, Figs. 4.6b and 4.6c illustrates the fact that some brittleness has been incorporated. Fig. 4.6a shows the grain relief similar to that observed in the samples tested normal to the rolling direction. Fig. 4.6d shows the cavity interlinkage at the fracture surface. This interlinkage leads to the generation of discontinuity and reduces the load-bearing cross-section. These factors ultimately produce fracture of the material.

Figs. 4.7a to 4.7f are the micrographs of the samples tested at the strain rate of $2 \times 10^{-4} s^{-1}$. In this strain rate there is no evidence of brittleness in fracture surfaces like the higher strain rate case. Moreover it is also evident from Figs. 4.7b, 4.7d and 4.7e that the intensity of interlinkage of cavities is also lesser than in higher strain rate. As in the case of the sample normal to the rolling direction, grain relief is observed (see Fig. 4.7a) and grains do not get elongated (see Figs. 4.7a and 4.7c). Fig. 4.7f clearly shows a crack

propagating along grain boundary leading to intergranular mode of fracture (see the arrow mark).

Tensile samples oriented 45° angle to rolling direction.

Figs. 4.8 and 4.9 show the fracture surfaces of the samples having $45°$ angle with rolling direction. Figs. 4.8a to 4.8d show the fracture surfaces of the samples tested at the strain rate of 2×10^{-2} s^{-1}. All the micrographs represent the ductile mode of fracture. The fracture surfaces have essentially the same features as already discussed in the present cases. Figs. 4.9a to 4.9c show the fracture surfaces of the samples tested at the strain rate of 2×10^{-4} s^{-1}. In this case also (as for the normal and parallel samples) the extent of cavity interlinkage is lower than that of higher strain rate.

Fig 4.4a   Fracture surface of the Cu-Zn-Al sample, having tensile axis normal to the rolling direction, tested at a strain rate of $2\times10^{-2}\,s^{-1}$. Figure shows the uplilftment of grain (A)

Fig 4.4b   Fracture surface of the Cu-Zn-Al sample, having tensile axis normal to the rolling direction, tested at a strain rate of $2\times10^{-2}\,s^{-1}$.

Fig 4.4c   Fracture surface of the Cu-Zn-Al sample, having tensile axis normal to the rolling direction, tested at a strain rate of $2\times10^{-2}\,s^{-1}$.

Fig 4.4d   Fracture surface of the Cu-Zn-Al sample, having tensile axis normal to the rolling direction, tested at a strain rate of $2 \times 10^{-2} \, s^{-1}$.

Fig 4.5a Fracture surface of the Cu-Zn-Al sample, having tensile axis normal to the rolling direction, tested at a strain rate of $2 \times 10^{-4} \, s^{-1}$. Grains are tends to be equiaxed.

Fig 4.5b Fracture surface of the Cu-Zn-Al sample, having tensile axis normal to the rolling direction, tested at a strain rate of $2 \times 10^{-4} s^{-1}$.Cavities are isolated. The arrow indicates one such cavity.

50

Fig 4.5c Fracture surface of the Cu-Zn-Al sample, having tensile axis normal to the rolling direction, tested at a strain rate of $2 \times 10^{-4} s^{-1}$. Grains are more or less equiaxed.

Fig 4.5d Fracture surface of the Cu-Zn-Al sample, having tensile axis normal to the rolling direction, tested at a strain rate of $2 \times 10^{-4} s^{-1}$. Figure shows the evidence of intergranular crack propagation (arrow mark in the figure).

Fig 4.5e Fracture surface of the Cu-Zn-Al sample, having tensile axis normal to the rolling direction, tested at a strain rate of $2 \times 10^{-4} s^{-1}$. Grains are more or less equiaxed.

51

Fig 4.5f Fracture surface of the Cu-Zn-Al sample, having tensile axis normal to the rolling direction, tested at a strain rate of $2\times10^{-4}s^{-1}$. Shows dimpled nature of the fracture surface

Fig 4.6a. Fracture surface of the Cu-Zn-Al sample, having tensile axis parallel to the rolling direction, tested at a strain rate of $2\times10^{-2}s^{-1}$. Figure shows grain upliftment (A in the figure)

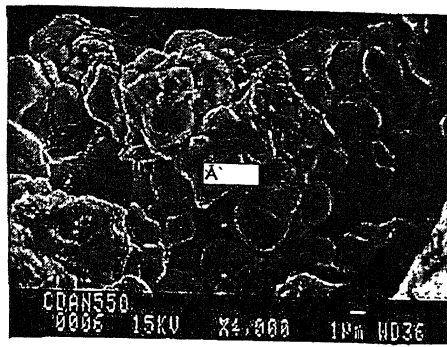Fig 4.6b. Fracture surface of the Cu-Zn-Al sample, having tensile axis parallel to the rolling direction, tested at a strain rate of $2\times10^{-2}s^{-1}$.

52

Fig 4.6c. Fracture surface of the Cu-Zn-Al sample, having tensile axis parallel to the rolling direction, tested at a strain rate of $2\times10^{-2}s^{-1}$. Figure shows facets (arrow mark in the figure), which indicates the incorporation of some amount of brittleness in the fracture mode.
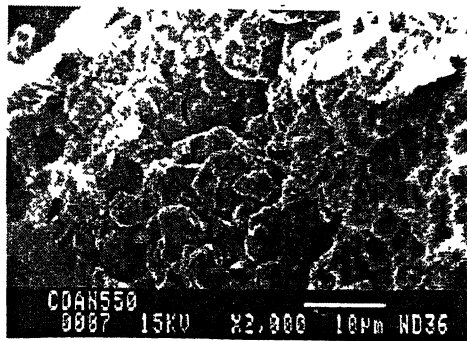

Fig. 4.6d Fracture surface of the Cu-Zn-Al sample, having tensile axis parallel to the rolling direction, tested at a strain rate of $2\times10^{-2}s^{-1}$. Figure shows cavity interlinkage (arrow mark in the figure) at fracture surface.
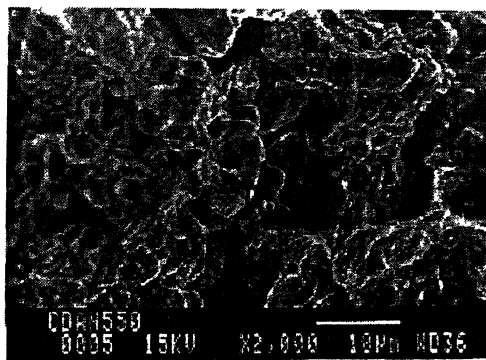

Fig 4.7a. Fracture surface of the Cu-Zn-Al sample, having tensile axis parallel to the rolling direction, tested at a strain rate of $2\times10^{-4}s^{-1}$. Figure shows upliftment of grains. (A in the figure)
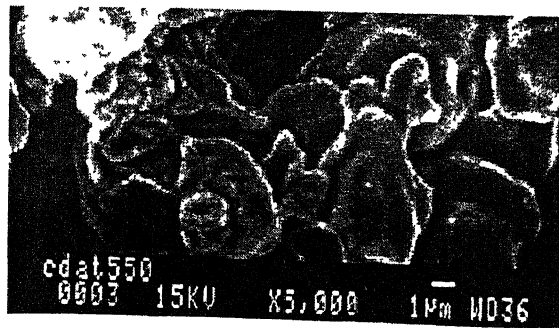
Fig 4.7b. Fracture surface of the Cu-Zn-Al sample, having tensile axis parallel to the rolling direction, tested at a strain rate of $2\times10^{-4}s^{-1}$. Figure shows that extent of cavity interlinkage is relatively lower than that of higher strain rate.

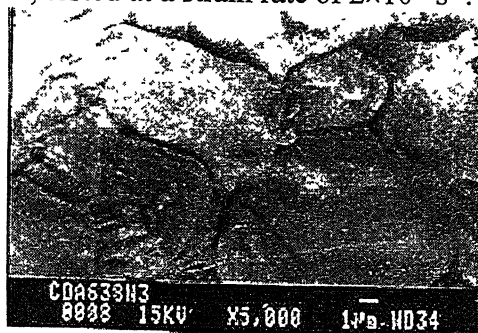Fig 4.7c. Fracture surface of the Cu-Zn-Al sample, having tensile axis parallel to the rolling direction, tested at a strain rate of $2\times10^{-4}s^{-1}$. Figure shows upliftment of grains. (A in the figure)

Fig 4.7d. Fracture surface of the Cu-Zn-Al sample, having tensile axis parallel to the rolling direction, tested at a strain rate of $2\times10^{-4}s^{-1}$.
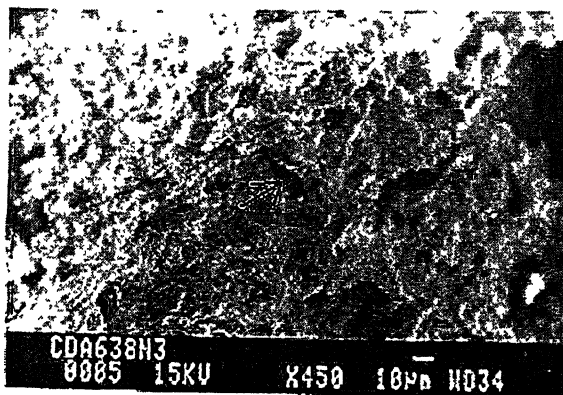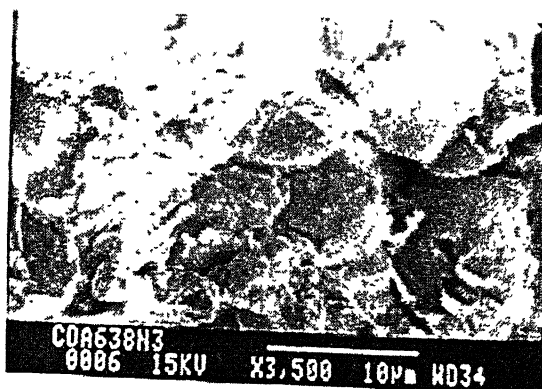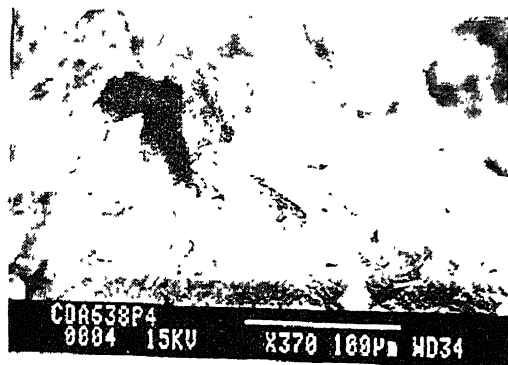
Fig 4.7e. Fracture surface of the Cu-Zn-Al sample, having tensile axis parallel to rolling direction, tested at a strain rate of $2\times10^{-4}s^{-1}$.
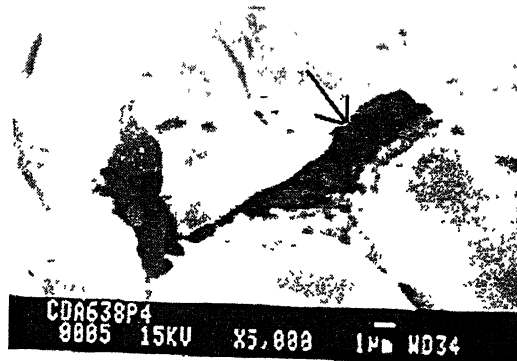
Fig 4.7f Fracture surface of the Cu-Zn-Al sample having, tensile axis parallel to rolling direction, tested at a strain rate of $2\times10^{-4}s^{-1}$. Figure shows the evidence of intergranular crack propagation (arrow mark indicate this feature).
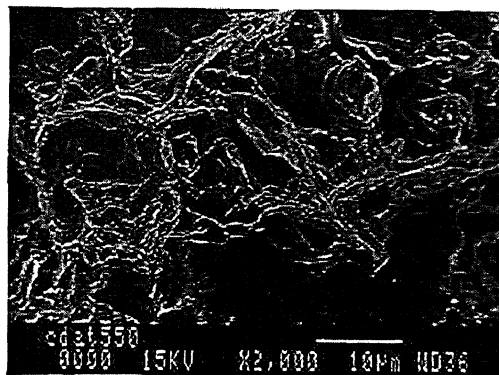
Fig 4.8a Fracture surface of the Cu-Zn-Al tensile sample, having tensile axis at an angle of 45° to rolling direction, tested at a strain rate of $2\times10^{-2}s^{-1}$.

55
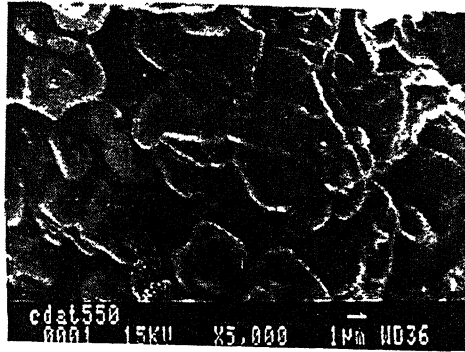
Fig 4.8b Fracture surface of the Cu-Zn-Al tensile sample, having tensile axis at an angle of 45° to rolling direction, tested at a strain rate of $2 \times 10^{-2} s^{-1}$.
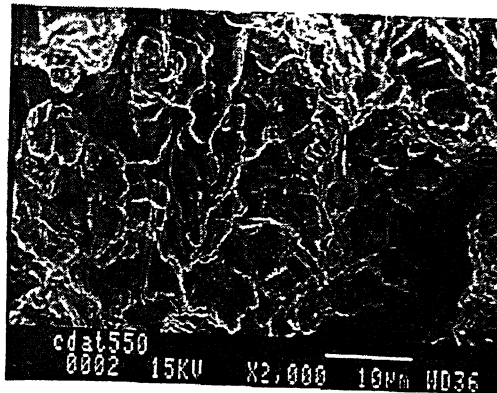
Fig 4.8c Fracture surface of the Cu-Zn-Al tensile sample, having tensile axis at an angle of 45° to rolling direction, tested at a strain rate of $2 \times 10^{-2} s^{-1}$.
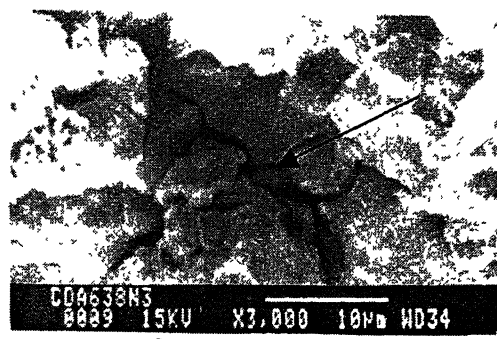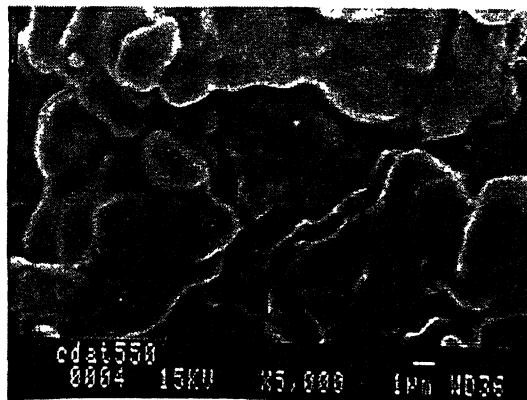

Fig 4.8d Fracture surface of the Cu-Zn-Al tensile sample, having tensile axis at an angle of 45° to rolling direction, tested at a strain rate of $2 \times 10^{-2} s^{-1}$.
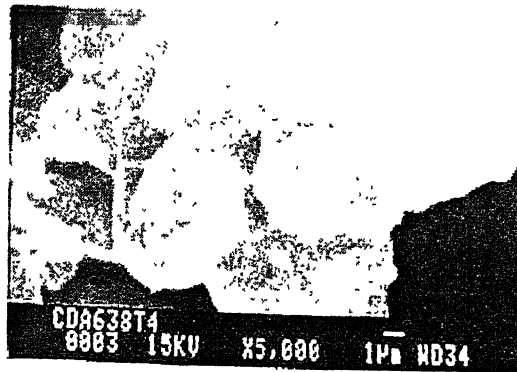
Fig 4.9a Fracture surface of the Cu-Zn-Al tensile sample, having tensile axis at an angle of 45° to rolling direction, tested at a strain rate of $2 \times 10^{-4} s^{-1}$.
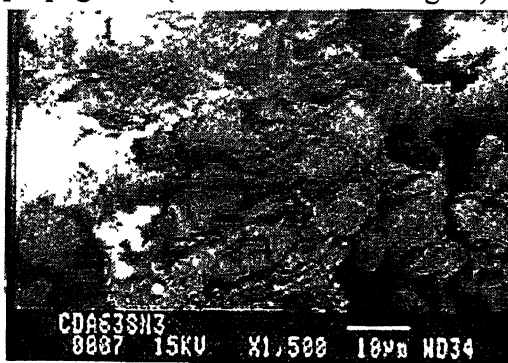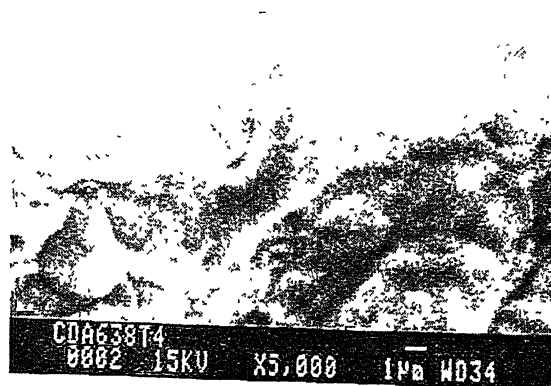

Fig 4.9b Fracture surface of the Cu-Zn-Al tensile sample, having tensile axis at an angle of 45° to rolling direction, tested at a strain rate of $2 \times 10^{-4} s^{-1}$.
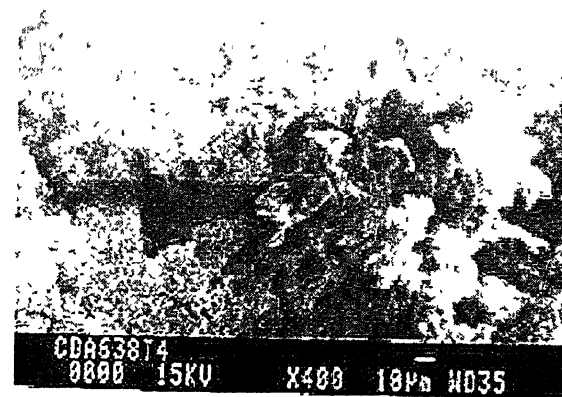
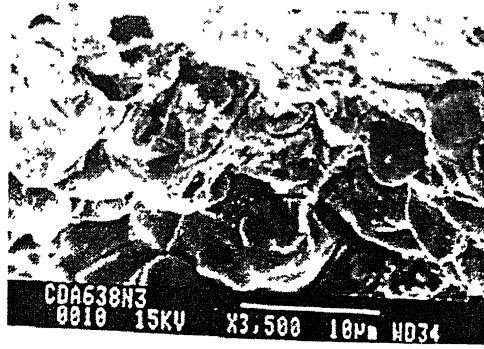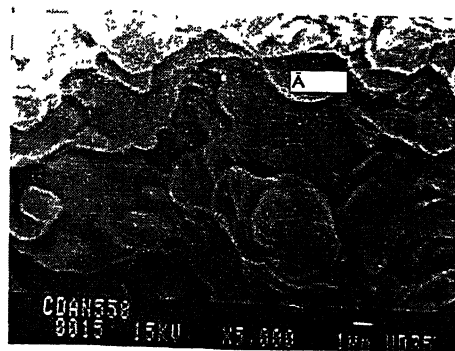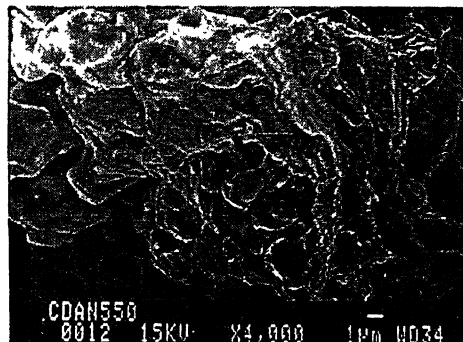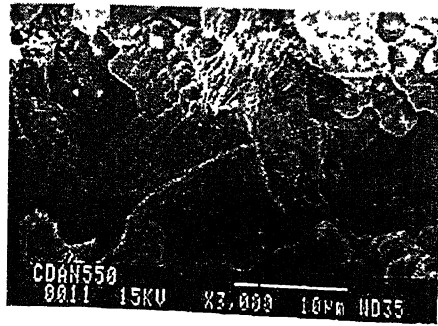
Fig 4.9c Fracture surface of the Cu-Zn-Al tensile sample, having tensile axis at an angle of 45° to rolling direction, tested at a strain rate of $2 \times 10^{-4} s^{-1}$.

4.3.2 Al-Mg Alloy

Tensile samples normal to rolling direction.

Figs. 4.10 and 4.11 show the fracture surface of the samples having tensile gauge length normal to the rolling direction. Like Cu-Zn-Al samples this material also shows dimpled fracture surface, which is a characteristic of ductile fracture. Figs. 4.10a and 4.10b show the fracture surfaces of the samples tested at the strain rate of 2×10^{-2} s^{-1}. Fig. 4.10a shows the relief of grain. Same features have been observed in case of Cu-Zn-Al alloys. Fig. 4.10b shows the evidence of intergranular mode of fracture. As the testing temperature is higher than $0.4 T_M$ the grain boundary being weaker than the grain, the crack initiates at the grain boundary leading to intergranular fracture.

Figs. 4.11a and 4.11b show the fracture surfaces of the samples tested at the strain rate of 2×10^{-4} s^{-1}. These micrographs also demonstrate the fact that ductile fracture takes place. Fig. 4.11a shows the dimpled fracture surface, which is a characteristic of ductile fracture. Fig. 4.11b shows evidence of cavity interlinkage.

Tensile samples parallel to rolling direction.

Figs. 4.12 and 4.13 show the fracture surfaces of the samples having tensile gauge length parallel to the rolling direction. Figs. 4.12a and 4.12b show the fracture surfaces of the samples tested at the strain rate of 2×10^{-2} s^{-1}. Like the normal samples these samples also undergo ductile fracture. Fig. 4.12a supports this fact by showing dimpled fracture surface. Fig. 4.12b shows the evidence of cavity interlinkage. This interlinkage of cavities reduces the load-bearing cross-section and results in failure.

Figs. 4.13a and 4.13b show the fracture surfaces of the samples tested at the strain rate of 2×10^{-4} s^{-1}. Fig. 4.13a shows that grain relief is taking place as a result of grain boundary sliding. The details of this feature have been discussed in the early part of this section. Fig. 4.13b shows the evidence of intergranular fracture.
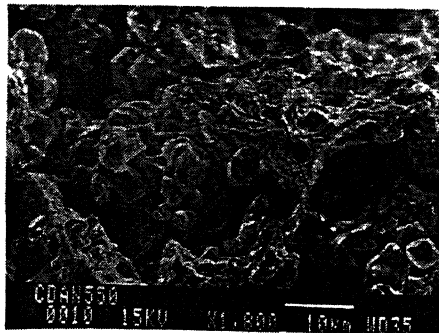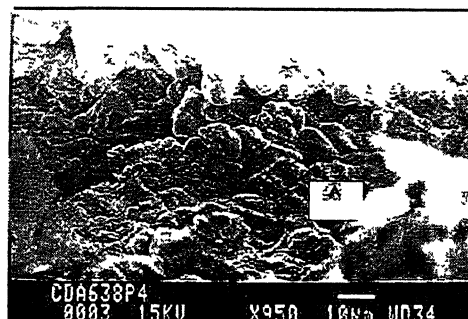
Fig. 4.11a Fracture surface of the Al-Mg tensile sample, having tensile axis normal to the rolling direction, tested at a strain rate of 2×10^{-4} s^{-1}.
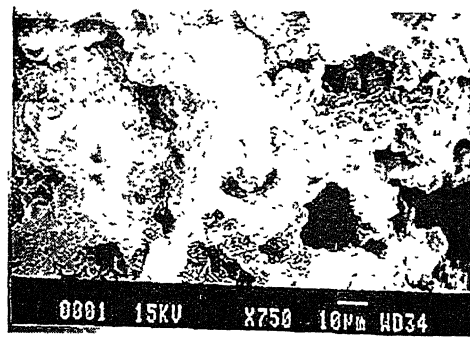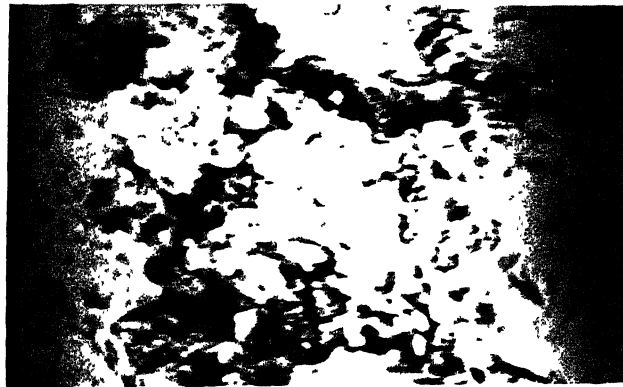

Fig. 4.11b Fracture surface of the Al-Mg tensile sample, having tensile axis normal to the rolling direction, tested at a strain rate of 2×10^{-4} s^{-1}. Fig. Shows the cavity interlinkage.
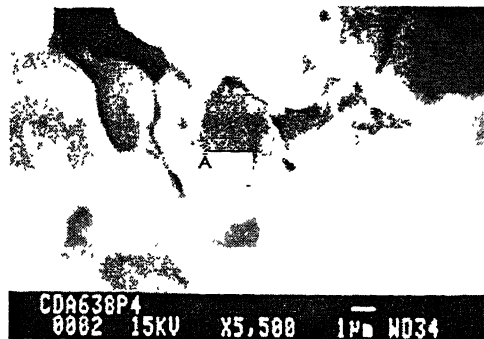
Fig. 4.12a Fracture surface of the Al-Mg tensile sample, having tensile axis parallel to the rolling direction, tested at a strain rate of $2 \times 10^{-2} \, s^{-1}$. Fig. shows the evidence of ductile fracture.
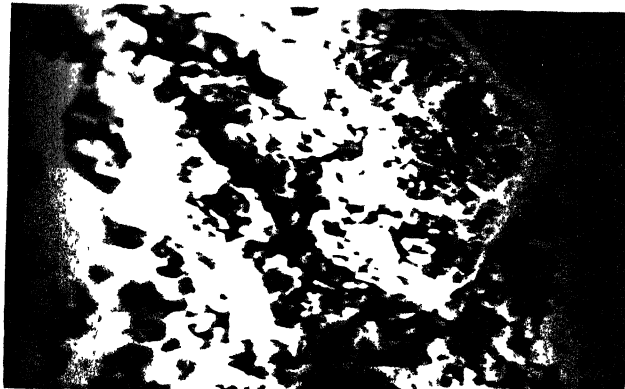
Fig. 4 12b Fracture surface of the Al-Mg tensile sample, having tensile axis parallel to the rolling direction, tested at a strain rate of $2 \times 10^{-2} \, s^{-1}$. Figs. show the evidence of interlinkage
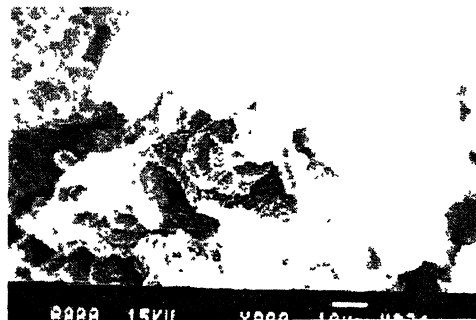
Fig. 4.13a Fracture surface of the Al-Mg tensile sample, having tensile axis parallel to the rolling direction, tested at a strain rate of $2 \times 10^{-4} \, s^{-1}$. Figs. shows the evidence of grain relief.
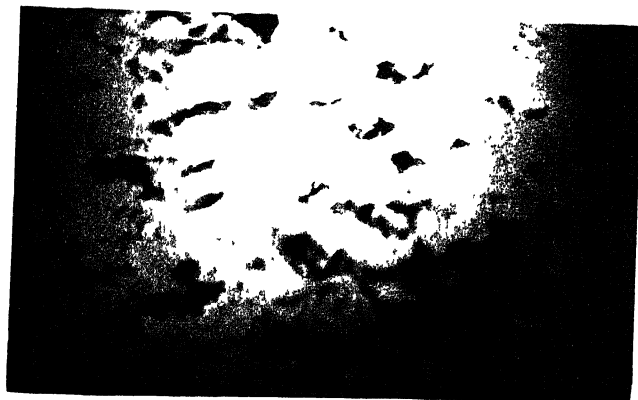
Fig. 4.13b Fracture surface of the Al-Mg tensile sample, having tensile axis parallel to the rolling direction, tested at a strain rate of $2 \times 10^{-4} \, s^{-1}$. Figs. show the evidence of intergranular fracture.

4.4 Optical Microscopy.

4.4.1 Cu-Zn-Al alloy

Tensile Samples normal to rolling direction

Figs. 4.14 and 4.15 are the micrographs of the gauge length of the samples normal to the rolling direction. Figs. 4.14a to 4.14d show the micrographs of the samples tested at a strain rate of $2 \times 10^{-2} s^{-1}$. The micrographs are arranged in order of increasing distance from fracture tip to grip (Fig. 4.14a is closest to the tip and Fig. 4.14d being furthest from the tip). Tensile axis is along the horizontal direction. It is observed that those cavities are elongated and interconnected along the direction perpendicular to the tensile axis. Fig. 4.14a shows the micrograph of the section at vicinity of fracture tip. This illustrates the extensive cavitation tendency near the fracture tip. This is due to the fact that near the fracture surface the instability is maximum. Here cavities get interconnected which in turn reduces the load bearing cross section and leads to fracture. The volume fraction of cavity reduces with increasing distance from fracture tip. This can be shown in Figs. 4.14b, 4.14c, and 4.14d. In Fig. 4.14c it is shown that the cavities are interconnected along the direction normal to the tensile axis, i.e., along the rolling direction. Fig 4.14d shows an optical micrograph near the grip section. It is observed that near the grip section the degree of cavitation is significantly lower. This is due to the fact that in the vicinity of the grip region the flow instability is much lower than that at the fracture tip region.

Figs. 4.15a to 4.15d show the micrographs of the samples tested at a strain rate of $2 \times 10^{-4} s^{-1}$. The micrographs are arranged in order of increasing distance from fracture tip to grip (Fig. 4.15a is closest to the tip and Fig. 4.15d being furthest from the tip). Tensile axis is along the horizontal direction. Here also the orientation of the cavities and cavity interconnection is similar to the higher strain rate case. The difference in the extent of

cavity interconnection is lesser than at the higher strain rate case. This difference is due to the fact that in case of lower strain rate diffusion controlled mechanism of cavity growth is expected to be prevalent. For this kind of mechanism the cavities have the tendency to be isolated. In lower strain rate deformation, the deformation rate is lower so mass transfer via diffusion can easily take place. For this reason cavities are having more regular shape. On the other hand in strain controlled growth mechanism the cavities are having irregular shape and the interconnectivity also is on the higher side. Details about cavity growth mechanism are referred in section 2.42.

Tensile samples parallel to tensile axis.

Figs. 4.16 and 4.17 are the micrographs of the gauge length of the samples parallel to the rolling direction. Figs. 4.16a to 4.16d show the micrographs of the samples tested at a strain rate of $2 \times 10^{-2} s^{-1}$. The micrographs are arranged in order of increasing distance from fracture tip to grip (Fig. 4.16a is closest to the tip and Fig. 4.16d being furthest from the tip). Tensile axis is along the horizontal direction. The cavity stringers are parallel to tensile axis. As in the case of normal sample, here also the degree of cavitation is much higher at the vicinity of fracture surface and significantly lower at the grip section. The underlying reasons for these phenomena are similar to the previous case.

Figs. 4.17a to 4.17d show the micrographs of the samples tested at a strain rate of $2 \times 10^{-4} s^{-1}$. Fig. 4.17c shows that the orientation of cavity stringers is parallel to tensile axis. But, in Fig 4.17a it is shown that the cavities are interconnected along the normal direction. However, this observation was only an exception to the general observation that cavity interconnection occurs along the rolling direction. Fig. 4.17b shows the evidence of filament forming. Due to the instability in flow the filament breaks down and cavities get interconnected. The load bearing cross section is reduced and sample undergoes failure. Thus, it can be concluded that in the region of the fracture tip the breaking down of filaments plays an important role in cavity interconnection. Fig. 4.17d

shows the cavity distribution near the grip region. It also illustrates the lower degree of cavitation near the grip region.

Tensile samples oriented at 45° angle to rolling direction

Figs. 4.18 and 4.19 are the micrographs of the gauge length of the samples oriented at 45° angle to rolling direction. Figs. 4.18a to 4.18d show the micrographs of the samples tested at a strain rate of $2\times10^{-2}s^{-1}$. The micrographs are arranged in order of increasing distance from fracture tip to grip (Fig. 4.18a is closest to the tip and Fig. 4.18d being furthest from the tip). Tensile axis is along the horizontal direction. The basic difference in cavitation behavior is that these samples are subjected to cavitation to a much lesser extent as compared to parallel and normal samples. This is due to the fact that the rolling direction may incorporate directionality in the slip system at the grain boundary, which in turn leads to a major role in accommodation mechanism like grain boundary folding and grain boundary migration. Another important observation is that in case of these samples no specific direction of cavity distribution, alignment and cavity interconnection has been observed. From this it can be interpreted that cavity stringers are not directed to the rolling direction in this case, whereas in the previous cases the cavity stringers are directed along the rolling axis.

Figs. 4.19a to 4.19d show the micrographs of the samples tested at a strain rate of $2\times10^{-4}s^{-1}$. The micrographs are arranged in order of increasing distance from fracture tip to grip (Fig. 4.19a is closest to the tip and Fig. 4.19d being furthest from the tip). Tensile axis is along the horizontal direction. The characteristics are more or less same as in the case of higher strain rate. The only difference being, the cavities are more spherical in case of lower strain rate. Fig. 4.19c represents this morphology and shape of cavities. The cavities here have regular and near spherical shapes. This can be attributed by the mechanism of cavity growth, which has been discussed in the previous part of this section.
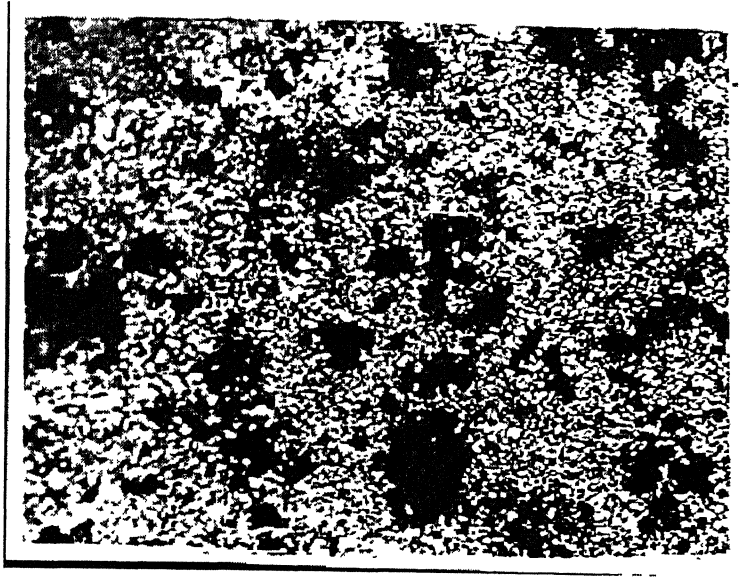
Fig 4.14a   Optical micrograph of the Cu-Zn-Al sample normal to the rolling direction tested at a strain rate of $2 \times 10^{-2} s^{-1}$. Magnification 100×. The micrograph is showing extensive cavitation near the fracture tip.

Fig 4.14b Optical micrograph of the Cu-Zn-Al sample normal to the rolling direction tested at a strain rate of $2 \times 10^{-2} s^{-1}$. Magnification 100×. The cavities are distributed and interconnected along the rolling direction. Tensile axis is along the horizontal direction.
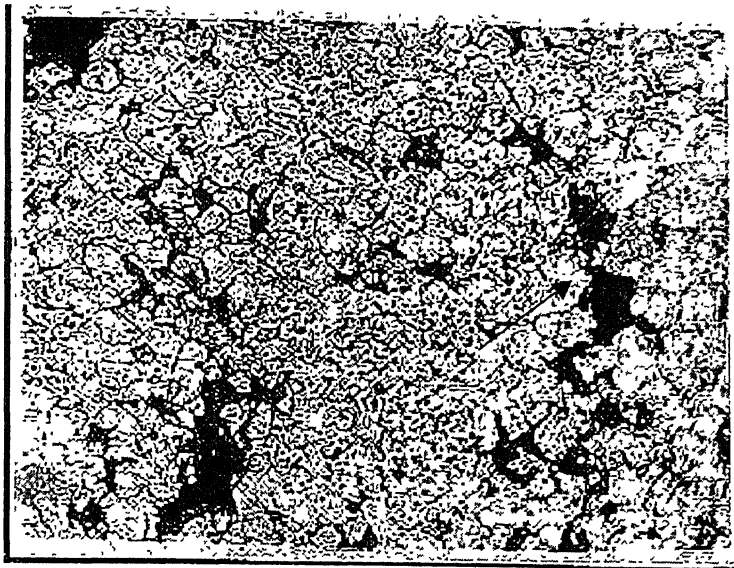
Fig 4.14c   Optical micrograph of the Cu-Zn-Al sample normal to the rolling direction tested at a strain rate of $2\times10^{-2}s^{-1}$. Magnification 500×. The cavities are distributed and interconnected along the rolling direction (shown by the arrow mark). Tensile axis is along the horizontal direction.
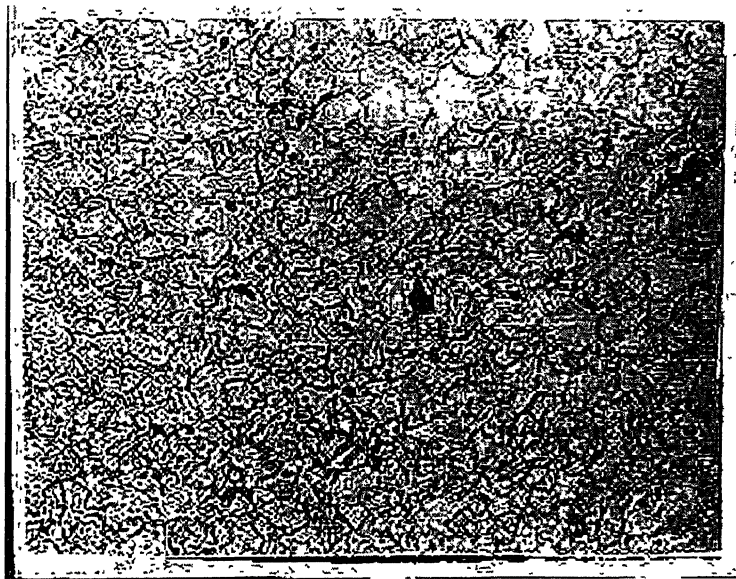
Fig 4.14d   Optical micrograph of the Cu-Zn-Al sample normal to the rolling direction tested at a strain rate of $2\times10^{-2}s^{-1}$. Magnification 500×. Figure shows the lesser amount of cavitation near the grip region. Tensile axis is along the horizontal direction.
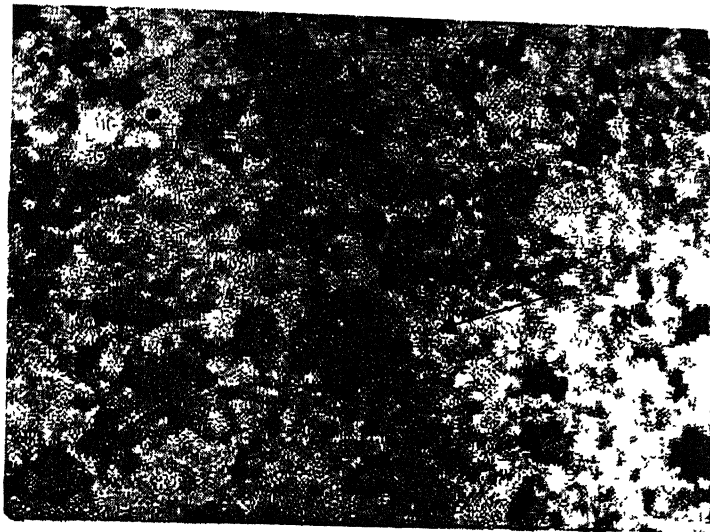
Fig 4.15a   Optical micrograph of the Cu-Zn-Al sample normal to the rolling direction tested at a strain rate of $2\times10^{-4}s^{-1}$. Magnification 100×. Figure shows extensive cavitation in the vicinity of fracture tip (shown by the arrow mark). Tensile axis is along the horizontal direction.
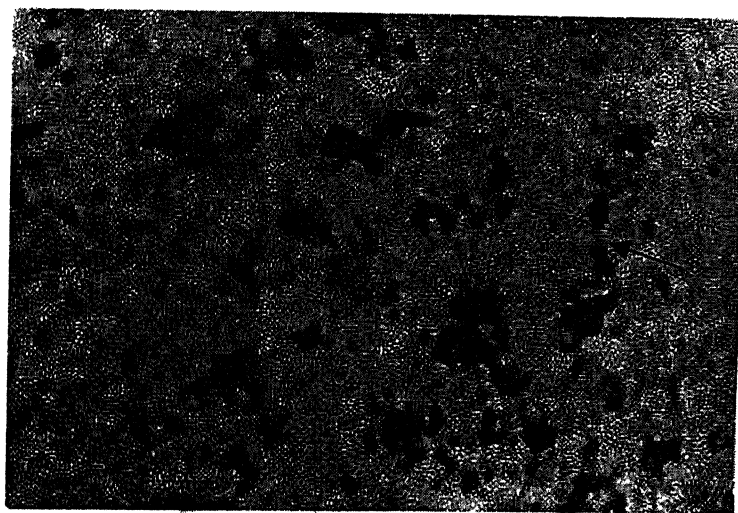
Fig 4.15b   Optical micrograph of the Cu-Zn-Al sample normal to the rolling direction tested at a strain rate of $2\times10^{-4}s^{-1}$. Magnification 100×. Figure shows the alignment of the cavities along the rolling direction (shown by the arrow mark). The degree of cavitation is lesser than that of the higher strain rate case. Tensile axis is along the horizontal direction.

68
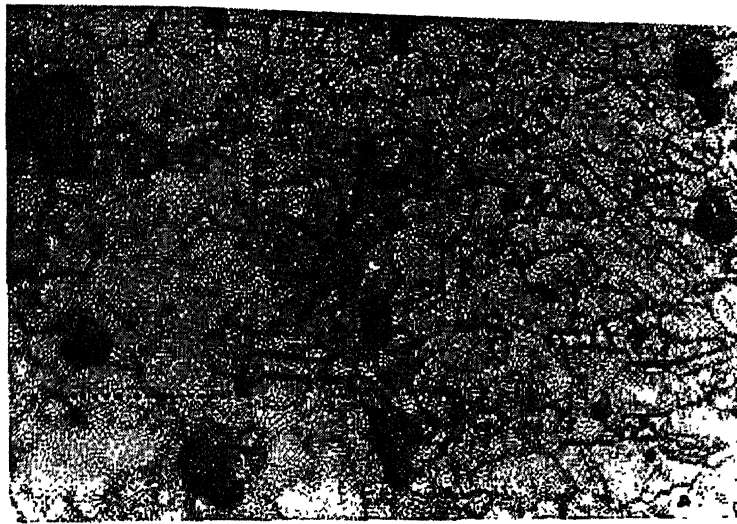
Fig 4.15c   Optical micrograph of the Cu-Zn-Al sample normal to the rolling direction tested at strain rate of $2\times10^{-4}s^{-1}$. Magnification 1000×. Figure shows lesser interconnection of cavities. Tensile axis is along the horizontal direction.
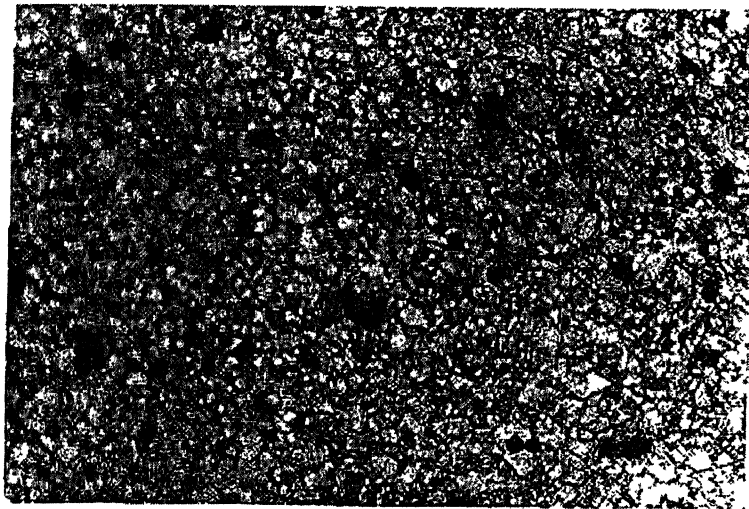
Fig 4.15d   Optical micrograph of the Cu-Zn-Al sample normal to the rolling direction tested at a strain rate of $2\times10^{-4}s^{-1}$. Magnification 200×. Figure shows the lesser degree of cavitation in the grip region. Tensile axis is along the horizontal direction.

Fig 4.16a   Optical micrograph of the Cu-Zn-Al sample parallel to the rolling direction tested at a strain rate of $2 \times 10^{-2} s^{-1}$. Magnification 100×. Figure shows extensive cavitation near the fracture tip region. Tensile axis is along the horizontal direction.

Fig 4.16b   Optical micrograph of the Cu-Zn-Al sample parallel to the rolling direction tested at a strain rate of $2 \times 10^{-2} s^{-1}$. Magnification 100×. Cavity stringers are parallel to the tensile axis (shown by the arrow mark). Tensile axis is along the horizontal direction.

Fig 4.16c   Optical micrograph of the Cu-Zn-Al sample parallel to the rolling direction tested at a strain rate of $2 \times 10^{-2} s^{-1}$.Magnification 200×. Tensile axis is along the horizontal direction.

Fig 4.16d   Optical micrograph of the Cu-Zn-Al sample parallel to the rolling direction tested at a strain rate of $2 \times 10^{-2} s^{-1}$. Magnification 500×. Tensile axis is along the horizontal direction. Figure shows the lesser degree of cavitation near the grip region.

Fig 4.17a   Optical micrograph of the Cu-Zn-Al sample parallel to the rolling direction tested at a strain rate of $2\times10^{-4}s^{-1}$. Magnification 200×. Tensile axis is along the horizontal direction. The alignment and direction of interconnection are not parallel to the tensile axis. (shown by the arrow mark)

Fig 4.17b   Optical micrograph of the Cu-Zn-Al sample parallel to the rolling direction tested at a strain rate of $2\times10^{-4}s^{-1}$. Magnification 500×. Tensile axis is along the horizontal direction. Figure shows a filament formed by deformation, breaking down of which produces interconnection of cavities.

Fig 4.17c   Optical micrograph of the Cu-Zn-Al sample parallel to the rolling direction tested at $2 \times 10^{-4} s^{-1}$. Magnification 200×. Tensile axis is along the horizontal direction. Arrow marks in the figure shows that the cavity stringers are parallel to the tensile axis.

Fig 4.17d   Optical micrograph of the Cu-Zn-Al sample parallel to the rolling direction tested at a strain rate of $2 \times 10^{-4} s^{-1}$. Magnification 100×. Tensile axis is along the horizontal direction. Figure shows the lesser degree of cavitation near the grip region.

73
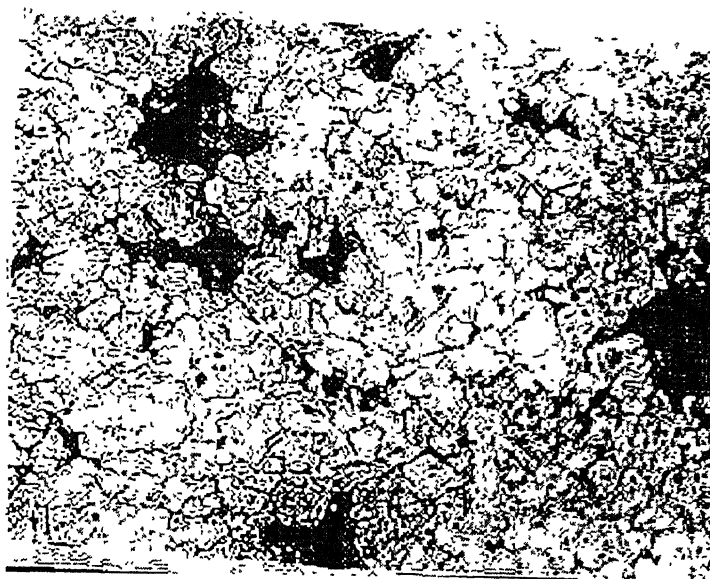
Fig 4.18a   Optical micrograph of the Cu-Zn-Al tensile sample having tensile axis at an angle of 45° to rolling direction, tested at a strain rate of $2 \times 10^{-2} s^{-1}$. Magnification 500×. Figure shows cavitation near the fracture tip region. The degree of cavitation is lesser than that of parallel and normal sample.
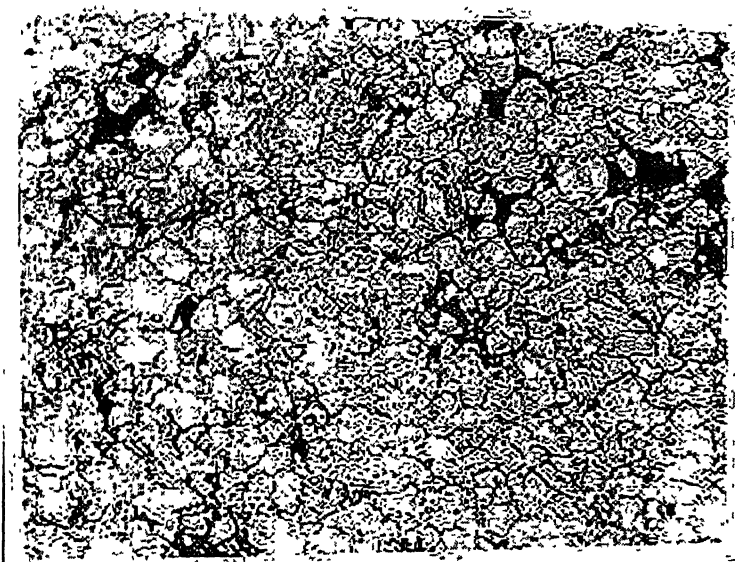
Fig 4.18b Optical micrograph of the Cu-Zn-Al tensile sample having tensile axis at an angle of 45° to rolling direction, tested at a strain rate of $2 \times 10^{-2} s^{-1}$. Tensile axis is along the horizontal direction. Magnification 500×. Figure shows intergranular nature of crack propagation (shown by the arrow mark).
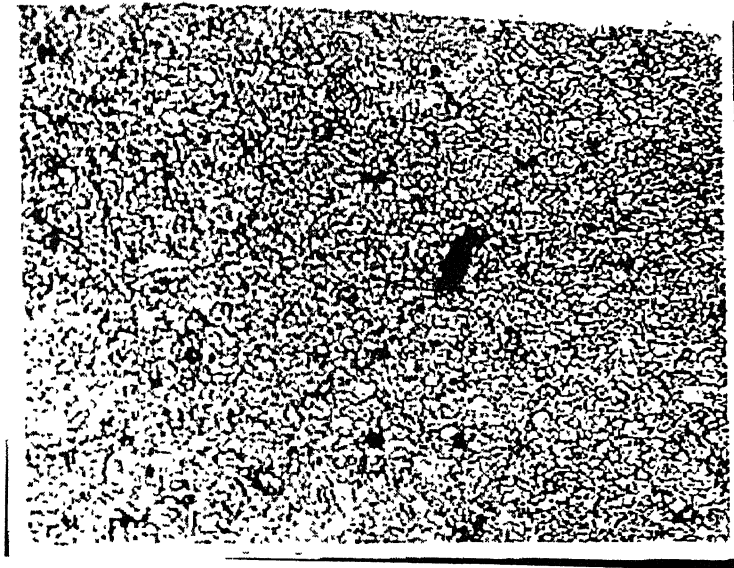
Fig 4.18c   Optical micrograph of the Cu-Zn-Al tensile sample having tensile axis at an angle of 45° to rolling direction, tested at a strain rate of $2\times10^{-2}s^{-1}$. Tensile axis is along the horizontal direction. Magnification 100×. Figure shows the cavitation near the grip region.
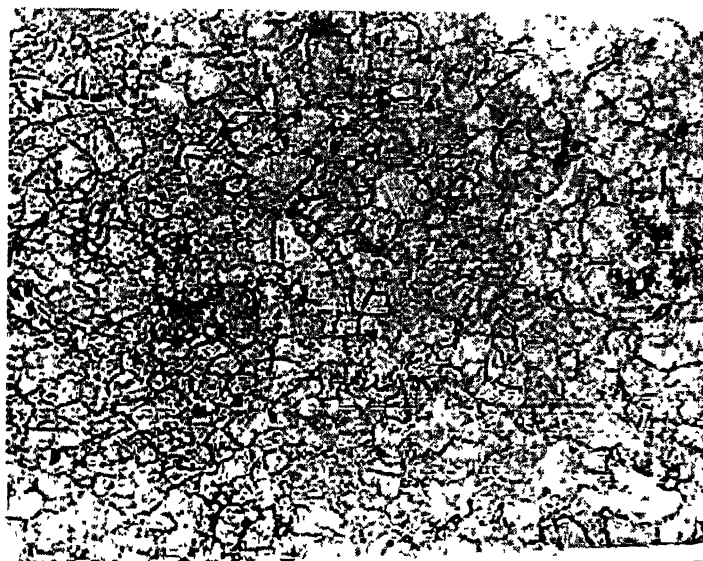
Fig 4.18d   Optical micrograph of the Cu-Zn-Al tensile sample having tensile axis at an angle of 45° to rolling direction, tested at a strain rate of $2\times10^{-2}s^{-1}$. Tensile axis is along the horizontal direction. Magnification 500×. Figure shows the cavitation near the grip region.
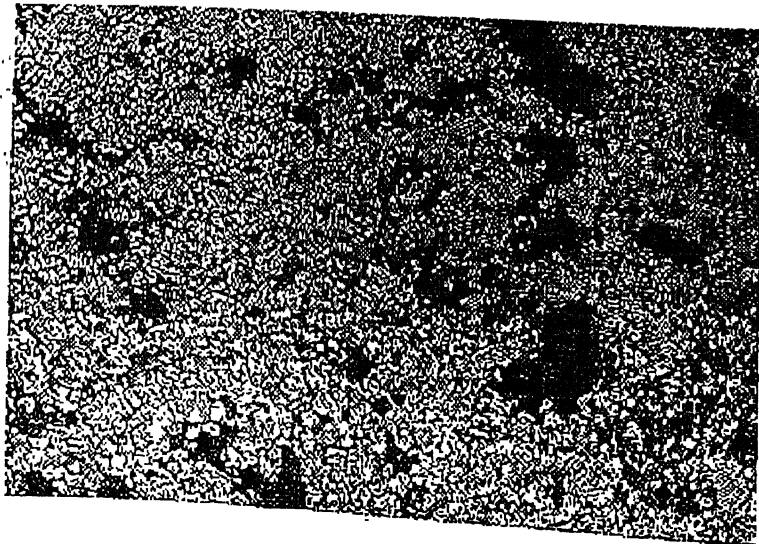
Fig 4.19a Optical micrograph of the Cu-Zn-Al tensile sample having tensile axis at an angle of 45° to rolling direction, tested at a strain rate of $2\times10^{-4}s^{-1}$. Magnification 200×. Tensile axis is along the horizontal direction. Figure shows cavitation near the fracture tip region.
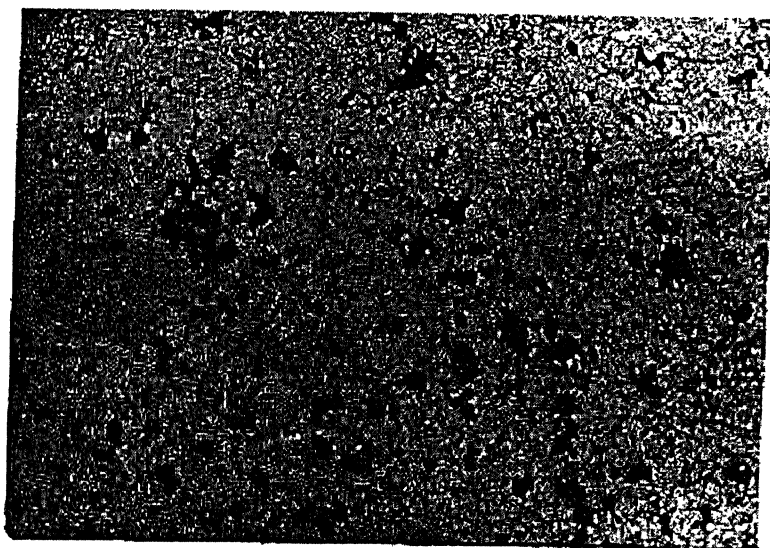
Fig 4.19b Optical micrograph of the Cu-Zn-Al tensile sample having tensile axis at an angle of 45° to rolling direction, tested at a strain rate of $2\times10^{-4}s^{-1}$. Magnification 200×. Tensile axis is along the horizontal direction

Fig 4.19c Optical micrograph of the Cu-Zn-Al tensile sample having tensile axis at an angle of 45° to rolling direction, tested at a strain rate of $2 \times 10^{-4} s^{-1}$. Magnification 500×. Tensile axis is along the horizontal direction. Figure shows spherical cavities.
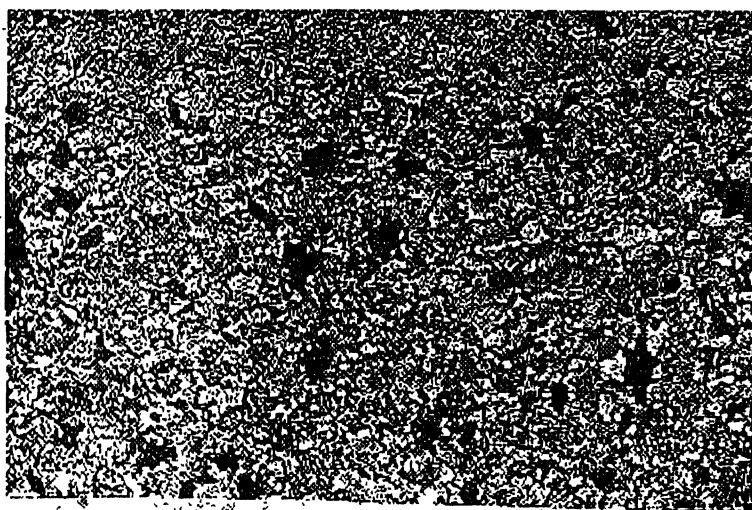
Fig 4.19d Optical micrograph of the Cu-Zn-Al tensile sample having tensile axis at an angle of 45° to rolling direction, tested at a strain rate of $2 \times 10^{-4} s^{-1}$. Magnification 200×. Tensile axis is along the horizontal direction. Figure shows the degree of cavitation near the grip region.

4.4.2 Al-Mg alloy

Tensile Samples normal to rolling direction

Figs. 4.20 and 4.21 are the micrographs of the gauge length of the samples normal to the rolling direction. Figs. 4.20a to 4.20c show the micrographs of the samples tested at a strain rate of $2 \times 10^{-2} s^{-1}$. The micrographs are arranged in order of increasing distance from fracture tip to grip (Fig. 4.20a is closest to the tip and Fig. 4.20c being furthest from the tip). Tensile axis is along the horizontal direction. The basic features are same as of the Cu-Zn-Al materials. Fig. 4.20a shows the extensive cavitation near the fracture tip. That is due to instability in flow followed by interlinkage of cavities. Fig 4.20b shows that the cavities are distributed along the normal direction to the tensile axis. Fig. 4.20c shows the degree of cavitation near the grip region. In that region the extent of cavitation is much lower.

Figs. 4.21a to 4.21c show the micrographs of the samples tested at a strain rate of $2 \times 10^{-4} s^{-1}$. The micrographs are arranged in order of increasing distance from fracture tip to grip (Fig. 4.21a is closest to the tip and Fig. 4.21c being furthest from the tip). Tensile axis is along the horizontal direction. Here also the orientation of the cavities and cavity interconnection is similar to the higher strain rate case. The difference in the extent of cavity interconnection is lesser than at the higher strain rate case. The reason for this phenomenon has been discussed in the early part of this section.

Tensile samples parallel to tensile axis.

Figs. 4.22 and 4.23 are the micrographs of the gauge length of the samples parallel to the rolling direction. Figs. 4.22a to 4.22c show the micrographs of the samples tested at a strain rate of $2 \times 10^{-2} s^{-1}$. The micrographs are arranged in order of increasing distance from fracture tip to grip (Fig. 4.22aa is closest to the tip and Fig. 4.22c being furthest from the tip). Tensile axis is along the horizontal direction. The cavity stringers are parallel to tensile axis. As in the case of normal sample here also the degree of cavitation is much higher at the vicinity of fracture surface and significantly lower at the grip section. The underlying reasons for these phenomena are similar like to previous cases.

Figs. 4.23a to 4.23c show the micrographs of the samples tested at a strain rate of $2 \times 10^{-4} s^{-1}$. Fig. 4.23a shows extensive cavitation near the fracture tip. Fig. 4.23c shows the extent of cavitation near the grip region. Due to stability in flow the extent of cavitation is much lower and cavities are also isolated.
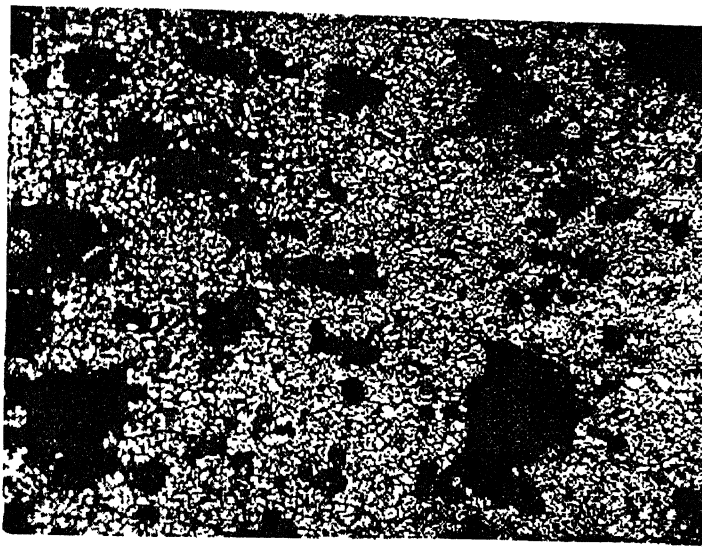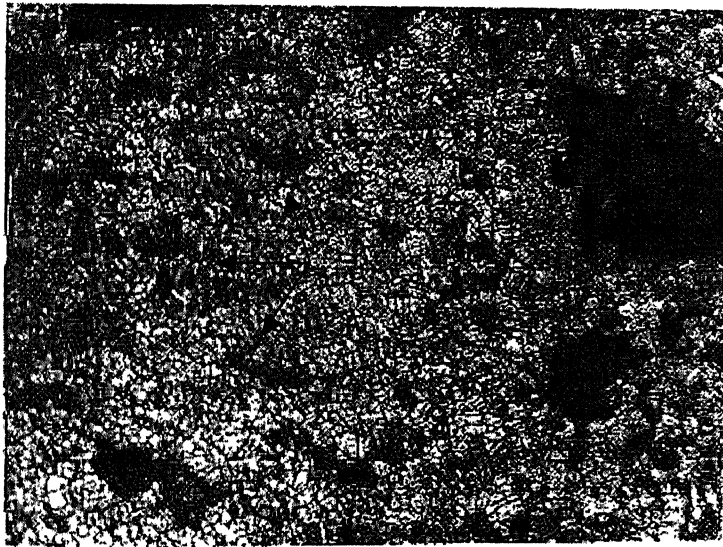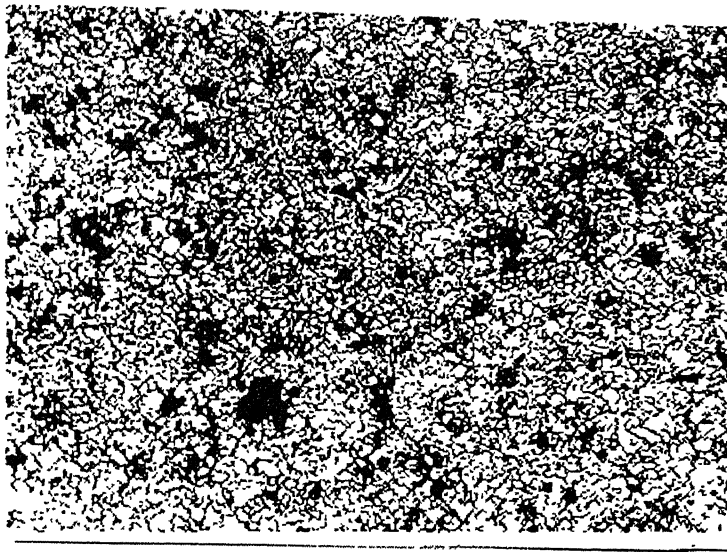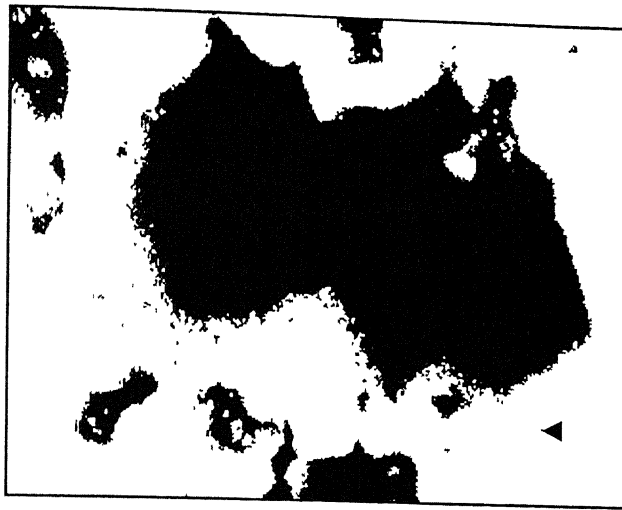
Fig. 4.20a   Optical micrograph of the Al-Mg sample normal to the rolling direction tested at a strain rate of $2 \times 10^{-2} s^{-1}$. Magnification 500×. The micrograph is showing extensive cavitation near the fracture tip.
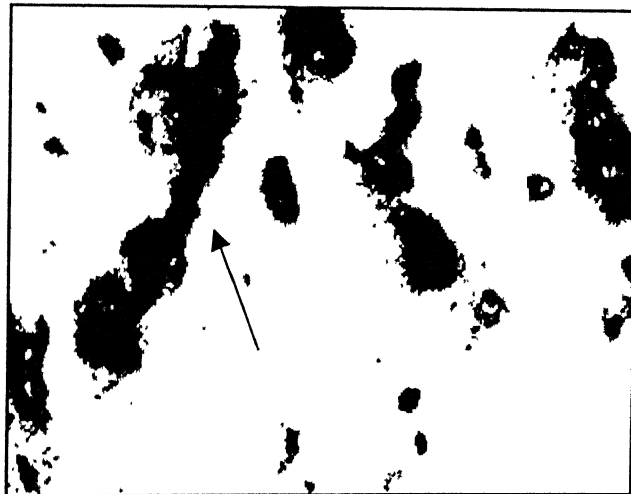
Fig. 4.20b Optical micrograph of the Al-Mg sample normal to the rolling direction tested at a strain rate of $2 \times 10^{-2} s^{-1}$. Magnification 200×. The cavities are distributed and interconnected along the rolling direction (see arrow). Tensile axis is along the horizontal direction

80
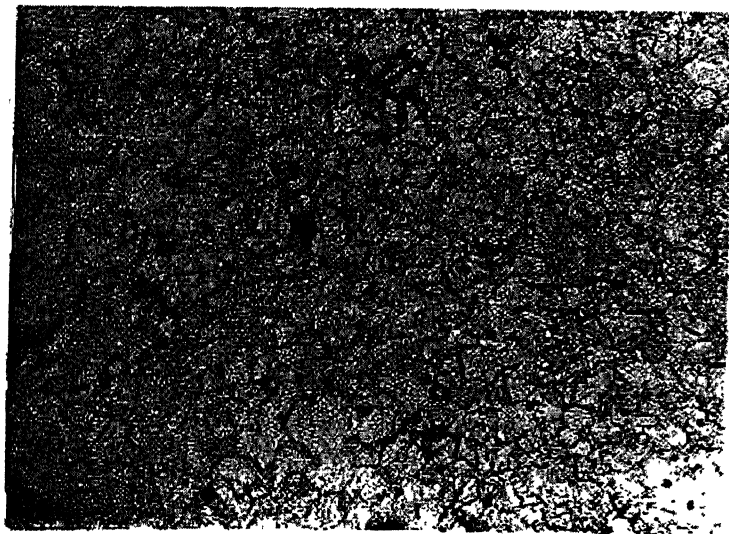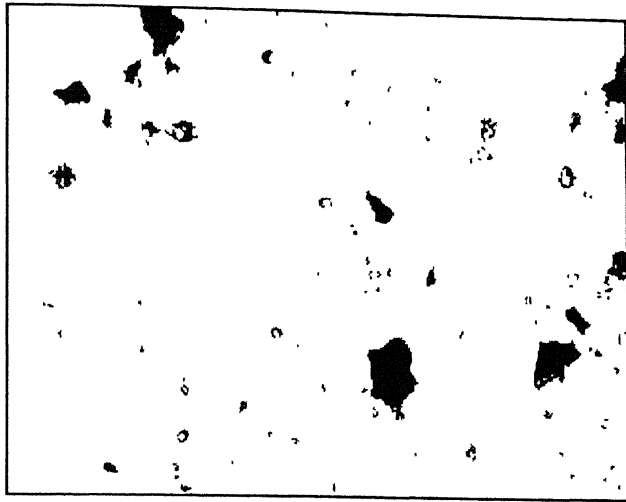
Fig. 4.20c Optical micrograph of the Al-Mg sample normal to the rolling direction tested at a strain rate of $2 \times 10^{-2} s^{-1}$. Magnification 200×. Figure shows the lesser degree of cavitation in the grip region. Tensile axis is along the horizontal direction.
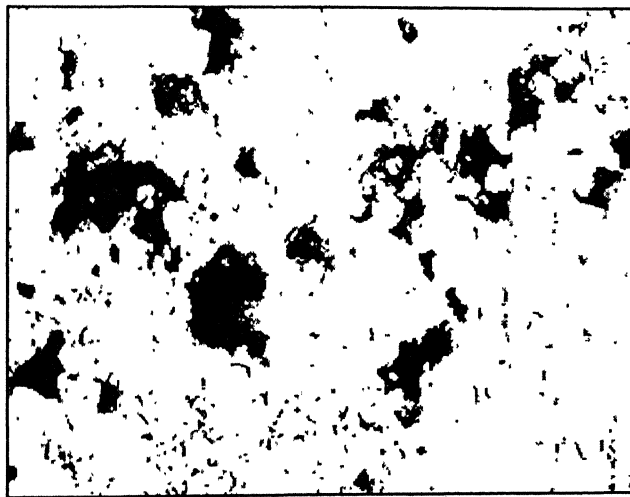
Fig. 4.21a Optical micrograph of the Al-Mg sample normal to the rolling direction tested at a strain rate of $2 \times 10^{-4} s^{-1}$. Magnification 200×. The micrograph is showing extensive cavitation near the fracture tip.
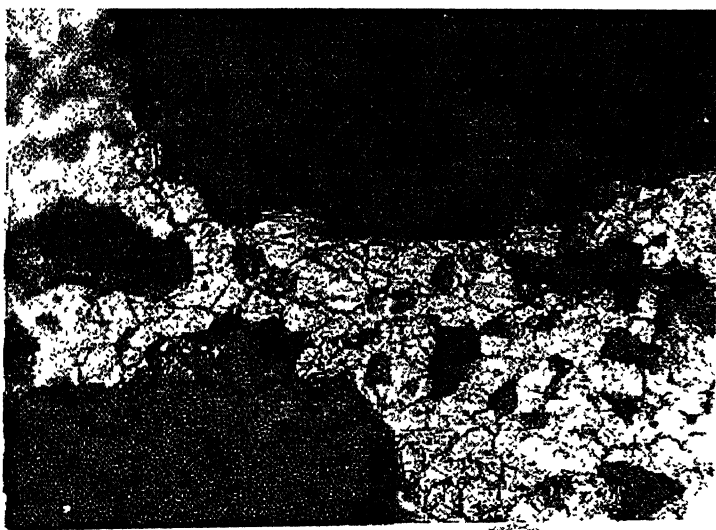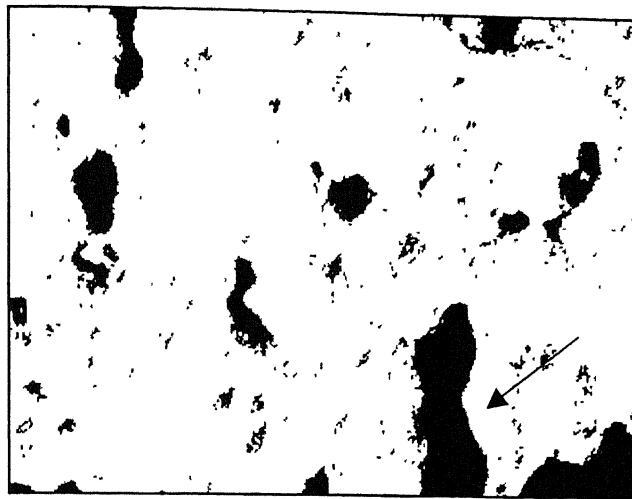
Fig. 4.21b Optical micrograph of the Al-Mg sample normal to the rolling direction tested at a strain rate of $2\times10^{-4}s^{-1}$. Magnification 200×. The cavities are distributed and interconnected along the rolling direction (see arrow). Tensile axis is along the horizontal direction
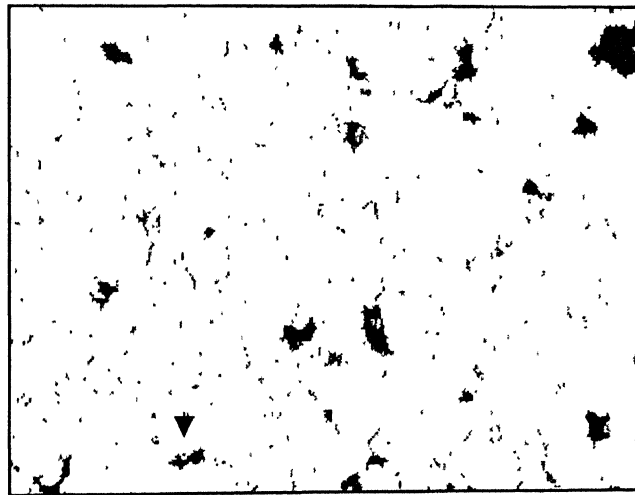
Fig. 4.21c Optical micrograph of the Al-Mg sample normal to the rolling direction tested at a strain rate of $2\times10^{-4}s^{-1}$. Magnification 200×. Figure shows the lesser degree of cavitation in the grip region. Tensile axis is along the horizontal direction.
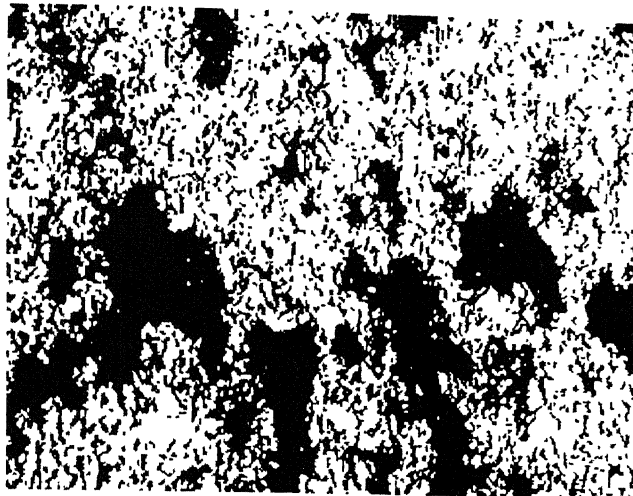
Fig. 4.22a   Optical micrograph of the Al-Mg sample parallel to the rolling direction tested at a strain rate of $2 \times 10^{-2} s^{-1}$. Magnification 500×. The micrograph is showing extensive cavitation near the fracture tip.

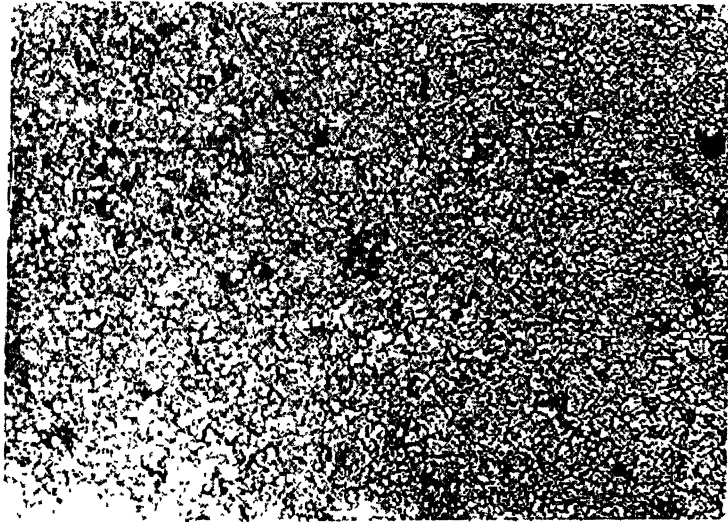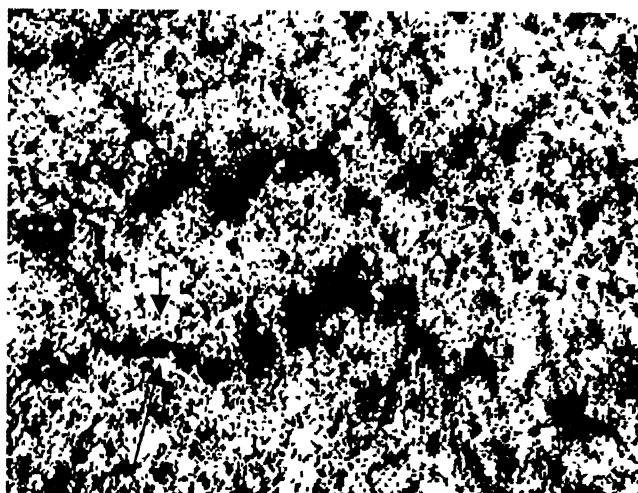

Fig. 4.22b Optical micrograph of the Al-Mg sample parallel to the rolling direction tested at a strain rate of $2 \times 10^{-2} s^{-1}$. Magnification 200×. The cavities are distributed and interconnected along the rolling direction (see arrow). Tensile axis is along the horizontal direction
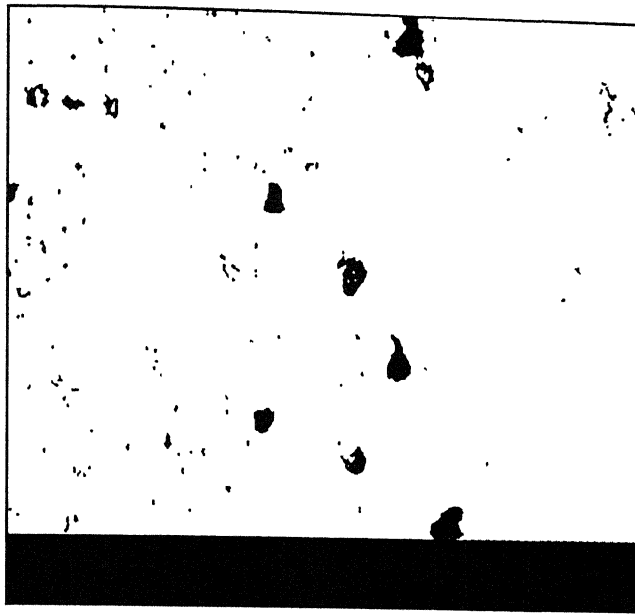
Fig. 4.22c Optical micrograph of the Al-Mg sample parallel to the rolling direction tested at a strain rate of $2 \times 10^{-4} s^{-1}$. Magnification 200×. Figure shows the lesser degree of cavitation near the grip region. Tensile axis is along the horizontal direction.
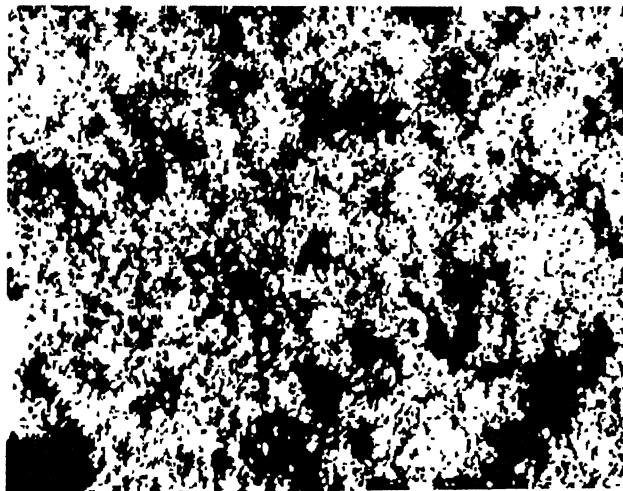
Fig. 4.23a   Optical micrograph of the Al-Mg sample parallel to the rolling direction tested at a strain rate of $2 \times 10^{-4} s^{-1}$. Magnification 200×. The micrograph is showing extensive cavitation near the fracture tip.
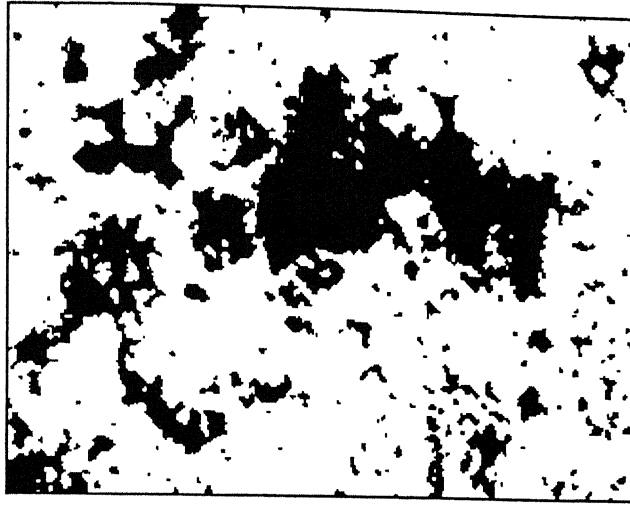
Fig. 4.23b Optical micrograph of the Al-Mg sample parallel to the rolling direction tested at a strain rate of $2 \times 10^{-2} s^{-1}$. Magnification 200×. The cavities are distributed and interconnected along the rolling direction. Tensile axis is along the horizontal direction.

Fig. 4.23c Optical micrograph of the Al-Mg sample parallel to the rolling direction tested at a strain rate of $2 \times 10^{-4} s^{-1}$. Magnification 200×. Figure shows lesser degree of cavitation near the grip region. Tensile axis is along the horizontal direction.

4.5 Stereological measurements

4.5.1 Cu-Zn-Al Alloy

4.5.1.1 Cavity Volume Fraction

Tables 4.3 to 4.9 show the cavity volume fraction of the tested Cu-Al samples. Data are tabulated along the gauge length and starting from fracture surface to grip. Each value represents mean of cavity volume fraction measured from four different fields of view. The scatter of values about the mean is small, as can be noted from the raw data in tables A1.1 to A1.6. For each sample regardless of the rolling direction and strain rate the cavity volume fraction is higher near the fracture tip and gradually reduces near the grip portion. In superplastic deformation elongation occurs due to grain boundary sliding and not due to grain elongation while cavitation occurs due to lack of accommodation of grain boundary sliding. Thus, it may be concluded that the cause of failure is extensive cavitation followed by interconnection. The cavities are interconnected and reduce the load bearing cross-section area, which leads to fracture.

For the samples having the same orientation with rolling direction but tested under different strain rates do not show any significant variation in degree of cavitation but at lower strain rate i.e. at 2×10^{-4} s^{-1} it experiences lower degree of cavitation than higher strain rate. This could be accounted by nucleation and growth mechanism of cavitation.

It is found in the results that the degree of cavitation in the samples having 45° angle with rolling direction is significantly lower. It could be due to the different accommodation mechanisms such, grain boundary grain boundary folding and grain boundary migration. For grain boundary deformation to occur without producing cracks or cavities at the grain boundaries, deformation mechanisms, such as, grain boundary folding and grain

boundary migration, must be available to achieve continuity of strain along the grain boundary. However, no conclusive evidence for these mechanisms could be obtained in the present investigation,

Figs 4.24a to 4.24f show the variation of cavity volume fraction with width strain (width strain is calculated by measuring the fractional change in the gauge width from the fracture tip to grip of the tensile sample). For each sample the volume fraction of cavity increases with the width strain. From this behavior it can be concluded that due to instability in flow necking is occurred and cavities are also get interconnected intensely near the fracture tip.

Table 4.3 Cavity volume fraction of Cu-Zn-Al samples, having tensile axis at an angle of 45^0 to rolling direction, tested at a strain rate of 2×10^{-2} s^{-1}

No.	Mean Cavity Volume Fraction	No.	Mean Cavity Volume Fraction
1[*]	10.79%	8	4.49%
2	7.45%	9	1.52%
3	7.57%	10	1.23%
4	7.52%	11	1.07%
5	6.37%	12	0.87%
6	5.38%	13	0.49%
7	4.69%	14[**]	0.85%

*Closest to Fracture Tip
** Furthest from Fracture Tip

Table 4.4 Cavity Volume Fraction Of Cu-Zn-Al Samples Normal To Rolling Direction, Tested At a Strain Rate of $2 \times 10^{-2}\,\mathrm{s}^{-1}$.

No.	Mean Cavity Volume Fraction	No.	Mean Cavity Volume Fraction
1*	33.42%	20	11.81%
2	38.64%	21	9.14%
3	25.32%	22	9.54%
4	21.17%	23	7.40%
5	23.07%	24	7.07%
6	25.36%	25	6.34%
7	20.39%	26	6.95%
8	18.82%	27	4.96%
9	17.68%	28	4.43%
10	17.20%	29	4.23%
11	17.22%	30	3.88%
12	14.90%	31	3.70%
13	14.88%	32	4.46%
14	14.16%	33	4.59%
15	14.17%	34	4.53%
16	12.13%	35	2.44%
17	11.80%	36	2.44%
18	10.32%	37**	2.37%

*Closest to Fracture Tip
** Furthest from Fracture Tip

Table 4.5 Cavity Volume Fraction Of Cu-Zn-Al Samples Parallel To Rolling Direction Tested At a Strain Rate of $2 \times 10^{-2} s^{-1}$

No.	Mean Cavity Volume Fraction	No.	Mean Cavity Volume Fraction
1[*]	23.38%	12	9.06%
2	22.32%	13	9.69%
3	22.78%	14	8.26%
4	21.10%	15	8.37%
5	20.70%	16	8.50%
6	26.355	17	6.01%
7	18.63%	18	6.77%
8	18.54%	19	5.43%
9	16.64%	20	2.55%
10	12.62%	21	1.37%
11	10.22%	22[**]	1.66%

*Closest to Fracture Tip
** Furthest from Fracture Tip

Table 4.6 Cavity Volume Fraction Of Cu-Zn-Al Samples Parallel To Rolling Direction Tested At 2×10^{-4} s^{-1}

No.	Mean Cavity Volume Fraction	No.	Mean Cavity Volume Fraction
1*	30.01%	19	11.37%
2	31.28%	20	9.03%
3	24.57%	21	8.48%
4	22.46%	22	6.68%
5	23.78%	23	7.30%
6	16.68%	24	6.97%
7	20.05%	25	5.98%
8	19.58%	26	5.00%
9	20.92%	27	3.71%
10	19.58%	28	4.37%
11	20.92%	29	2.85%
12	16.50%	30	2.06%
13	13.90%	31	1.93%
14	13.14%	32	1.39%
15	12.52%	33	1.04%
16	15.52%	34	0.98%
17	15.00%	35	0.57%
18	13.44%	36**	0.23%

*Closest to Fracture Tip
** Furthest from Fracture Tip

Table 4.7 Cavity Volume Fraction Of Cu-Zn-Al Samples Normal To Rolling Direction Tested At $2 \times 10^{-4} s^{-1}$

No.	Mean Cavity Volume Fraction	No.	Mean Cavity Volume Fraction
1*	33.155	19	12.61%
2	32.08%	20	8.20%
3	43.05%	21	9.05%
4	26.95%	22	6.72%
5	30.02%	23	5.63%
6	22.38%	24	7.47%
7	22.47%	25	4.62%
8	19.39%	26	3.49%
9	17.38%	27	3.32%
10	21.27%	28	2.14%
11	15.18%	29	2.14%
12	16.06%	30	2.12%
13	15.93%	31	1.30%
14	16.33%	32	1.39%
15	13.50%	33	0.89%
16	17.41%	34	0.80%
17	17.41%	35**	0.60%

*Closest to Fracture Tip
** Furthest from Fracture Tip

Table 4.8 Cavity Volume Fraction Of Samples Having 45° Angel With Rolling Direction Tested At 2×10^{-4} s $^{-1}$

No.	Mean Cavity Volume Fraction	No.	Mean Cavity Volume Fraction
1*	18 66%	19	7 32%
2	20 74%	20	6 79%
3	16 41%	21	4 24%
4	16 09%	22	5 43%
5	12 77%	23	3 40%
6	10 77%	24	2 72%
7	11 63%	25	2 33%
8	10 84%	26	2 86%
9	8 21%	27	3.20%
10	7 60%	28	2 08%
11	7 50%	29	1 63%
12	8 45%	30	1 41%
13	7 15%	31	1 31%
14	7 59%	32	1 11%
15	6 29%	33	0.86%
16	6 94%	34	0.64%
17	6 58%	35	1 00%
18	7 33%	36**	00 37%

*Closest to Fracture Tip
** Furthest from Fracture Tip

4.5.1.2 Aspect Ratio Analysis

From the aspect ratio data it is found that aspect ratio is varying with strain rate. (see table 4.9 to 4.14) Regardless of rolling direction the aspect ratio is closer to unity in case of lower strain rate than in higher strain rate. So it can be said that the cavities are more spherical in lower strain rate deformation than in higher strain rate. This observation strongly suggests that diffusion controlled growth mechanism is dominant in the case of lower strain rate deformation. On the other hand the results of higher strain rate deformation elucidate the fact that strain induced growth mechanism is prevalent. Figs. 4.24a to 4.24f show the variation of aspect ratio with width strain. No definitive trends could be noticed from these plots.

Table 4.9 Aspect Ratio of Cu-Zn-Al Samples Parallel To Rolling Direction Tested At $2\times10^{-2}\,s^{-1}$

NO.	Aspect Ratio	NO.	Aspect Ratio
1[*]	1.78	11	1.97
2	1.75	12	1.86
3	1.72	13	1.76
4	1.68	14	1.63·
5	1.62	15	1.6
6	1.74	16	1.55
7	1.68	17	1.75
8	1.78	18	1.87
9	1.8	19	1.6
10	2.44	20[**]	1.75

Table 4.10 Aspect Ratio of Cu-Zn-Al Samples Normal To Rolling Direction Tested At $2\times10^{-2}\,s^{-1}$

No.	Aspect Ratio	No.	Aspect Ratio
1[*]	1.94	16	1.76
2	2.20	17	1.98
3	2.39	18	1.93
4	1.84	19	2.06
5	1.92	20	1.66
6	1.8	21	1.79
7	1.83	22	1.90
8	2.11	23	1.71
9	1.67	24	1.66
10	2.24	25	1.87
11	1.87	26	1.61
12	2.271	27	1.61
13	1.95	28	1.5
14	2.06	29	1.7
15	1.91	30	1.8
31	1.77	33	1.5
32	164	34[**]	1.73

*Closest to Fracture Tip
** Furthest from Fracture Tip

Table 4.11 Aspect Ratio of Cu-Zn-Al Samples Having 45° Angel To Rolling Direction Tested At 2×10^{-2} s $^{-1}$

No.	Aspect Ratio	No.	Aspect Ratio
1[*]	1.8	9	1.73
2	1.76	10	1.69
3	2.13	11	2.03
4	1.86	12	1.87
5	1.79	13	1.82
6	2.29	14	1.81
7	1.78	15[**]	1.68
8	2.18		

Table 4.12 Aspect Ratio of Cu-Zn-Al Samples Parallel To Rolling Direction Tested At 2×10^{-4} s $^{-1}$

No.	Aspect Ratio	No.	Aspect Ratio
1[*]	1.68	11	1.32
2	1.10	12	1.14
3	1.23	13	1.27
4	1.34	14	1.34
5	1.21	15	1.23
6	1.18	16	1.49
7	1.45	17	1.16
8	1.21	18	1.08
9	1.12	19	1.42
10	1.35	20[**]	1.10

[*]Closest to Fracture Tip
[**] Furthest from Fracture Tip

Table 4.13 Aspect Ratio of Cu-Zn-Al Samples Normal To Rolling Direction Tested At $2\times10^{-4}\,s^{-1}$

No.	Aspect Ratio	No.	Aspect Ratio
1[*]	1.45	19	1.19
2	1.43	20	1.23
3	1.32	21	1.32
4	1.12	22	1.21
5	1.30	23	1.36
6	1.27	24	1.41
7	1.23	25	1.23
8	1.40	26	1.38
9	1.21	27	1.18
10	1.12	28	1.29
11	1.33	29	1.13
12	1.32	30	1.31
13	1.21	31	1.29
14	1.19	32	1.20
15	1.12	33	1.21
16	1.01	34	1.16
17	1.31	35	1.19
18	1.21	36[**]	1.27

*Closest to Fracture Tip
** Furthest from Fracture Tip

96

Table 4.14 Aspect Ratio Of Cu-Zn-Al Samples Having 45 ° Angle With Rolling Direction Tested At $2\times10^{-4}\,s^{-1}$

No.	Aspect Ratio	No.	Aspect Ratio
1[*]	1.19	11	1.26
2	1.34	12	1.34
3	1.23	13	1.20
4	1.29	14	1.16
5	1.20	15	1.32
6	1.45	16	1.50
7	1.23	17	1.14
8	1.53	18	1.31
9	1.32	19	1.18
10	1.13	20[**]	1.09

*Closest to Fracture Tip
** Furthest from Fracture Tip

4.5.2 Al-Mg Alloy

4.5.2.1 Cavity Volume Fraction

Tables 4.15 to 4.18 show the cavity volume fraction of the tested Al-Mg samples. Data are tabulated along the gauge length and start from fracture surface to grip. Each value represents mean of cavity volume fraction measured from four different fields of view. The scatter of values about the mean is small, as can be noted from the raw data in tables A2.1 to A2.6. For each sample regardless of the rolling direction and strain rate the cavity volume fraction is higher near the fracture tip and gradually reduces near the grip portion.

The main difference between the results of two materials is that the Al-Mg materials are having less cavitation than Cu-Zn-Al materials. The absence of pre-existing pores is the major cause for this difference. Because pre-existing pore acts as cavity nucleation center and enhance the degree of cavitation.

Table 4.15 Cavity Volume Fraction of Al-Mg Tensile Sample Having Parallel Direction With Rolling Direction Tested at a Strain Rate of $2 \times 10^{-2} \, s^{-1}$

No.	Mean Cavity Volume Fraction	No.	Mean Cavity Volume Fraction
1[*]	27.39%	11	8.11%
2	26.37%	12	5.70%
3	25.45%	13	4.38%
4	19.41%	14	3.51%
5	20.08%	15	2.49%
6	13.55%	16	2.27%
7	114.39%	17	1.54%
8	10.05%	18	0.87%
9	7.90%	19	0.77%
10	8.11%	20[**]	0.66%

*Closest to Fracture Tip
** Furthest from Fracture Tip

Table 4.16 Cavity Volume Fraction of Al-Mg Tensile Sample Having Normal Direction With Rolling Direction Tested at a Strain Rate of $2\times10^{-2}\,s^{-1}$

No.	Mean Cavity Volume Fraction	No.	Mean Cavity Volume Fraction
1[*]	30.15%	11	17.65%
2	31.56%	12	15.79%
3	29.38%	13	11.38%
4	25.39%	14	8.36%
5	26.64%	15	5.09%
6	23.62%	16	3.75%
7	20.76%	17	2.16%
8	19.55%	18	1.87%
9	21.65%	19	1.51%
10	18.48%	20[**]	1.36%

*Closest to Fracture Tip
** Furthest from Fracture Tip

Table 4.17 Cavity Volume Fraction of Al-Mg Tensile Sample Having Parallel Direction With Rolling Direction Tested at a Strain rate of $2 \times 10^{-4} \, s^{-1}$

No.	Mean Cavity Volume Fraction	No.	Mean Cavity Volume Fraction
1[*]	26.20%	11	8.255
2	25.59%	12	6.29%
3	24.93%	13	4.35%
4	23.95%	14	2.93%
5	23.32%	15	2.45%
6	21.54%	16	1.35%
7	18.74%	17	1.21%
8	14.48%	18	0.93%
9	11.44%	19	0.8%
10	8.64%	20[**]	0.68%

*Closest to Fracture Tip
** Furthest from Fracture Tip

Table 4.18 Cavity Volume Fraction of Al-Mg Tensile Sample Having Normal Direction With Rolling Direction Tested at a Strain Rate of $2\times10^{-4}\,s^{-1}$

No.	Mean Cavity Volume Fraction	No.	Mean Cavity Volume Fraction
1[*]	28.29%	11	13.50%
2	29.30%	12	11.84%
3	27.65%	13	8.38%
4	26.71%	14	7.255
5	25.52%	15	6.155
6	23.20%	16	4.44%
7	21.52%	`17	3.55%
8	17.63%	18	3.01%
9	15.61%	19	1.74%
10	14.63%	20[**]	1.24%

*Closest to Fracture Tip
** Furthest from Fracture Tip

4.5.2.2 Aspect Ratio Analysis.

From the aspect ratio data it is found that aspect ratio is varying with strain rate. Regardless of the rolling direction the aspect ratio is closer to unity in case of lower strain rate than in higher strain rate. So it can be said that the cavities are more spherical in lower strain rate deformation than in higher strain rate. This observation for Al-Mg alloy is similar like Cu-Al-Zn alloy. Tables 4.17 to 4.20 show the distribution of aspect ratio along the gauge length. Figs. 4.21 shows the variation of aspect ratio with width strain. No significant variation has been observed.

Table 4.19 Aspect Ratio of Al-Mg Samples Normal To Rolling Direction Tested at a Strain Rate of $2\times10^{-2}s^{-1}$

No.	Aspect Ratio	No.	Aspect Ratio
1[*]	1.65	11	1.77
2	1.68	12	1.59
3	1.72	13	1.55
4	1.75	14	1.67
5	1.62	15	1.57
6	1.58	16	1.72
7	1.55	17	1.66
8	1.61	18	1.68
9	1.68	19	1.64
10	1.66	20[**]	1.71

*Closest to Fracture Tip
** Furthest from Fracture Tip

Table 4.20 Aspect Ratio of Al-Mg Samples Parallel To Rolling Direction Tested at a Strain Rate of $2\times10^{-2}s^{-1}$.

No.	Aspect Ratio	No.	Aspect Ratio
1[*]	1.78	11	1.70
2	1.75	12	1.68
3	1.81	13	1.75
4	1.77	14	1.77
5	1.69	15	1.68
6	1.57	16	1.59
7	1.62	17	1.63
8	1.65	18	1.69
9	1.68	19	1.73
10	1.72	20[**]	1.78

Table 4.21 Aspect Ratio of Al-Mg Samples Normal To Rolling Direction Tested at a Strain Rate of $2\times10^{-4}s^{-1}$.

No.	Aspect Ratio	No.	Aspect Ratio
1[*]	1.26	11	1.32
2	1.28	12	1.31
3	1.31	13	1.25
4	1.39	14	1.30
5	1.34	15	1.25
6	1.25	16	1.28
7	1.26	17	1.40
8	1.29	18	1.29
9	1.36	19	1.33
10	1.26	20[**]	1.28

*Closest to Fracture Tip
** Furthest from Fracture Tip

Table 4.22 Aspect Ratio of Al-Mg Samples Parallel To Rolling Direction Tested at a Strain Rate of $2\times10^{-4}s^{-1}$.

No.	Aspect Ratio	No.	Aspect Ratio
1[*]	1.31	11	1.42
2	1.38	12	1.41
3	1.41	13	1.45
4	1.44	14	1.40
5	1.45	15	1.38
6	1.36	16	1.33
7	1.31	17	1.32
8	1.34	18	1.41
9	1.37	19	1.45
10	1.46	20[**]	1.38

* Closest to Fracture Tip
** Furthest from Fracture Tip
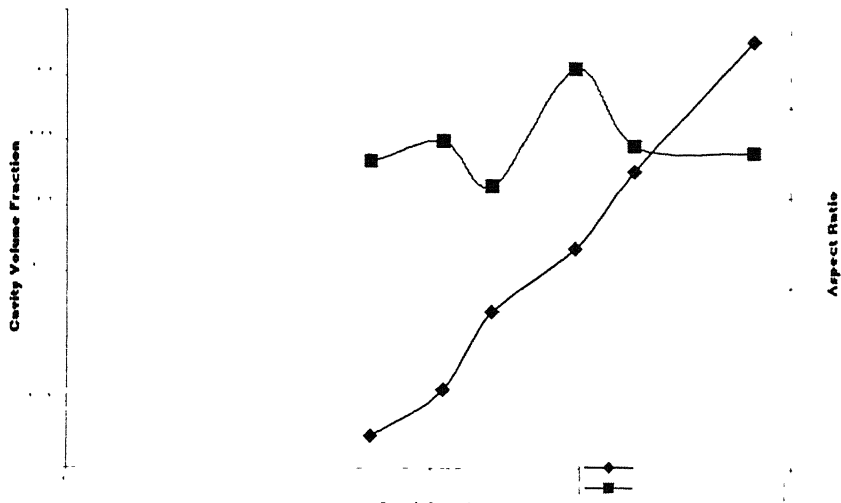
Fig. 4.24a The variation of cavity volume fraction and aspect ratio with width strain for the Cu-Zn-Al tensile samples, having a orientation normal to the rolling direction, tested at a strain rate of $2x10^{-2}s^{-1}$
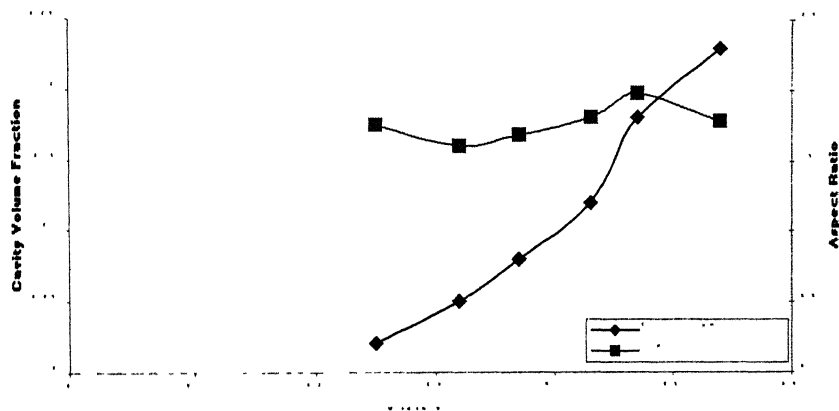
Fig. 4.24b The variation of cavity volume fraction and aspect ratio of the Cu-Zn-Al tensile samples, having a orientation parallel to the rolling axis, tested at a strain rate of $2x10^{-2}s^{-1}$
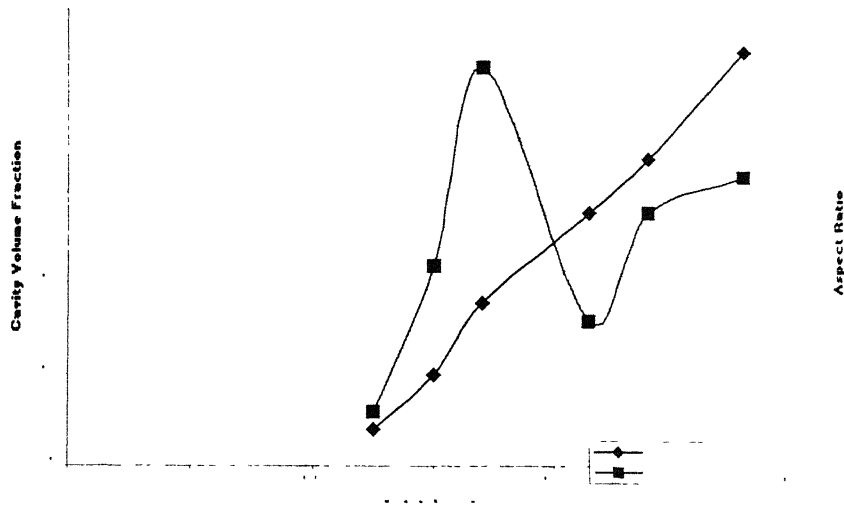
Fig. 4.24c The variations of cavity volume fraction and aspect ratio with width strain for the Cu-Zn-Al tensile samples, having a orientation of 45 degree to the rolling axis, tested at a strain rate of $2 \times 10^{-2} s^{-1}$
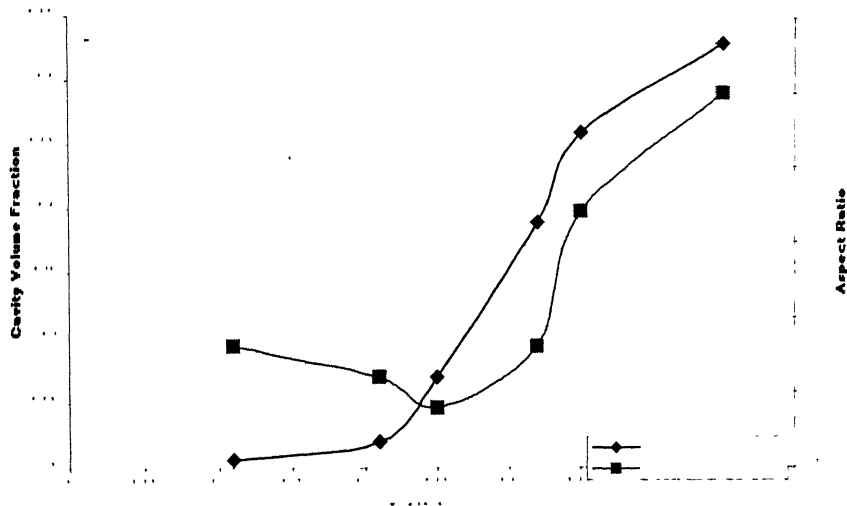
Fig. 4.24d The variations of cavity volume fraction and aspect ratio with width strain for the Cu-Zn-Al samples, having a orientation normalto the rolling direction, tested at a strain rate of $2 \times 10^{-4} s^{-1}$

107
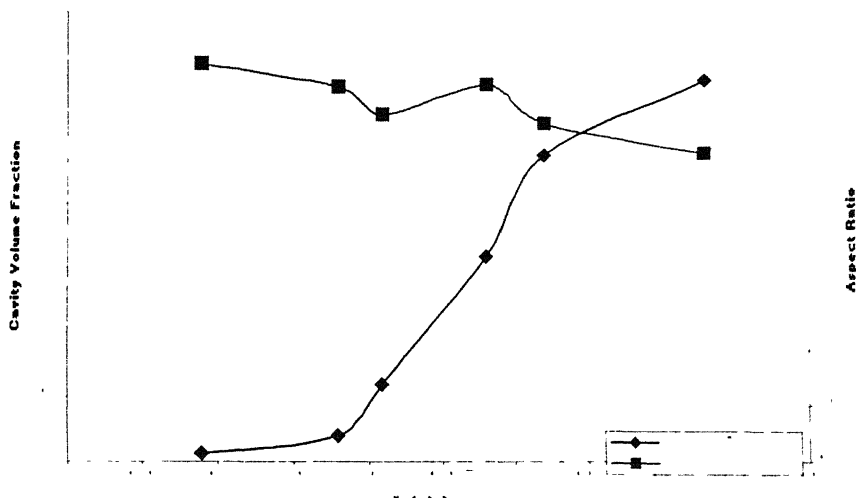
Fig. 4.24e The variations of cavity volume fraction and aspect ratio with width strain for the Cu-Zn-Al tensile samples, having a orientation parallel to the rolling axis, tested at a strain rate of $2 \times 10^{-4} s^{-1}$
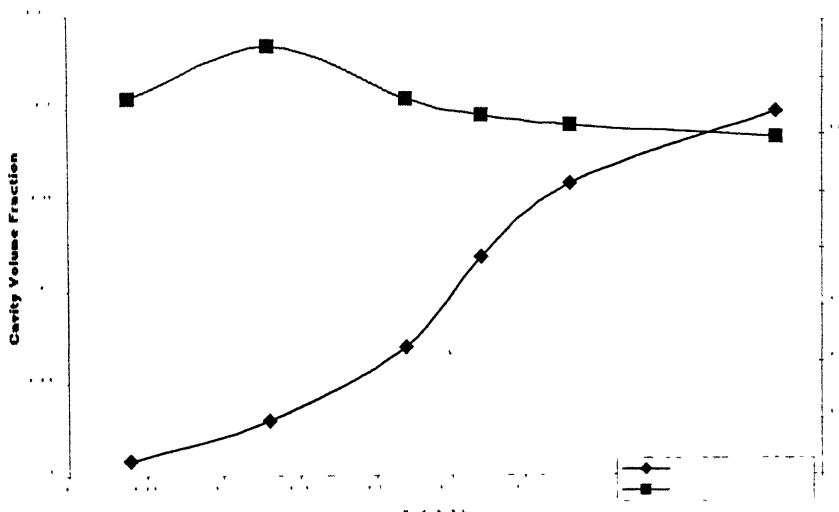
Fig. 4.24f The variations of cavity volume fraction and aspect ratio with width strain for the Cu-Zn-Al tensile samples, having a orientation of 45 degrees to the rolling direction, tested at a strain rate of $2 \times 10^{-4} s^{-1}$

108
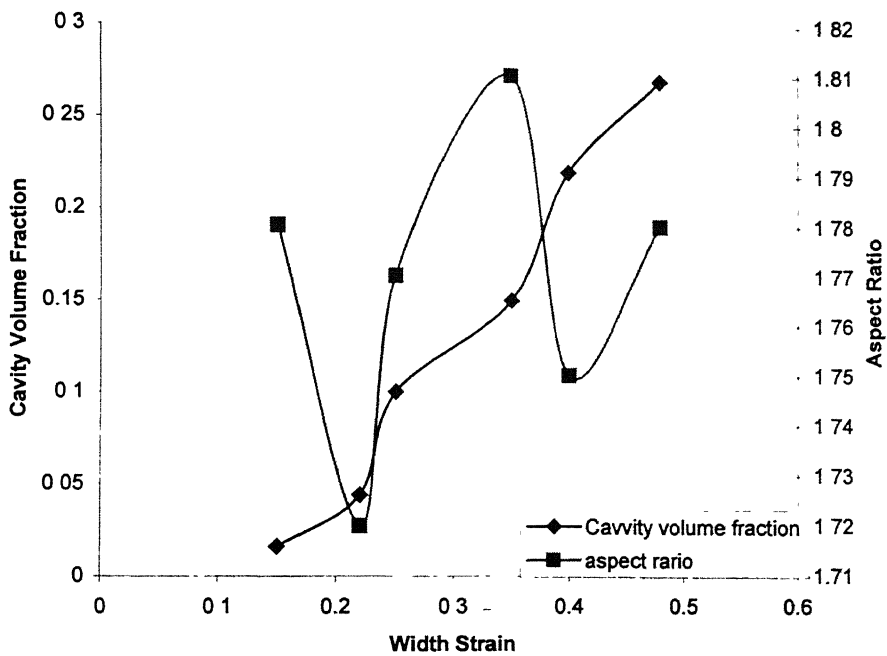
Fig. 4.25a The variations of cavity volume fraction and aspect ratio with width strain for the Al-Mg tensile samples, having a orientation parallel to the rolling direction, tested at a strain rate of 2x10⁻²s⁻¹.
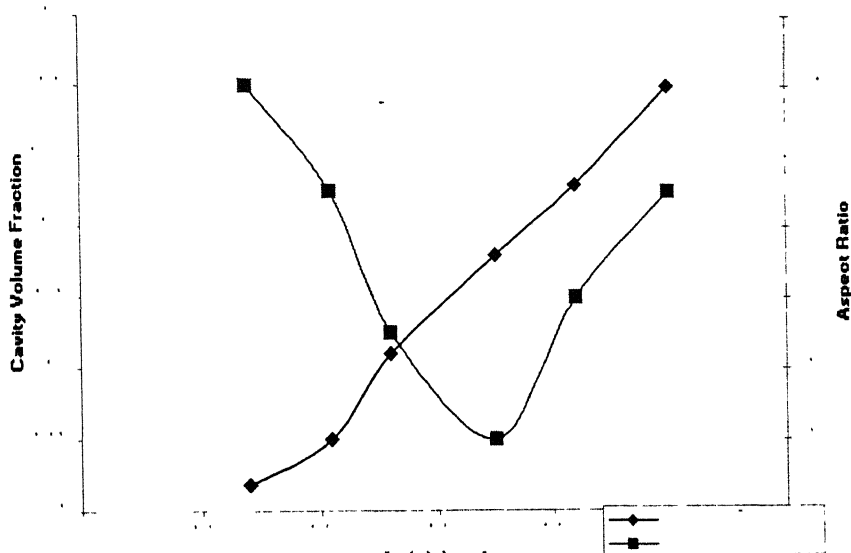
Fig. 4.25b The variations of cavity volume fraction and aspect ratio with width strain for the Al-Mg tensile samples, having a orientation normal to the rolling direction, tested at a strain rate of 2x10⁻²s⁻¹
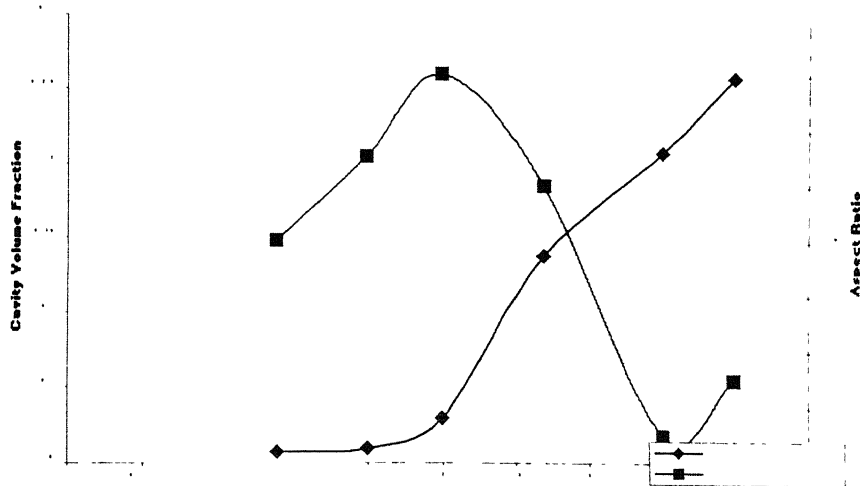
Fig. 4.25c The variation of cavity volume fraction and aspect ratio with width strain for the Al-Mg tensile samples, having a orientation parallel to the rolling axis, tested at a strain rate of $2x10^{-4}s^{-1}$.
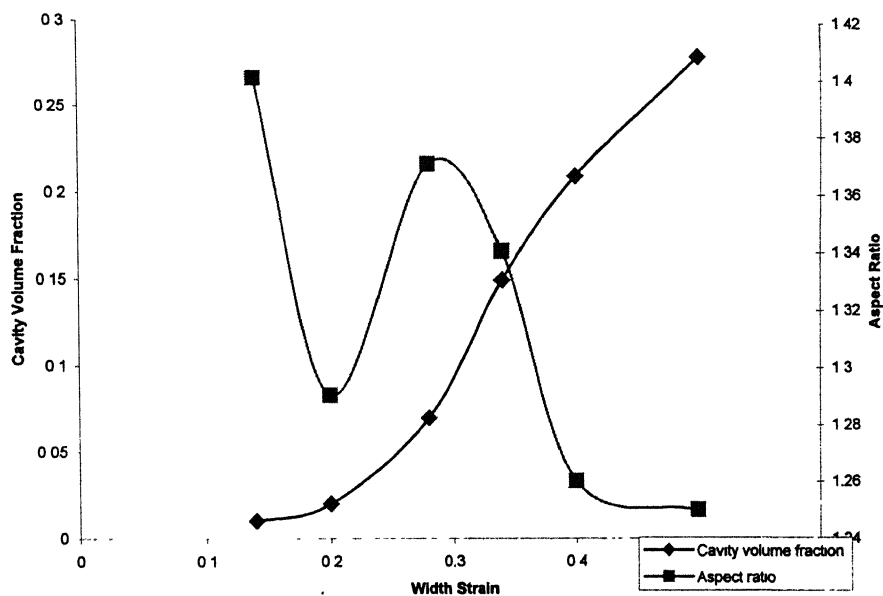
Fig. 4.25d The variation of cavity volume fraction and aspect ratio with width strain for the Al-Mg tensile samples, having a orientation normal to the rolling direction, tested at a strain rate of $2x10^{-4}s^{-1}$

5. Conclusions

1. In case of Cu-Zn-Al alloy the degree of cavitation is higher at the strain rate of $2\times10^{-2}s^{-1}$ than that at the strain rate of $2\times10^{-2}s^{-1}$. In case of Al-Mg alloy the reverse has been observed.

2. For all cases the cavity volume fraction has the highest value near the fracture tip and has the lowest value near the grip region.

3. At lower strain rate diffusion controlled cavity growth mechanism is dominant whereas at higher strain rate strain induced cavity growth mechanism tends to dominate.

4. For the samples, tested normal to the rolling direction, cavities are aligned along the direction normal to the tensile axis. For parallel sample cavities are aligned along the tensile axis. In both cases cavities are along the rolling direction.

5. In case of Cu-Zn-Al alloy the degree of cavitation has it's least value in the samples having 45° orientation with rolling direction.

6. Strain rate has significant effect on the morphology and fracture behavior.

7. The mode of fracture in superplastic deformation is ductile.

8. Extensive interlinkage of cavities has taken place, which leads to decrease in load bearing cross-section and ultimately results in fracture.

9. At lower strain rate the extent of interconnectivity of cavities is less

10. Grain relief is taking place in superplastic deformation.

111

References

1. Davies, G.J; Edington, J.W.; Cutler, C.P.; Padmanavan, K.A.: J. Mater. Sci 5 (1970) 1091

2. Rosenhain, W.; Haughton, J.L.; Bingham, K.E.: J. Inst. Met. 23 (1920) 261

3. Davies, G.J.; Padmanavan, K.A.; *Superplasticity* (1980) pp1

4. Hargreaves, F. J. Inst. Met. 39 (1928) 301-327

5. Hargreaves, F.; Hills, R.J.: J. Inst. Met 41 (1929) 257-283

6. Jenkins, C.M.H. J. Inst. Met. 40 (1928) 41-54

7. Pearson, C.E. J.Inst. Met. 54 (1934) 111-124

8. Underwood, E.E. J. Metals 14 (1962) 914-919

9. Thomsen, T.H.; Holt D.L.; Met. Eng. Quart. 2 (1970) 1-12

10. Wakai, F; Sakaguchi, S; Adv. Ceram. Mater 1 (1986) 259-263

11. Nieh, T.G.; Sherby, O.D: Superplasticity in Metals and Ceramic (1997) 14

12. Nieh, T.G.; Hanshall, C.A. 18 Scr. Metall. (1984) 1405-1408

13. Bacofen, W.A; Turner, I.R.: Trans. Am. Soc. Met. 57(1964) 980

14. Davies, G.J.; Padmanavan, K.A.; *Superplasticity* (1980) pp 32

15. Langdon, T.G. *Superplastic Forming of Structural Alloys,* Ed. Paton, N.E; Hamilton, C.H. (1982) 27-40

16. Mukherjee, A.K. Material Sci. and Eng. 8 (1971) 83-89

17. Ashby, M.F.; Verall, R.A.:Acta. Metall.21 (1973) 149-163

18. Spingarn, J.R.; Nix, W.D.: Acta Metall 26 (1978) 1389-1398

19. Gifkins. R.C : *Superplastic Forming of Structural Alloys,* Ed. Paton, N.E; Hamilton, C.H. (1982) 3-26

20. Hutchinsion, M.M; Ball, A: Metal Sci. J. 3 (1969) 1-7

21. Davies, G.J.; Padmanavan, K.A.; *Superplasticity* (1980) pp96

22. Stowell, M.J *Superplastic Forming of Structural Alloys,* Ed. Paton, N.E; Hamilton, C.H. (1982) 321-336

23. Bampton, C.C.; Raj, R Acta. Metall. 30 (1982) 2043-2053

24. Livesay, D.W.; Ridley,N. Metall. Trans. 9A (1978) 519-526

25. Chandra T., Jonas, J.J. J.Mat. Sci. 13 (1978) 2380-2384

26. Asfby, M.F.; Cocks, A.C.F Mat. Sci. 16 (1982) 465-474

27. Asfby, M.F.; Cocks, A.C.F Mat. Sci. 14 (1980) 395-402

28. Hancock, J.W. Metal. Sci. 10 (1976) 319-325

29. Rice, J.R; Tracy, D.M J.Mech. Phys. Solids 17 (1969) 201-217

30. Ridley, N.; Stowell, M.J Acta. Metall. 32 (1984) 35-42

31. Pilling, J.; Ridley, N Acta. Metall. 34 (1986) 669-679

Appendix

Cavity Volume fraction data

Cu-Zn-Al Samples.

Table A.1 Cavity volume fraction of samples, having tensile axis at an angle of 45^0 to rolling direction, tested at a strain rate of 2×10^{-2} s^{-1}

No.	Cavity Volume Fraction	Mean	No.	Cavity Volume Fraction	Mean
1*	10.71% 10.32% 10.70% 11.45%	10.79%	8	4.33% 4.56% 4.19% 4.89%.	4.49
2	7.29% 7.05% 8.14% 7.35%	7.45	9	1.62% 1.23% 1.57% 1.72%	1.52
3	7.96% 7.34% 7.86% 7.12%	7.57%	10	1.18% 1.23% 1.39% 1.12%	1.23
4	7.33% 7.56% 7.23% 7.98%	7.52%	11	1.05% 1.11% 0.99% 1.13%	1.07
5	6.29% 6.45% 6.76% 5.98%	6.37%	12	0.89% 0.78% 0.86% 0.96%	0.87%
6	5.27% 5.67% 5.24% 5.37%	5.38%	13	0.50% 0.45% 0.61% 0.43%	0.49%

No.	Cavity volume fraction	Mean	No	Cavity volume fraction	Mean
7	4.79% 4.67% 4.35% 4.97%	4.69%	14*	0.82% 0.78% 0.92% 0.89%	0.85%

Table A1.2 Cavity Volume Fraction OfSamples Normal To Rolling Direction, Tested At a Strain Rate of $2\times10^{-2}\,s^{-1}$.

No.	Cavity volume fraction	Mean	No	Cavity volume fraction	Mean
1*	33.61% 33.23% 33.14% 33.70%	33.42%	19	11.92% 11.34% 11.85% 12.14%	11.81%
2	40.10% 40.32% 33.96% 40.19%	38.64%	20	9.23% 8.93% 9.05% 9.38%	9.14%
3	25.35% 25.25% 25.67% 25.03%	25.32%	21	9.50% 9.34% 9.72% 9.61%	9.54%
4	21.09% 21.45% 20.76% 21.39%	21.17%	22.	7.45% 7.23% 7.78% 7.16%	7.40%
5	23.00% 23.59% 22.67% 23.05%	23.07	23	7.06% 7.45% 6.85% 6.95%	7.07%
6	25.59% 25.67% 24.87% 25.34%	25.36%	24	6.27% 6.34% 6.21% 6.56%	6.34%
7	20.21% 20.56% 20.34% 20.45%	20.39%	25	6.98% 7.09% 7.13% 6.62%	6.95%
8	18.76% 18.45%		26	5.01% 4.78%	

	19.48% 18.61%	18.82%		4.82% 5.25%	4.96%
9	17.67% 17.56% 17.47% 18.05%	17.68%	27	4.46% 4.23% 4.69% 4.35%	4.43%
10	17.14% 17.43% 17.23% 17.02%	17.20%	28	4.14% 4.57% 3.97% 4.24%	4.23%
11	17.32% 17.23% 17.45% 16.91%	17.22%	29	3.97% 3.59% 3.81% 4.17%	3.88%
12	14.85% 14.67% 15.32% 14.78%	14.90%	30	3.72% 3.89% 3.26% 3.93%	3.70%
13	14.93% 14.57% 14.79% 15.23%	14.88%	31	4.43% 4.56% 4.79% 4.09%	4.46%
14	14.23% 14.35% 13.87% 14.21%	14.16%	32	4.69% 4.23% 4.97% 4.50%	4.59%
15	14.00% 14.56% 13.95% 14.18%	14.17%	33	4.43% 4.98% 4.40% 4.34%	4.53%
16	12.00% 11.94% 11.79% 12.80%	12.13%	34	2.36% 2.56% 2.18% 2.67%	2.44%
17	11.99% 11.56% 11.45% 12.21%	11.80%	35	2.50% 2.14% 2.69% 2.45%	2.44%
18	10.27% 10.47% 10.34% 10.21%	10.32%	36[**]	2.36% 2.37% 2.11% 2.64%	2.37%

III

Table A1.3 Cavity Volume Fraction Of Samples Parallel To Rolling Direction Tested At a Strain Rate of $2\times10^{-2}\,\mathrm{s}^{-1}$

No.	Cavity volume fraction	Mean	No.	Cavity volume fraction	Mean
1*	23.36% 23.34% 23.57% 23.26%	23.38%	13 - 	8.95% 9.42% 8.86% 9.04%	9.06%
2	22.50% 22.56% 22.13% 22.19%	22.32%	14	9.68% 9.06% 10.21% 9.83%	9.69%
3	22.96% 22.67% 22.52% 23.00%	22.78%	15	8.18% 8.10% 8.45% 8.34%	8.26%
4	20.82% 21.23% 21.31% 21.05%	21.10%	16	8.41% 8.34% 8.62% 8.12%	8.37%
5	20.65% 20.23% 21.17% 20.75%	20.70%	17	8.52% 8.43% 8.33% 8.73%	8.50%
6	26.30% 26.70% 26.43% 25.98%	26.35%	18	6.14% 6.05% 5.99% 5.86%	6.01%
7	18.79% 18.49% 18.45% 18.80%	18.63%	19	6.75% 6.95% 6.34% 7.07%	6.77%
8	18.37% 18.47% 18.92% 18.42%	18.54%	20	5.23% 5.45% 5.34% 5.71%	5.43%

No.	Cavity volume fraction	Mean	No.	Cavity volume Fraction	Mean
9	16.48% 16.78% 16.91% 16.42%	16.64%	21	2.72% 2.56% 2.78% 2.17%	2.55%
10	12.71% 12.53% 12.84% 12.41%	12.62%	22	1.33% 1.34% 1.54% 1.27%	1.37%
11	10.00% 10.67% 10.56% 9.67%	10.22%	23[**]	1.78% 1.70% 1.45% 1.73%	1.66%

Table A1.4 Cavity Volume Fraction Of Samples Parallel To Rolling Direction Tested At $2\times10^{-4}\,s^{-1}$

No.	Cavity volume fraction	Mean	No.	Cavity volume Fraction	Mean
1[*]	30.02% 29.67% 30.13% 30.23%	30.01%	19	11.45% 11.19% 11.52% 11.33%	11.37%
2	31.24% 31.33% 31.45% 31.10%	31.28%	20	9.08% 8.74% 9.20% 9.12%	9.03%
3	24.67% 24.51% 24.78% 24.32%	24.57%	21	8.40% 8.45% 8.30% 8.79%	8.48%
4	22.56% 22.29% 22.72% 22.28%	22.46%	22	6.78% 6.74% 6.92% 6.38%	6.68%
5	23.89% 23.49% 24.01% 23.75%	23.78%	23	7.15% 7.33% 7.45% 7.27%	7.30%

6	16.78% 16.46% 16.58% 16.93%	16.68%	24	7.03% 6.94% 6.77% 7.14%	6.97%
7	20.08% 20.29% 19.89% 19.94%	20.05%	25	5.98% 6.03% 5.84% 6.10%	5.98%
8	19.56% 19.45% 19.50% 19.81%	19.58%	26	4.91% 5.08% 4.87% 5.16%	5.00%
9	20.68% 21.00% 21.07% 20.93%	20.92%	27	3.78% 3.77% 3.50% 3.82%	3.71%
10	16.57% 16.68% 16.45% 16.33%	16.50%	28	4.57% 4.56% 4.20% 4.18%	4.37%
11	13.90% 14.21% 13.63% 13.88%	13.90%	29	2.92% 2.47% 2.97% 3.06%	2.85%
12	12.97% 13.34% 13.20% 13.06%	13.14%	30	2.01% 1.99% 2.18% 2.07%	2.06%
13	12.56% 12.45% 12.30% 12.78%	12.52%	31	1.90% 1.97% 1.85% 2.02%	1.93%
14	15.89% 15.56% 15.30% 15.34%	15.52%	32	1.35% 1.45% 1.29% 1.50%	1.39%
15	14.98% 14.55% 15.11% 15.37%	15.00%	33	1.01% 0.98% 1.07% 1.11%	1.04%
16	13.56% 13.45% 13.47% 13.62%	13.52%	34	0.98% 1.02% 0.94% 1.00%	0.98%
17	12.98% 13.92%		35	0.51% 0.42%	

No.	Cavity volume fraction	Mean	No.	Cavity volume fraction	Mean
	13.00% 12.73%	13.15%		0.75% 0.62%	.0.57%
18	13.45% 13.56% 13.42% 13.33%	13.44	36[**]	0.23% 0.18% 0.31% 0.22%	0.23%

Table A1.5 Cavity Volume Fraction Of Samples Normal To Rolling Direction Tested At $2 \times 10^{-4}\,s^{-1}$

No.	Cavity volume fraction	Mean	No.	Cavity volume fraction	Mean
1[*]	33.00% 33.24% 33.39% 32.97%	33.15%	19	12.79% 12.45% 12.38% 12.84%	12.61%
2	32.01% 31.89% 32.34% 32.11%	32.08%	20	8.11% 8.43% 8.05% 8.23%	8.20%
3	43.09% 43.06% 43.22% 42.81%	43.05%	21	9.05% 9.23% 9.01% 8.94%	9.05%
4	26.89% 27.12% 26.74% 27.05%	26.95%	22	6.78% 6.71% 6.48% 6.92%	6.72%
5	30.06% 30.18% 29.97% 29.89%	30.02%	23	5.67% 5.51% 5.79% 5.55%	5.63%
6	22.46% 22.23% 22.59% 22.27%	22.38%	24	7.30% 7.78% 7.55% 7.27%	7.47%
7	22.60% 22.45% 22.51% 22.33%	22.47%	25	4.89% 4.55% 4.44% 4.62%	4.62%

8	19.43% 19.34% 19.49% 19.31%	19.39%	26	3.34% 3.61% 3.29% 3.73%	3.49%
9	17.10% 17.39% 17.82% 17.22%	17.38%	27	3.22% 3.52% 3.16% 3.40%	3.32%
10	21.39% 21.19% 21.08% 21.42%	21.27%	28	2.13% 2.07% 2.22% 2.17%	2.14%
11	15.13% 15.34% 15.20% 15.08%	15.18%	29	2.19% 2.11% 2.06% 2.22%	2.14%
12	15.97% 16.09% 16.41% 15.77%	16.06%	30	1.29% 1.17% 1.33% 1.42%	1.30%
13	16.10% 15.89% 15.73% 16.00%	15.93%	31	2.01% 2.15% 2.04% 2.28%	2.12%
14	16.15% 16.49% 16.28% 16.41%	16.33%	32	1.53% 1.45% 1.33% 1.28%	1.39%
15	13.59% 13.74% 13.38% 13.29%	13.50%	33	0.98% 0.84% 0.92% 0.84%	0.89%
16	17.39% 17.56% 17.44% 17.26%	17.41%	34	0.84% 0.79% 0.82% 0.78%	0.80%
17	17.22% 17.52% 17.41% 17.49%	17.41%	35	0.53% 0.56% 0.65% 0.68%	0.60%
18	13.15% 13.67% 13.42% 13.66%	13.47%	36**	0.33% 0.29% 0.26% 0.37%	0.31%

VIII

Table A1.6 Cavity Volume Fraction Of Samples Having 45° Angel With Rolling Direction Tested At 2×10^{-4} s^{-1}

No.	Cavity volume fraction	Mean	No.	Cavity volume fraction	Mean
1*	18.79% 18.71% 18.65% 18.49%	18.66%	19	7.32% 7.46% 7.31% 7.21%	7.32%
2.	20.73% 20.63% 21.01% 20.59%	20.74%	20	6.76% 6.72% 6.71% 6.98%	6.79%
3.	16.24% 16.39% 16.73% 16.29%	16.41%	21	4.19% 4.29% 4.17% 4.31%	4.24%
4	16.17% 16.06% 15.93% 16.22%	16.09%	22	5.70% 5.49% 5.27% 5.28%	5.43%
5	12.79% 12.71% 12.59% 12.99%	12.77%	23	3.27% 3.45% 3.29% 3.61%	3.40%
6	10.83% 10.59% 10.92% 10.77%	10.77%	24	2.83% 2.66% 2.47% 2.94%	2.72%
7	11.73% 11.39% 11.88% 11.53%	11.63%	25	2.24% 2.28% 2.48% 2.33%	2.33%
8	10.98% 10.59% 10.63% 11.18%	10.84%	26	2.89% 3.04% 2.82% 2.69%	2.86%
9	8.31% 8.21% 8.19% 8.13%	8.21%	27	3.17% 3.08% 3.33% 3.25%	3.20%

10	7.60%		28	2.07%	
	7.95%			2.17%	
	7.36%	7.58%		1.96%	2.08%
	7.44%			2.12%	
11	7.50%		29	1.56%	
	7.43%			1.63%	
	7.81%	7.49%		1.79%	1.63%
	7.25%			1.54%	
12	8.60%		30	1.47%	
	8.39%			1.49%	
	8.17%	8.45%		1.39%	1.41%
	8.66%			1.32%	
13	7.15%		31	1.21%	
	7.33%			1.20%	
	7.19%	7.15%		1.37%	1.31%
	6.96%			1.47%	
14	7.60%		32	1.06%	
	7.77%			1.23%	
	7.49%	7.59%		1.14%	1.11%
	7.53%			1.01%	
15	6.20%		33	00.85%	
	6.48%			00.79%	
	6.35%	6.29%		00.89%	00.86%
	6.14%			00.94%	
16	6.99%		34	00.65%	
	7.09%			00.58%	
	6.79%	6.94%		00.63%	00.64%
	6.90%			00.70%	
17	6.50%		35	00.99%	
	6.54%			1.02%	
	6.95%	6.58%		00.97%	1.00%
	6.36%			1.05%	
18	7.32%		36**	00.33%	
	7.09%			00.41%	
	7.44%	7.33%		00.45%	00.37%
	7.48%			00.29%	

Al-Mg Samples

Table A2.1 Cavity Volume Fraction of Al-Mg Tensile Sample Having Parallel Direction With Rolling Direction Tested at a Strain Rate of $2\times10^{-2}\,s^{-1}$

X

No.	Cavity Volume Fraction	Mean	No.	Cavity Volume Fraction	Mean
1[*]	27.48% 27.85% 27.18% 27. 08%	27.39%	11	8.01% 7.93% 8.09% 8.41%	8.11%
2	26.71% 25.95% 26.43% 26.39%	26.37%	12	5.69% 5.89% 5.32% 5.91%	5.70%
3	25.49% 25.24% 25.71% 25.38%	25.45%	13	4.20% 4.18% 4.43% 4.71%	4.38%
4	21.09% 21.89% 21.37% 21.23%	21.39%	14	3.51% 3.32% 3.51% 3.71%	3.51%
5	19.56% 19.29% 19.34% 19.47%	19.41%	15	2.41% 2.71% 2.49% 2.37%	2.49%
6	20.07% 20.39% 19.81% 20.07%	20.08%	16	2.01% 2.18% 2.48% 2.41%	2.27%
7	17.51% 17.39% 17.45% 17.86%	13.55%	17	1.67% 1.53% 1.61% 1.37%	1.54%
8	14.32% 14.19% 14.39% 14.67%	14.39%	18	1.52% 1.52% 1.71% 1.38%	1.53%
9	10.05% 9.69% 10.11% 10.37%	10.05%	19	0.93% 1.03% 0.83% 0.71%	0.87%
10	7.89% 7.94% 8.01% 7.77%	7.90%	20[**]	0.89 % 0.83% 0.71% 0.68%	0.77%

Table A2.2 Cavity Volume Fraction of Al-Mg Tensile Sample Having Normal Direction With Rolling Direction Tested at a Strain Rate of $2\times10^{-2}\,s^{-1}$

No.	Cavity Volume Fraction	Mean	No.	Cavity Volume Fraction	Mean
1[*]	30.01% 30.15% 30.31% 30.15%	30.15%	11	17.82% 17.54% 17.58% 17.68%	17.65%
2	31.59% 31.78% 31.42% 31.47%	31.56%	12	15.67% 15.67% 15.97% 15.85%	15.79%
3	29.47% 29.53% 29.13% 29.41%	29.38%	13	11.34% 11.36% 11.41% 11.42%	11.38%
4	25.59% 25.45% 25.67% 25.08%	25.39%	14	8.31% 8.34% 8.20% 8.59%	8.36%
5	26.49% 26.48% 26.89% 26.72%	26.64%	15	5.04% 4.93% 5.11% 5.31%	5.09%
6	23.45% 23.49% 23.67% 23.89%	23.62%	16	3.72% 3.97% 3.62% 3.71%	3.75%
7	20.94% 20.78% 20.56% 20.79%	20.76%	17	2.19% 2.16% 2.08% 2.22%	2.16%
8	19.84% 19.51% 19.49% 19.39%	19.55%	18	1.97% 1.94% 1.74% 1.83%	1.87%
9	21.97% 21.84% 21.47% 21.34%	21.65%	19	1.63% 1.34% 1.48% 1.59%	1.51%
10	18.51% 18.39% 18.37%	18.48%	20[**]	1.32% 1.49% 1.28%	1.36%

	18.67%			1.36%	

Table A2.3 Cavity Volume Fraction of Al-Mg Tensile Sample Having Parallel Direction With Rolling Direction Tested at a Strain rate of $2\times10^{-4}\,s^{-1}$

No.	Cavity Volume Fraction	Mean	No.	Cavity Volume Fraction	Mean
1[*]	26.15% 26.46% 26.04% 26.17%	26.20%	11	8.25% 8.17% 8.38% 8.22%	8.25%
2	25.59% 25.94% 25.24% 25.61%	25.59%	12	6.34% 6.18% 6.29% 6.38%	6.29%
3	25.12% 25.07% 24.96% 24.59%	24.93%	13	4.31% 4.37% 4.29% 4.44%	4.35%
4	24.39% 24.92% 23.98% 23.15%	23.95%	14	3.01% 2.81% 2.84% 3.08%	2.93%
5	23.22% 23.56% 23.18% 23.34%	23.32%	15	2.37% 2.38% 2.49% 2.57%	2.45%
6	21.67% 21.35% 21.72% 21.45%	21.54%	16	1.39% 1.47% 1.26% 1.29%	1.35%
7	18.79% 18.56% 18.72% 18.92%	18.74%	17	1.12% 1.16% 1.31% 1.25%	1.21%
8	14.56% 14.39% 14.71%	14.48%	18	0.98% 0.83% 1.05%	0.93%

	14.28%			0.86%	
9	11.38%		19	0.83%	
	11.34%			0.89%	
	11.49%	11.44%	.	0.73%	0.8%
	11.57%			0.75%	
10	8.93%		20[**]	0.78%	
	8.39%			0.65%	
	8.71%	8.64%		0.59%	0.68%
	8.54%			0.71%	

Table A2.4 Cavity Volume Fraction of Al-Mg Tensile Sample Having Normal Direction With Rolling Direction Tested at a Strain Rate of $2\times10^{-4}\,s^{-1}$

No.	Cavity Volume Fraction	Mean	No.	Cavity Volume Fraction	Mean
1[*]	28.37%		11	13.48%	
	28.56%			13.65%	
	28.17%	28.29%		13.71%	13.50%
	28.07%			13.18%	
2	29.05%		12	11.94%	
	29.61%			11.88%	
	29.39%	29.30%		11.63%	11.84%
	29.17%			11.93%	
3	27.84%		13	8.41%	
	27.72%			8.58%	
	27.59%	27.65%		8.37%	8.38%
	27.46%			8.18%	
4	26.78%		14	7.31%	
	26.58%			7.35%	
	26.85%	26.71%		7.25%	7.25%
	26.64%			7.09%	
5	25.38%		15	6.04%	
	25.61%			6.14%	
	25.26%	25.52%		6.20%	6.15%
	25.83%			6.25%	
6	23.05%		16	4.35%	

	23.17%			4.33%	
	23.39%	23.20%		4.47%	4.44%
	23.19%			4.61%	
7	21.56%		17	3.17%	
	21.46%			3.78%	
	21.62%	21.52%		3.59%	3.55%
	21.44%			3.67%	
8	17.67%		18	2.98%	
	17.55%			2.90%	
	17.89%	17.63%		3.11%	3.01%
	17.42%			3.05%	
9	15.82%		19	1.78%	
	15.75%			1.57%	
	15.48%	15.61%		1.79%	1.74%
	15.39%			1.85%	
10	14.50%		20**	1.25%	
	14.67%			1.15%	
	14.55%	14.63%		1.31%	1.24%
	14.81%			1.27%	

* Closest to Fracture Tip
** Furthest from Fracture Tip

XV